Dynamical downscaling of prevailing synoptic-scale winds over the complex terrain of Mariepskop, South Africa

by

Ilze PRETORIUS

Submitted in partial fulfillment of the requirements

for the degree

MASTER OF SCIENCE

in the

Faculty of Natural and Agricultural Sciences

University of Pretoria

May 2013

Dynamical downscaling of prevailing synoptic-scale winds over the complex terrain of Mariepskop, South Africa

Ilze PRETORIUS

Promoter	Prof. C.J.DeW. Rautenbach
Department	Department of Geography, Geoinformatics and Meteorology
Faculty	Faculty of Natural and Agricultural Sciences
University	University of Pretoria
Degree	Master of Science in Meteorology

Summary

Mariepskop (direct translation: “Marieps hill”) forms part of the northernmost edge of the Drakensberg Mountain range in the east of South Africa, and is known for its complex topography associated with meso-scale atmospheric circulation, and therefore its numerous climatic zones. As a result the mountain hosts a high degree of biodiversity. The peak of Mariepskop lies at approximately 1900m Above Mean Sea Level (AMSL), which is higher than the surrounding escarpment to the east bordering the Highveld. Its foothills also extend well into the Lowveld at about 700m AMSL. Mariepskop is therefore ideal for studying airflow exchange between the industrialized Highveld and the Lowveld with its diversity of natural resources. It is also ideal for detecting global warming signals on altitudinal gradients extending from the Lowveld to altitudes above the Highveld escarpment. In this study, long-term National Centre for Atmospheric Research / National Centre for Environmental Prediction (NCAR/NCEP) reanalysis wind data at two atmospheric pressure levels (850hPa and 700hPa), as well as reanalysis near-surface temperature data, were obtained for the Mariepskop region for the austral summer (and winter) seasons. The data was used to force a Computational Fluid Dynamics (CFD) model (also known as STAR-CCM+) across its lateral boundaries with the dominant synoptic flow in order to generate mesoscale simulation output over the complex terrain of Mariepskop. Wind speed and direction modelled results were then correlated to observations measured by three weather stations on Mariepskop. Modelled wind flow results for the summer simulation were also validated against aerial photographs in order to infer whether the model could accurately capture areas with high rainfall, which are related to denser vegetation.

DECLARATION

I declare that this dissertation that I am submitting for a MSC (Meteorology) degree in the Department of Geography, Geoinformatics and Meteorology at the University of Pretoria has not previously been submitted by me for degree purposes at any other university. I also declare that the research content of this dissertation is a representation of my own work.

Signature: _____ Date: _____

ACKNOWLEDGEMENTS

The author wishes to express her appreciation to the following persons and institutions who have contributed immensely towards the success of her research work:

1. First and foremost I would like to thank my parents for giving me the opportunity to study and for their love and support during my studies;
2. To my promoter, Prof. C.J.DeW. Rautenbach, for his help and patience;
3. To the employees at Aerotherm, especially Christiaan de Wet and Ignus le Roux for their support with the STAR-CCM+ package;
4. To Martin van Staden, the director of Aerotherm, for the use of STAR-CCM+ academic licenses and their super computers;
5. To my husband, Johan, for his love and support.

TABLE OF CONTENTS

LIST OF SYMBOLS

μ_{eff}	Effective viscosity
μ_l	Laminar viscosity
μ_t	Turbulent viscosity
a	Face area vector
A	Invicid flux jacobian
C_μ	Critical coefficient
E	Total energy
f	Body force vector
Fr	Froude number
f_r, f_g, f_p, f_u	Body force terms
g	Gravitational acceleration
G_b	Buoyancy production term
H	Total enthalpy
I	Identity matrix
k	Turbulent kinetic energy
L	Temperature lapse rate
M	Molecular mass of air
p	Wind speed exponent
$P(z)$	Air pressure at height z
P_{ab}	Absolute pressure
p_{piezo}	Piezometric pressure
p_{static}	Static pressure
q''	Heat flux vector
R	Universal gas constant
R_a	Gas constant for air
S	Strain tensor
S_u	User defined energy source terms

T	Temperature
T	Viscous stress tensor
T_{ground}	Surface temperature
T_l	Laminar stress tensor
T_t	Turbulent stress tensor (Reynolds stress tensor)
T_z	Temperature at a height (z) above the surface level
$u(z)$	Wind speed at a height of z AMSL
u_1	Wind speed at a height of z_1 AMSL
V	Cell volume
v	Velocity vector
v_g	Grid velocity vector
x	Altitude
x_0	Reference altitude
z	Height above surface level
ε	Turbulent kinetic energy dissipation rate
ρ	Density
χ	Porosity

LIST OF ABBREVIATIONS

2-D	Two Dimensional
AHI	African Highlands Initiative
AMS	American Meteorological Society
AMSL	Above Mean Sea Level
AWS	Automatic Weather Station
CAD	Computer Aided Design
CFD	Computational Fluid Dynamics
DJF	December-January-February
GIS	Geographic Information System
IMS	International Mountain Society
ISA	International Standard Atmosphere
JJA	June-July-August
LES	Large Eddy Simulation
MRI	Mountain Research Initiative
NCAR	National Center for Atmospheric Research
NCEP	National Center for Environmental Prediction
NRF	National Research Foundation
RAM	Random Access Memory
RANS	Reynold Averaged Navier Stokes
SAEON	South African Environmental Observation Network

LIST OF FIGURES

LIST OF TABLES

1

Introduction

1.1 Background

It is well known that complex terrain, such as mountains, have a profound effect on local and regional climates (Fridley, 2009; Daly *et al.,* 2007; Beniston, 2006; Wood, 2000 and Swanson *et al.,* 1988). Mountainous terrain often consists of a number of climatic zones, which are usually associated with a high degree of biodiversity. According to Beniston (2006), some characteristics of complex topography are rapid and systematic changes in climatic parameters, in particular temperature and precipitation, over relative short distances (Becker and Bugmann, 1997).

Temperature might change rapidly over mountainous terrain because solar radiation is intercepted at different angles depending on the orientation of slopes. In regions that lie in the mid- and high-latitudes of the Southern Hemisphere, slopes oriented to the north receive more energy per unit area, and thus experience larger thermal amplitudes than slopes that have other orientations (Beniston, 2006). Temperature also decrease with increasing altitude at an average rate of 6.5 °C per 100 m in altitude, which is known as the average environmental temperature lapse rate specified for the International Standard Atmosphere (ISA) (International Organization for Standardization, 1975). Adiabatic cooling is related to the conservation of internal energy in a volume of air when work is performed (energy used) due to vertical pressure reduction and the subsequent expansion of the volume with height, and thus a drop in internal energy. Topographic lift of volumes of air might therefore also influence mountain temperatures. Because of surface heat radiation, mountains often serve as elevated heat sources, as diurnal temperatures in mountains are normally found to be higher than at similar altitudes in the free atmosphere (Beniston, 2006; Flohn, 1968).

Rapid changes in precipitation can take place over short horizontal distances when moist air masses flow over hills and mountains. Higher precipitation tends to fall at higher elevations because of convection, adiabatic cooling and condensation. Higher mountain slopes and tops are often associated with clouds (or fog) and sometimes heavy rainfall, whereas on a larger scale, surface observation networks show a deficit of rain at the lee side of hills and mountains (Wood, 2000). For example, a study conducted on precipitation in the Drakensberg mountains in South Africa had found that although the number of rain days and rainfall events had increased with altitude, daily and mean

rainfall from individual rainfall events were less on the top of the mountain, or escarpment, than along slopes and in the foothills. According to the author this challenges the general assumption of a gradual increase in rainfall with altitude in the Drakensberg mountains (Nel, 2007), as well as other mountains in the world.

Landforms, such as mountains, influence the flow paths of winds (Swanson *et al.,* 1988). Winds usually increase near the crests of mountains and reduce and are more variable in the valleys and at the lee side of mountains.

In summary, mountain climates are presumed to be governed by four main factors (Beniston, 2006; Barry, 1994). These factors include: (1) continentality (the proximity of a particular region to an ocean), (2) latitude, (3) altitude and (4) topography, of which altitude and topography are of particular importance (Beniston, 2006). Altitude is known to be the most distinguishing and fundamental contributor to mountain climates. This is due to the fact that atmospheric density, pressure and temperature decrease with altitude. Topographic features play a key role in determining local climates due to the slope, aspect and exposure of the surface to the climatic elements, such as solar radiation. The four factors named above tend to govern the redistribution of solar energy, as well as precipitation and temperature. Precipitation is highly sensitive to local site characteristics and even modest topographic characteristics can exert an often disproportionate influence on the amount of precipitation (Beniston, 2006). It is known that adiabatic cooling with elevation and cold-air drainage might add additional variance within mountain landscapes. This further decouples near-ground temperature regimes from regional atmospheric qualities (Fridley, 2008; Shreve, 1912; Barry, 1992 and Geiger *et al.,* 2003).

As a result, mountain climates might change significantly over relatively short horizontal distances as a result of increases in altitude and changes in land topography, and so do vegetation patterns and hydrological features (Beniston, 2006; Whiteman, 2000). A consequence of the climatic diversity of mountains is that mountain ecosystems are often endemic because many plant and animal species remaining isolated in habitat at high elevations, compared to lowland biodiversity that occupy climatic niches that are spread over wider surface areas (Beniston, 2006).

1.2 Mesoscale flow over mountains

According to Raymond (1986), the disruption of airflow in mountainous areas might be explained to some extent, although it is normally associated with very complex processes. For example, as a

volume of air approaches a mountain, its velocity could change due to topographically disturbed horizontal pressure gradients (Raymond, 1986; Smith, 1982). Compression and higher pressures on the windward side of a mountain caused by winds blowing towards the mountain normally divides the wind flow in such a way that it deflects towards the left and right of the mountain obstacle, while some flow might take place over the mountain. In large mountainous areas, wind velocities and directions might even be further modified by the Coriolis force, which is a planetary function of the rotation of the earth (Raymond, 1986).

It is interesting to note that wind flow over mountainous terrain is often associated with very consistent features. According to Stangroom (2004), surface winds experience a slight deceleration at the upwind foot of a positive vertical slope. If the slope in question is steep enough, this deceleration of surface winds may cause a small “separation bubble” on the upwind slope. Flow then accelerates up to the hilltop in the region where the maximum velocity is reached, from where it decelerates down the lee side of the hill where a negative vertical slope occurs. If the hill is sufficiently steep, a large “separation bubble” will also form on the lee slope of the hill, which will result in circular flow (vertically orientated vortex) allowing for lee side surface winds to flow in the opposite direction of the prevailing higher level wind. However, the depth and length of such a “separation bubble” is a function of the shape of the hill (Stangroom, 2004).

It has been shown that air flowing over complex terrain where several topographic scales are present may exhibit different features at different atmospheric levels (Barry, 2008). For example, a study done in the Tennessee River Valley (50 - 60 km wide) in the United States of America (USA) between the Cumberland Plateau (1000 m Above Mean Sea Level (AMSL)) to the northwest and the Great Smokey Mountains to the southeast, has identified three distinct airflow layers in the vertical. Firstly, below around 200 m AMSL in the valley, flow experienced no large-scale terrain effects -except for some channeling by minor ridges 100 m to150 m AMSL in altitude. In this layer, variation in wind speed and direction occur virtually independent of stability. At the next layer, about 800 m AMSL above the valley floor, the wind speed profile still resembles that of a rough plain surface, but wind direction was now affected by local topography and stability. At higher levels, wind speeds increased but wind directions tend to stay constant into the free air (Nappo, 1977, Barry, 2008). This demonstrates a gradual change from turbulence, with high variability, at local scale topographical patterns towards laminar flow in the free atmosphere, and emphasizes the difficulty of studying local scale variability in wind and other atmospheric variables in areas of complex topography. It is,

however, local scale variability that drives smaller scale mountain climates, in contrast to synoptic scale flow that has a smaller impact.

Local scale features of atmospheric variability plays an important role in the water budget, which originates from rainfall, of mountains. Mountains are often regarded as “water towers” because it is in mountains where water from topographical instigated rainfall accumulates to form rivers that transfer water to lower laying areas. According to Rife (1996) there are two main influences that mountains have on cloud formation and precipitation. The first is that mountains are regarded as obstacles to atmospheric flow. As stable airflow approaches and encounters a mountain, it is partially forced to ascend against the slopes of the mountain (Rife, 1996; Banta, 1990). Thus, if atmospheric conditions prevail, and in particular if the atmosphere is unstable and moist, clouds and precipitation may be produced due to forced-topographical uplift and cooling of the air. The stability of the atmosphere plays an important role in determining how a mountain will affect air flow. In particular, the stability of the atmosphere determines the maximum rate of topographic lift. The more stable the atmosphere, the lower the lift and the less vertical displacement will take place, and as a consequence more air flow will take place around the mountain in contrast to over the mountain (Rife, 1996). The second role that mountains play in the process of cloud formation and precipitation is that they are elevated heat sources (Rife, 1996; Banta, 1990 and Orville 1965; 1968). Mountain slopes might reach high levels AMSL in the atmosphere, and air in close contact with mountain slopes is warmed by heat emitted from these slopes. Therefore, air in close proximity of the mountain topography is normally warmer than that at the same elevation, but away from the mountain landscape. The heat from solar radiation emitted from a mountain produces relatively lower pressure in the air close to the mountain topography. These lower pressures might be of such an extent that they induce convergence, additional to topographical lift, of larger scale flow toward and over a mountain. For example, if air moves up the mountain slopes, and provided that there is sufficient heating and low stability, airflow and moisture / clouds will eventually rise further over the mountain peak, and could even break away from the slope to form updrafts into the free atmosphere above the mountain (Rife, 1996).

Mountains could further also be regarded as elevated moisture sources, because water vapor could be added to the atmosphere from evaporation and evapo-transpiration at the surface of a mountain. Therefore, air in the proximity of mountain surfaces is normally moister and less dense than air at the same level away from the mountain surface and over the mountain plains (Rife, 1996; Orville, 1968). This is especially the case at mountain slopes that faces the sun and where more heat is released, which is proportional larger than evaporative cooling. Moisture is also a critical component for the

formation of clouds (Rife, 1996). Mountains might even play a role in the initiation and development of thunderstorms. Thunderstorms are caused by three main mountain effects, namely, (1) topographic lift, (2) thermal forcing and (3) obstacle effects which include mountain blocking, flow deflection, and the production of lee-side flow disturbances. Mountain-induced flows mainly determine where convective cells will be initiated, and how the precipitation from the cells will be spatially distributed in and around the mountain (Rife, 1996 after Banta, 1990).

Apart from the effects of mountain topography, as discussed above, other mesoscale flow phenomena might also be associated with mountains. These mesoscale flow phenomena may include (1) mountain waves, (2) lee waves and clouds (3) rotors and rotor clouds (4) severe down slope windstorms and (5) lee vortices. These phenomena are mostly induced by stably stratified flow over higher topography. A discussion of each of these phenomena follows below:

1. ***Mountain waves***:

   Mountain waves (Figure 1-1) may be defined as atmospheric gravity waves that form when stable air flow passes over a mountain or mountain barrier (American Meteorological Society (AMS), 2011). It has been shown that stably stratified air that is forced to flow over a sinusoidal varying surface topography often results in oscillations, which may either be vertically propagating or vertically decaying, depending on whether the intrinsic wave frequency relative to the mean flow is less or greater than the buoyancy frequency (Holton, 2004).

2. ***Lee waves***:

   A lee wave is a special type of a mountain or gravity wave that forms when the mean mountain cross wind speed strongly increases with height, or when there is a low-level stable layer. Such conditions may also be associated with a layer near the surface in which vertically propagating waves are permitted, which is topped by a layer in which the disturbance decays in the vertical. Therefore, vertically propagating waves in the lower layer are reflected when they reach the upper layer. Under some circumstances the waves may be repeatedly reflected from the upper layer and the surface downstream of the mountain, leading to a series of standing waves or "trapped" lee waves (Holton, 2004). The presence of lenticular clouds (or trapped lee wave clouds) is often an indication of the existence of trapped lee waves behind a mountain barrier (Figure 1-1) (AMS, 2000).

3. ***Rotor clouds*:**

A rotor-cloud, as defined by the AMS, is a turbulent altocumulus type cloud formation that is mainly found at the lee side of large mountain barriers. The air inside the cloud rotates around an axis that is parallel to the mountain barrier. Rotors and rotor clouds are often associated with lee waves and lenticular clouds (AMS, 2000). Figure 1-1 gives a schematic illustration of the location of the formation of such rotor clouds.

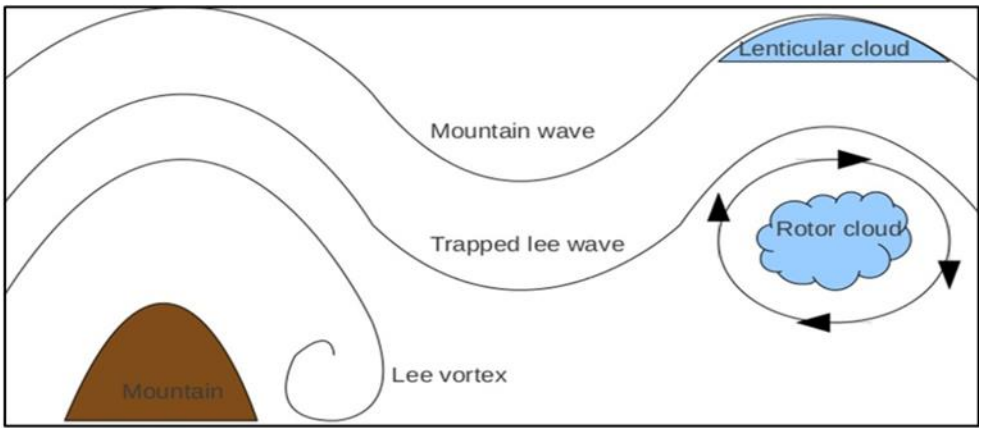

Figure 1-1:
An illustration indicating the formation and position of (1) mountain waves, (2) trapped lee waves, (3) lenticular clouds and (4) rotor clouds in air that flows over a bell-shaped mountain obstacle.

4. ***Severe down slope windstorms*:**

According to Holton (2000), strong down slope surface winds are sometimes observed along the lee slopes of mountain ranges. Partial reflection of linear vertically propagating gravity waves may produce enhanced surface winds under certain conditions, but it seems like nonlinear processes are essential to account for observed windstorms associated with stable flow over topography.

5. ***Lee vortices*:**

Atmospheric flow that passes a high mountain barrier often results in a low-level wake of reversed flow immediately downstream of the obstacle. When viewed from above (Figure 1-2) this wake can be identified as a pair of counter-rotating vortices circulating about a vertical axes (Epifanio, 2003).

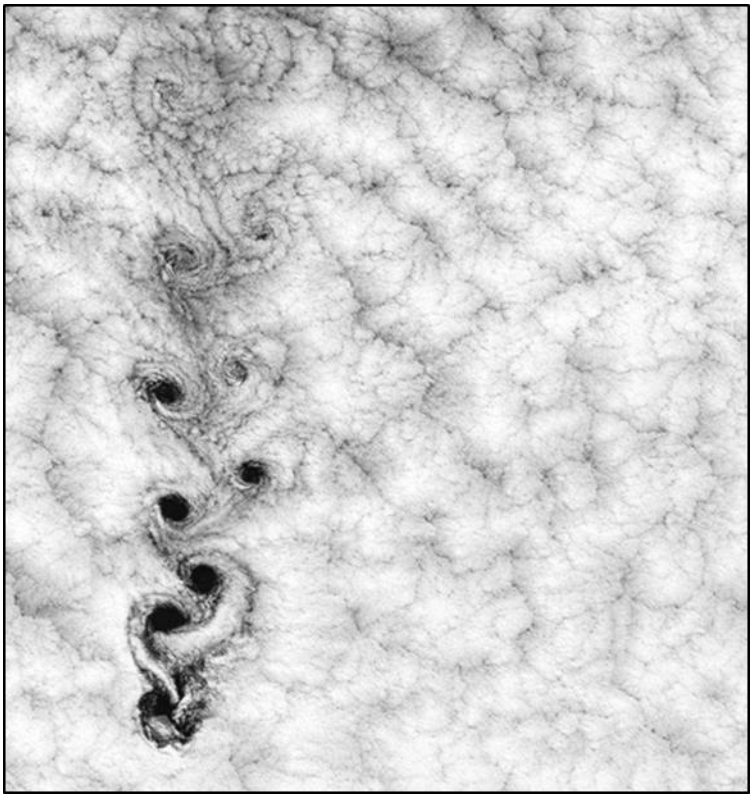

Figure 1-2:
A Landsat 7 satellite image of a vortex street downstream of the Alejandro Selkirk Island off the coast of Chile (Source: Epifanio, 2003).

1.3 Experimental model studies of airflow over a three dimensional hill.

Experimental model studies done on stratified flow over (and/or around) idealized three dimensional bell-shaped hills have shown that the criteria for the occurrence and location of separation in air flow at the lee side of a hill are modulated by the average slope of the hill as well as the ratio between the wavelength of the lee waves and the length of the hill in the direction of the flow. For moderately sloped hills, it was shown that the Froude number (Fr) prescribes separation, hydraulic jump, lee wave formation and rotor formation (Ayra and Hunt, 1979). Fr is a dimensionless number that dependents on the flow speed of the air, the Brunt-Vaisalla frequency (or the static stability parameter) and gravitational acceleration. For flow that takes place over and/or around a hill of fixed height, relatively low Fr values are indicative of stable atmospheric conditions, whereas relatively high Fr values are indicative of unstable conditions.

Ayra and Hunt (1979) have shown that at low Fr values ($0.1 < Fr < 0.2$), flow is constrained to move in horizontal planes around the hill, with the exception of narrow regions near the hill top where flow

takes place over the top of the hill. Air flow separation occurs just beyond the hill top. Under these conditions the wake region behind the hill tends to have two dimensional (2-D) characteristics consisting of a symmetric pair of nearly vertical oriented vortices. As Fr is increased (Fr > 0.2), more flow moves over the top of the hill while, at the same time, the region where the flow goes over the hill top becomes increasingly broader. The point of separation of the central streamlines passing over the hill top occurs farther downstream as Fr is increased. At a Fr value of 0.9, nearly all of the flow in the center-plane moves over the hill top, and separation only takes place well beyond the lee side base of the hill. When Fr=1, the flow again tends to separate just past the top of the hill. As Fr values are further increased (Fr>1), the flow separates near the hilltop and the size of the recirculation zone and wake region grow in both the lateral and vertical directions. If Fr is increased to a value of Fr=1.7, the flow almost resembles neutral flow (Fr=∞), except for the fact that streamlines are more closely spaced and they lose elevation faster in the wake region than those in neutral flow. In the neutral case (Fr=∞) flow tend to separate slightly upwind of the hilltop and upslope flow can be found on the lee side of the hill (Ayra and Hunt, 1979).

Air flow separation is caused by adverse pressure gradients that exist due to the geometry of the hill and is mainly modulated by the average slope of the hill as well as by the ratio of the fundamental wave length of the lee waves to the half-length of the hill. When the average slope is small (slope<<1), separation will not readily occur. However, when the slope is large (slope>>1) separation is very likely to occur. For moderately sloped hills, the occurrence and location of separation is highly dependent on Fr values (Ayra and Hunt, 1979).

It is important to note that these results were obtained from considering an idealized hill geometry and may therefore differ significantly from values obtained from real mountains with much more complex geometry.

1.4 Motivation for the research

Changes in the global climate have been widely observed over the past 150 years, including in South Africa (IPCC, 2007). It is also widely accepted that these changes are the result of anthropogenic induced warming of the atmosphere. Although climate model projections are pointing towards a general drying over the western parts, and normal to wetter conditions over the east of South Africa (IPCC, 2007), it has not been verified to date, especially over high topographical regions where observations are limited. Rautenbach and Mphepya (2005) have shown that, for at least in some parts of South Africa, a marked seasonal shift in rainfall has been identified in observations. It has also been

shown that near-surface temperatures are already on the increase over most of South Africa. It is widely expected that changes in ambient temperature and rainfall will have an effect on the physical characteristics of an area (e.g. soil characteristics and water runoff), its biodiversity (e.g. plant and animal species habitat structure) and the use of water and other natural resources by humans.

Because of the long-term nature of detecting climate change, it is crucial that monitoring sites be located in climate sensitive areas where the highest probability exists for detecting climate change. Mountainous areas are especially important in this regard, since enhanced heating of the atmosphere will be more obvious at higher altitudes compared to near surface changes, especially above dew point temperature levels in the atmosphere. This is because surface heating might be absorbed and reduced by evaporative cooling, while the heat absorbed are transferred to higher atmospheric levels through latent heat fluxes. Latent head absorbed by evaporation at the earth's surface will then be released at higher altitudes when condensation takes place at dew point temperatures, which in turn, will add to temperature increases at higher altitudes. This implies that anthropogenic warming at the surface are transferred to higher altitudes, where the warming will be much more obvious to observe.

Mount Kilimanjaro could be considered as an example of climate shifts since altitudinal shifts in some of the ecological zones were recently observed on the slopes of the mountain (Hemp, 2005). The importance of mountains as areas of ecological monitoring has also been emphasized through the activities of institutions such as the African Highlands Initiative (AHI) in Ethiopia[1], as well as through many activities of the International Mountain Society (IMS) (Switzerland)[2] and the Mountain Research Initiative (MRI) (Switzerland)[3].

In order to monitor the effects of climate change on mountains it is important to study a number of mountains in many different regions in the world, as each region may be affected by climate change differently.

This study is concerned with flow over a particular mountain called Mariepskop (direct translation: "Marieps hill"), which has a horizontal spatial dimension of approximately 5 km by 3 km, and is approximately 1900 m high in altitude AMSL. Mariepskop is situated on the border between the Mpumalanga and Limpopo Provinces of South Africa. It consist of a high mountain peak that is partly

[1] http://www.cgiar-ilac.org/content/african-highlands-initiative-ahi
[2] http://www.mrd-journal.org/default.asp
[3] http://www.mri.scnatweb.ch

isolated towards the west from the rest of the Drakensberg mountain range which forms the eastern escarpment of South Africa, making it ideal for studying the effects of atmospheric flow dynamics over the mountain and its associated climate, with limited interference in the predominantly westerly flow from the adjacent topography. Mariepskop also has many endemic fauna and flora species making it an ecologically sensitive mountain. To date, only limited studies had been conducted regarding the climate of Mariepskop, and none of these addressed atmospheric flow dynamics over the mountain.

This study will contribute to the currently limited understanding of air flow over Mariepskop, and will form a basis for further future climate studies on Mariepskop. It is especially the author's wish that the study may further contribute to conservation efforts on the mountain.

1.5 Current observations on Mariepskop

This dissertation formed part of a multidisciplinary research project aiming to study the effects of climate change on Mariepskop and its natural biodiversity. The project was funded by the National Research Foundation (NRF) with its South African Environmental Observation Network (SAEON) national facility; the project involves botanical, zoological, geomorphological and social facets. As part of the project, three Automatic Weather Stations (AWSs) were erected at different elevations on Mariepskop. Weather stations were erected at 700 m, 1000 m, 1300 m (Figure 1-3) 1600 m (Figure 1-4), and 1900 m AMSL. The last three stations, at higher altitudes, were considered for this study – also since the lower level stations were erected after the start of the research. What was of interest is that each weather station collects rainfall, near-surface temperature, wind speed, wind direction, soil moisture and solar radiation data on an hourly basis.

Figure 1-3:
The Automatic Weather Station (AWS) at 1300 m Above Mean Sea Level (AMSL) on Mariepskop (the 1900 m AMSL peak of Mariepskop can be seen in the background.

Figure 1-4:
The Automatic Weather Station (AWS) at 1600 m Above Mean Sea Level (AMSL) and the team responsible for the installation of this weather station: From left to right: Colin Patrick (from the game farm Maholoholo), Prof Hannes Rautenbach (promoter), Prof Willem Ferguson (University of Pretoria's Centre for Environmental Studies – CFES), Ilze Pretorius (author and leader of this study), Johan Pretorius (the authors husband), and Hanneke Pienaar-Steenekamp (a friend who participated).

1.6 Aims and objectives of the study

The aim of this study is to try explaining the location of climate zones on Mariepskop by analyzing model simulations of atmospheric flow dynamics over Mariepskop using a Computational Fluid Dynamics (CFD) model. The objectives of the study are listed below:

OBJECTIVE 1:

To determine estimated predominant synoptic flow over Mariepskop over a climatic period at different vertical layers.

This was achieved by the weighted interpolation of National Centre for Environmental Prediction / National Centre for Atmospheric Research (NCEP/NCAR) reanalysis data, over the past 30-years, around Mariepskop (Kalnay and others, 1996) in order to locate wind direction, wind speed and near-surface temperature values at the centre of the Mariepskop domain for the summer, December-

January-February (DJF), and winter, June-July-August (JJA), seasons. Data were obtained for both the 700 hPa and the 850 hPa atmospheric pressure levels.

OBJECTIVE 2:

To use NCEP/NCAR reanalysis data to generate seasonally representative boundary condition input for the CFD model in order to generate mesoscale wind simulations output over the complex terrain of Mariepskop, and to verify the CFD model output against station observations.

Dominant wind directions at both the 700 hPa and 850 hPa atmospheric pressure levels, as well as the dominant near-surface temperature was used as boundary conditions for input to the CFD model (also known as STAR-CCM+).Although CFD models have traditionally been used for engineering applications, CFD models have been applied more regularly in the meteorological realm over the last few years. CFD is especially used for wind flow modeling over complex terrain, for wind-farm modeling and fire prediction applications (Stangroom, 2004; O'Sullivan et al., 2010; Forthofer et al., 2003; Watson et al., 2004, Stander, 2008). The advantage of CFD models are that they capture flow over complex terrain quite well and that they can be run at very high resolutions over reasonable acceptable time frames, compared to other available fine resolution regional atmospheric models. Note that the CFD model used in this study does not contain code for moisture processes, and is therefore not suitable for rainfall simulations. In order to determine model performance, wind simulations were verified against station records at the three AWSs at 1300 m, 1600 m and 1900 m AMSL.

OBJECTIVE 3:

To use wind simulations and aerial photographs as guidance to identify mountain areas with higher rainfall, and to use this to draw preliminary conclusions on the local climate characteristics of Mariepskop.

Convection properties in airflow will be used as guidance towards identifying areas of higher mountain rainfall, while aerial photographs will also be examined with the objective to draw preliminary conclusions on the local climates of Mariepskop.

1.7 Organization of the report

1. Synoptic disturbances over South Africa, the Mariepskop site, the reanalysis data obtained for the study area and the weather stations that have been installed on Mariepskop are all introduced and discussed in Chapter 2.

2. In Chapter 3 the CFD model used to simulate flow over Mariepskop is introduced. The governing equations and assumptions of the model are discussed, as well as the initial and boundary conditions used for the simulations in this study.

3. The results and verification of the CFD model are dealt with in Chapter 4. The model simulation output is verified against observations, as far as possible, using data that was logged by the three AWSs at different elevations on Mariepskop. Aerial photographs are also used to draw conclusions on local rainfall distribution and the climate of Mariepskop.

4. Chapter five contains concluding remarks and recommendations.

5. Chapter six lists all the references cited in this document.

2

Observational data and climate

2.1 Synoptic patterns over Mariepskop

According to Ross *et al.*, (2001), the synoptic systems affecting the Lowveld of the Mpumalanga Province of South Africa (where Mariepskop is situated) can be divided into four categories, namely (1) easterly waves / lows, (2) westerly disturbances (including troughs and cut-off lows), (3) ridging anticyclones and (4) continental anticyclones.

Tropical disturbances affecting South Africa, like easterly waves and lows, are predominantly austral summer systems (Tyson and Preston Whyte, 2000). In contrast, westerly disturbances are located more southwards and are predominantly more frequent during the austral winter (Garstang *et al.,* 1996; Tyson *et al.,* 1996; Ross *et al.,* 2001). Ridging anticyclones associated with the eastwards passage of cold front systems occur relatively consistently throughout the year (Ross *et al*., 2001), but with a higher frequency of in October and February (Tyson and Preston Whyte, 2000). Continental anticyclones show a clear annual cycle with a peak occurrence during autumn and winter (Ross *et al.,* 2001). For Mariepskop, it is especially ridging highs, associated with easterly and south-easterly onshore flow, and continental systems allowing for westerly flow towards the escarpment, that are of importance.

2.2 Study domain description

Mariepskop, with its central location at longitude 24°32'34.57"S and latitude 30°52'07.38"E, and its altitude of approximately 1900 m AMSL (Figure 2-1), is located at the northern edge of the Drakensberg mountain range in the Mpumalanga Province of South Africa, which also forms the eastern escarpment of South Africa that divides the higher altitude and industrialised Highveld to its west, and the lower lying Lowveld characterised by its diversity of natural resources to its east. The 1900 m mountain is characterized by complex topography associated with mesoscale atmospheric circulation and different climatic zones. It therefore hosts a high degree of biodiversity. What makes Mariepskop an ideal study site is the fact that its peak is higher than the surrounding escarpment to the east, and that its foothills extend well into the Lowveld at about 700 m AMSL and 231 km from the Indian Ocean. It is therefore also well situated for studying airflow exchange between the Highveld and the Lowveld.

Figure 2-1:
A visible satellite image of Mariepskop with its central location at longitude 24°32'34.57"S and latitude 30°52'07.38"E, with reference to the Mpumalanga and Limpopo Provinces of South Africa. (Source: Google Earth)

2.3 Observations

Before and during commencement of this research, three AWSs were erected at different elevations on Mariepskop. The AWSs were erected at 1300 m, 1600 m and 1900 m AMSL. Each weather station electronically recorded rainfall, temperature, wind speed, wind direction, soil moisture and solar radiation data on hourly intervals.

The wind speed and wind direction data at each of the three elevations were used to verify the output of the CFD model used to model atmospheric flow over Mariepskop.

2.4 Synoptic data

Long-term (1981 to 2011 = 30 years) NCAR-NCEP reanalysis wind data (Kalnay et al. 1996) at two atmospheric pressure levels (850 and 700 hPa), as well as near-surface temperature reanalysis data were obtained for the Mariepskop affinity for the austral summer (DJF) and austral winter (JJA) seasons. A disadvantage of the data is that the spatial coverage of the data is at a course resolution of 2.5° x 2.5°, and that data points are therefore not located in close proximity of the study domain. Nevertheless, NCAR-NCEP reanalysis data is one of the few data sets available for Mariepskop, exhibiting a consistent long record at different atmospheric levels in the vertical. The NCEP/NCAR facility was used to obtain synoptic scale wind flow data in the proximity of Mariepskop (Figure 2-2) of

the upper (700 hPa) and lower (850 hPa) atmosphere, as well as long-term near-surface temperature for the time 30-year time period of 1981 to 2011.

A nearest neighbour weighting method was employed in finding an average value at the centre of the Mariepskop domain (24°32'34.57"S and 30°52'07.38"E) for each of the three NCAR/NCEP reanalysis variables (u-wind, v-wind and near-surface temperature). Six-hourly u-wind and v-wind values were used to calculate wind direction and wind speed frequencies for the summer and winter seasons at both the 850 hPa and 700 hPa levels. Near-surface temperature values were used in an effort to detect historical temperature trends. However, all these variables were also used as boundary forcing to CFD model simulations over the same period of 30-years.

Figure 2-2:
The four National Centre for Environmental Prediction / National Centre for Atmospheric Research (NCEP/NCAR) reanalysis data points locations used, at a spatial resolution of 2.5° x 2.5°, in the proximity of Mariepskop from where wind and temperature data values at the 850 hPa and 700 hPa pressure levels were interpolated to a central Mariepskop point at six hourly intervals over a 30-year time period (Source: Google Earth).

2.5 Wind observations

The wind roses in Figure 2-3 depict summer season wind directions at Mariepskop for the 850 hPa (left) and 700 hPa (right) levels as calculated from a 30-year (1981- 2011) data record.

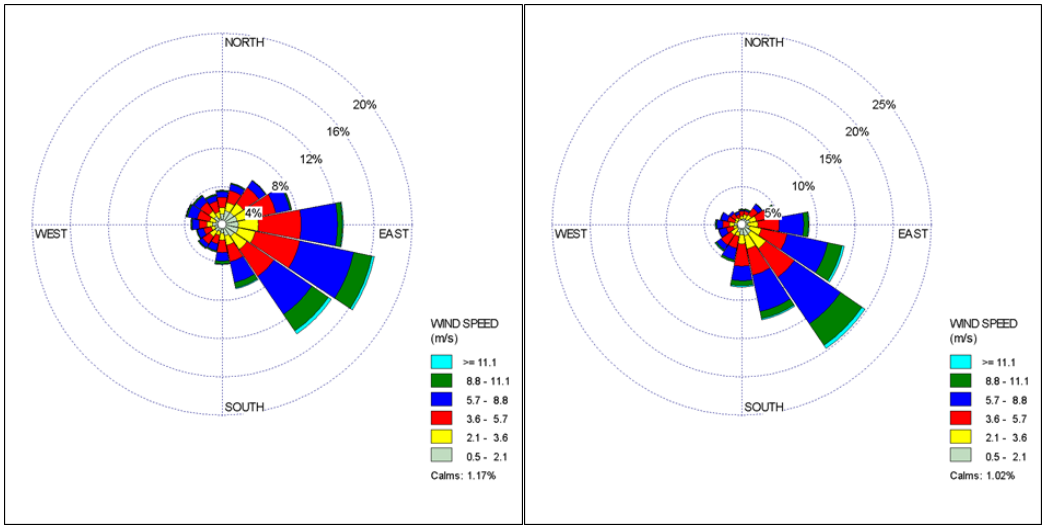

Figure 2-3:
Long term averaged (1981- 2011) summer season (December-January-February: DJF) wind roses for Mariepskop at the 850 hPa (left) and 700 hPa (right) atmospheric pressure levels, as interpolated from National Centre for Environmental Prediction / National Centre for Atmospheric Research (NCEP/NCAR) reanalysis data.

From Figure 2-3 it is clear that the east-south-east and south-east wind directions are by far the most prominent wind directions observed. These findings agree well with the results of a study done on circulation during for the period 1994-1998 over the Lowveld of South Africa by Ross *et al.,* (2001). South-easterly winds normally occur in association with both continental and ridging anticyclonic circulation.

The long-term wind class frequency distribution, as obtained from the NCAR/NCEP reanalysis data for the 850 hPa and 700 hPa summer winds, are indicated in the histograms of Figure 2-4.

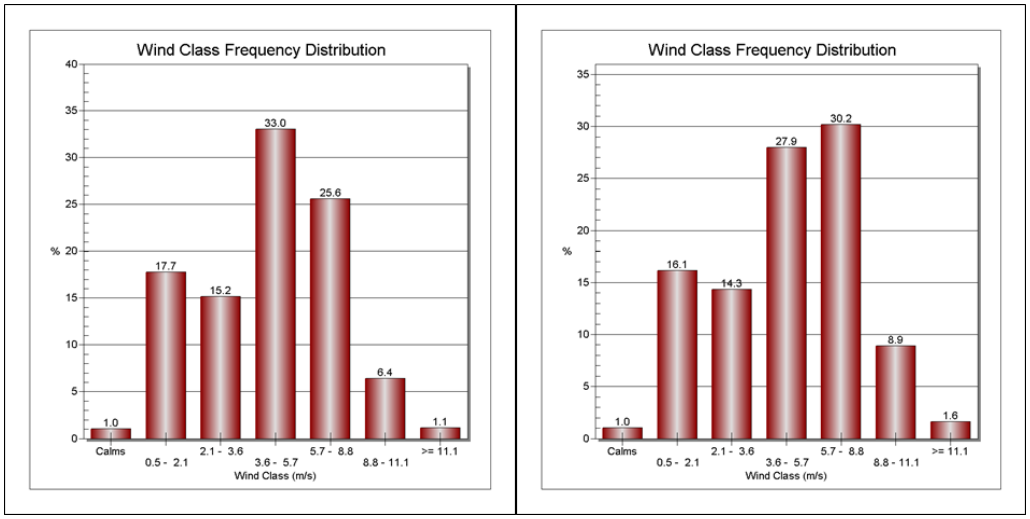

Figure 2-4:
Long term averaged (1981- 2011) summer season (December-January-February: DJF) wind class frequency distribution graphs for Mariepskop at the 850 hPa (left) and 700 hPa (right) atmospheric pressure levels as interpolated from National Centre for Environmental Prediction / National Centre for Atmospheric Research (NCEP/NCAR) reanalysis data.

The wind class frequency distribution histograms denote the frequency of occurrence of different wind speed classes. Figure 2-4 illustrates that the dominant wind speed class at the 850 hPa level for summer is between 3.6 - 5.7 $m.s^{-1}$, with an frequency of occurrence of 33%. This class is followed by the 5.7 - 8.8 $m.s^{-1}$ class, which prevailed for 25.6% of summer days. Calm days only occurred at about 1% of the time, whereas winds greater or equal to 11.1 $m.s^{-1}$ occur on 1.1% of summer days at the 850 hPa level.

For the 700 hPa level the two dominant summer wind speed classes were the 5.7 - 8.8 $m.s^{-1}$ (30.2%) and the 3.6 - 5.7 $m.s^{-1}$ (27.9%) classes. The wind speeds at the 700 hPa level are therefore greater and thus stronger, on average, than at the 850 hPa level. Calm days occurred at 1% of the time, which is the same as for the 850 hPa level, and wind speeds above 11.1 $m.s^{-1}$ were 0.5% more abundant at the 700 hPa level, at 1.6%.

High wind speeds exceeding 6 $m.s^{-1}$ are often associated with ridging anticyclonic conditions. This is due to steep pressure gradients, which also induce strong moisture advection from the Indian Ocean.

The associated long-term wind roses for the winter season for the period 1981 - 2011 are shown in Figure 2-5.

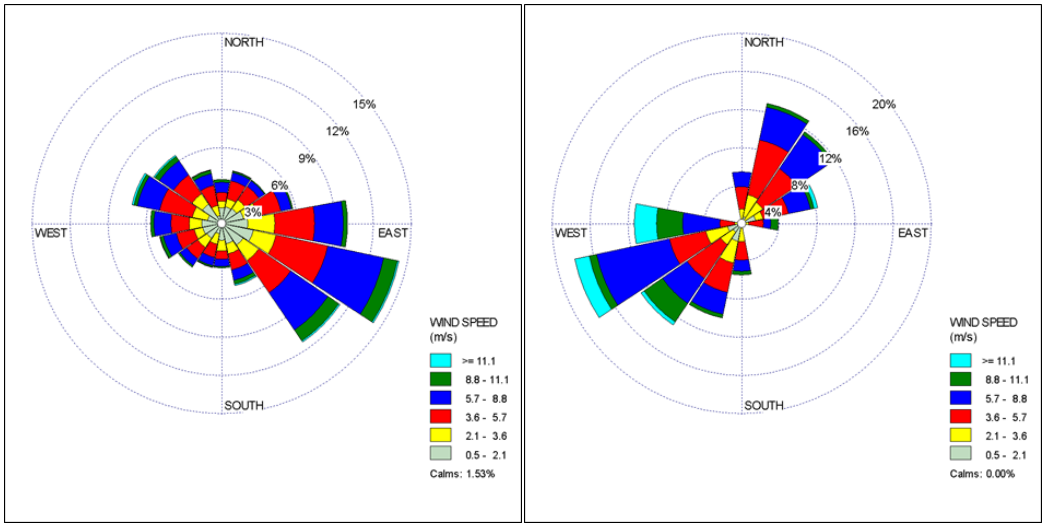

Figure 2-5:
Long term averaged (1981- 2011) winter season (June-July-August:JJA) wind roses for Mariepskop at the 850 hPa (left) and 700 hPa (right) atmospheric pressure levels, as interpolated from National Centre for Environmental Prediction / National Centre for Atmospheric Research (NCEP/NCAR) reanalysis data .

According to Figure 2-5, both the 850 hPa and 700 hPa levels show a more varied wind direction distribution during winter, as compared to summer. At the 850 hPa level the dominant wind directions were still east-south-east (14%), south-east (11%) and east (10%), but a more prominent portion of the winds were directed west-north-west (8%) and north-west (7%).

The 700 hPa winter wind direction distribution differed significantly from the summer distribution. In this case the dominant wind direction was west-south-west (18 %), with equal proportions from the south-west and north-north-east (13%), in second place. The winds from the west-south-west and south-west had the greatest wind speeds, with a relatively large proportion of the winds from these directions exceeding speeds of 11 $m.s^{-1}$, whereas winds from the opposite direction reached these speeds less often.

The predominant south-easterly flow seen in the 850 hPa winter wind rose of Figure 2-5 is due to the influence of ridging anticyclones, which occur fairly evenly throughout the year. The north-westerly wind directions at the 700 hPa atmospheric level are caused by westerly waves and cold front propagation which affect the Lowveld mainly during the spring and winter seasons.

The wind class frequency distribution histograms of long-term winter winds are indicated in Figure 2-6.

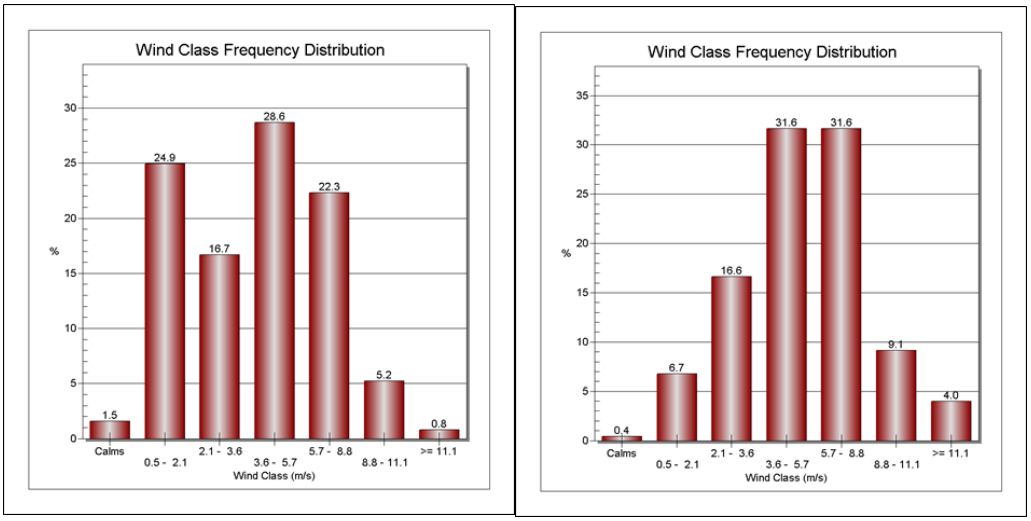

Figure 2-6:
Long term averaged (1981- 2011) winter season (June-July-August: JJA) wind class frequency distribution graphs for Mariepskop at the 850 hPa (left) and 700 hPa (right) atmospheric pressure levels as interpolated from National Centre for Environmental Prediction / National Centre for Atmospheric Research (NCEP/NCAR) reanalysis data.

From Figure 2-6 it is clear that the dominant winter wind speed class at the 850 hPa level is the 3.6 - 5.7 $m.s^{-1}$ class (28.6%). At the 700 hPa level the dominant wind speed classes are the 3.6 – 5.7 $m.s^{-1}$ and 5.7 - 8.8 $m.s^{-1}$ classes, each with a frequency of occurrence of 31.6 %. In general, the winds at the 700 hPa level reach higher speeds with 4% of total winds falling in the > 11.1 $m.s^{-1}$ class (relative to the 0.8% at the 850 hPa level). The 700 hPa level experiences calm conditions at only 0.4% of the time during winter months, whereas the 850 hPa level experience these conditions 1.5% of the time.

2.6 Near-surface temperature observations

The DJF and JJA averaged (from 6-hourly data) long term (1981-2011) near-surface temperatures over Mariepskop are depicted in Figures 2-7 and 2-8.

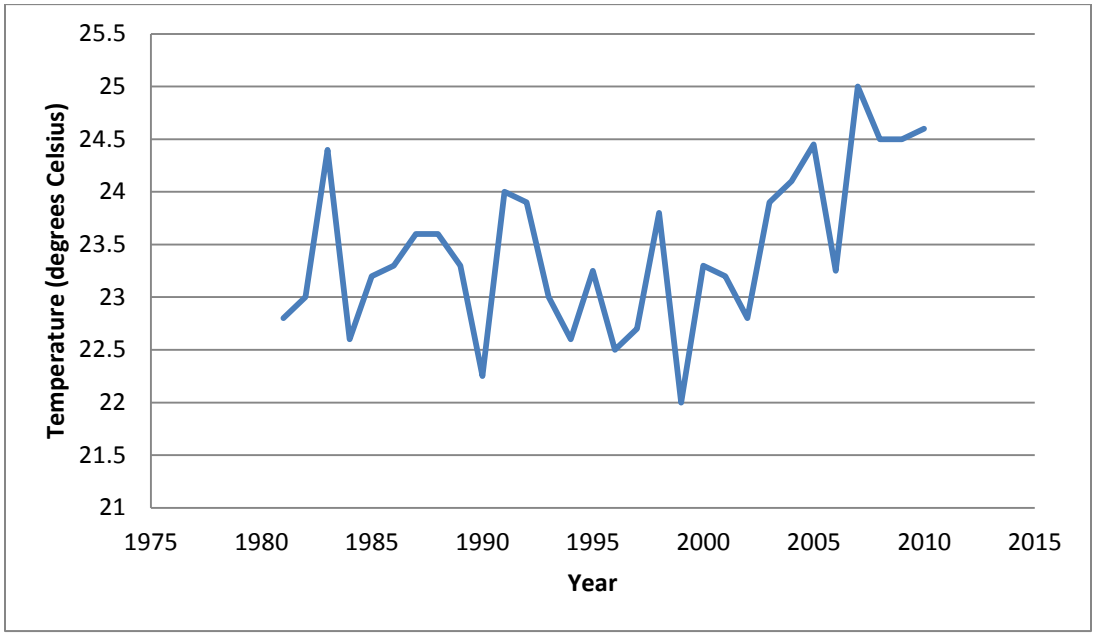

Figure 2-7:
Long term averaged (1981- 2011) summer season (December-January-February: DJF) near-surface temperatures for Mariepskop as interpolated from National Centre for Environmental Prediction / National Centre for Atmospheric Research (NCEP/NCAR) reanalysis data .

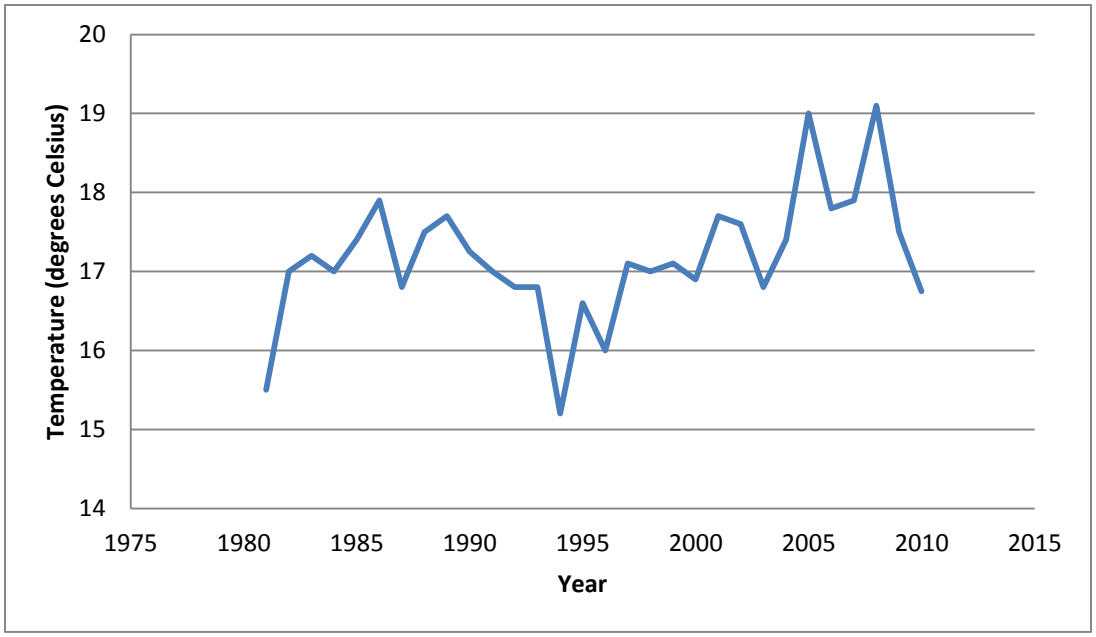

Figure 2-8:
Long term averaged (1981- 2011) winter season (June-July-August: JJA) near-surface temperatures for Mariepskop as interpolated from National Centre for Environmental Prediction / National Centre for Atmospheric Research (NCEP/NCAR) reanalysis data .

The average summer near surface temperature over the past 30 years at Mariepskop is around 23.5 °C, while the average winter temperature over the past 30 years is 17.2 °C. Both temperature time series show a positive trend which is particularly noticeable since the year 2000 in the summer graph, and since the mid-nineties in the winter graph.

Please note that these temperature values were interpolated, using an inverse distant weight factor, from NCEP/NCAR grid points. Some of these grid points are located on the escarpment / Highveld and some in the Lowveld (see Figure 2-3). Just like the winds in figures 2-4 to 2-7, they are therefore not representative of local Mariepskop climates, but are rather a reflection of the averaged large or synoptic scale climates at a central point at Mariepskop. Such large scale climates might, however, be a great value if they could serve as lateral boundary input to a fine resolution model with the objective to simulate local climate variability over the Mariepskop domain.

3

Dynamical downscaling of climate

3.1 The Computational Fluid Dynamics model

STAR-CCM+ is a modern engineering CFD package, and recently became the first commercial CFD package in the world that could mesh and solve flow dynamics and thermodynamics problems with over one billion finite volume cells. It was chosen as the model of choice for this study as it is capable of handling fine resolutions and because of its relative ease of operation.

According to White (2006), CFD is the numerical analysis of fluid flow on a digital computer where one replaces the partial differential equations of momentum, continuity and energy by algebraic approximations applied at a finite number of discrete mesh points. White (2006) stated that, given certain restrictions such as the choice of the Reynolds number as well as mesh spacing and the time increment, the results can be remarkably accurate. Laminar flows can be simulated with near exact accuracy, and is subject only to limitations of computer size and speed and possible irregularities in the shape and flow of the region of study. On the other hand, turbulence can only be computed or simulated accurately by direct simulation at very low Reynolds numbers. At high Reynolds numbers, only approximations of turbulent flow can be made by making use of a variety of turbulence modeling assumptions (White, 2006), which are regarded as suitable for the purpose of this study.

3.2 The Mariepskop domain

The terrain of Mariepskop was captured in three dimensions by making use of Geographical Information System (GIS) shape files that were first converted to .dxf format and then converted to three dimensional .stl files in an engineering drawing program. The domain selected across Mariepskop is around 27 km x 27 km, and the lowest point in the domain has an elevation of 520 m AMSL, whereas the highest point is located just below 2000 m AMSL. The three dimensional terrain model that was designed for the downscaling simulations of Mariepskop can be seen in Figure 3-1. Mariepskop is the highest mountain is visible (red in Figure 3-1) at the centre of the domain. The coordinates of the south western point of the domain are

approximately 24°39'49.57"S and 30°43'3.29"E whereas the coordinates of the north eastern point of the domain are approximately 24°26'1.01"S and 30°59'45.53"E.

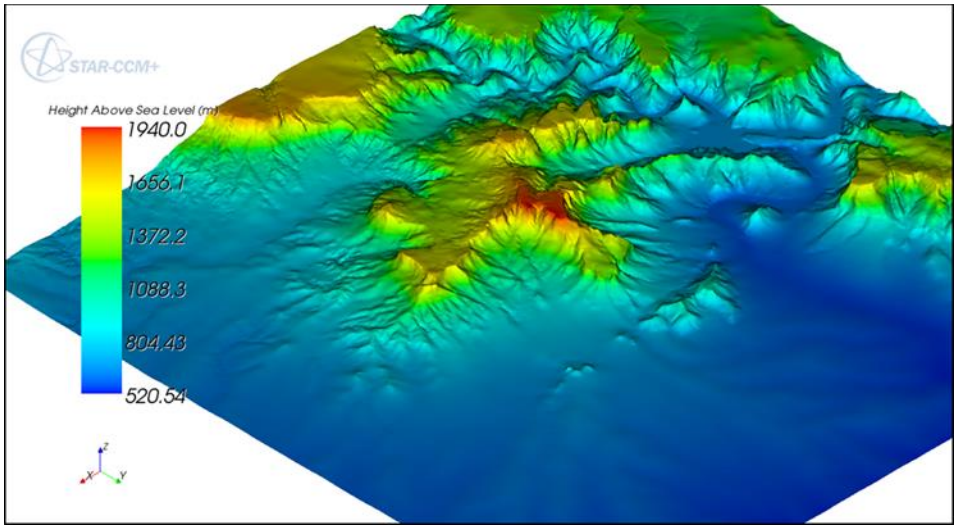

Figure 3-1:
The Mariepskop domain and topography selected and shaped for use in STAR-CCM+ Computational Fluid Dynamics (CFD) downscaling model simulations. The colours indicate height in meters Above Mean Sea Level (AMSL).

3.3 The Mariepskop volume mesh

In order to capture the volume of the fluid to be modeled by the CFD model (in this case the air around Mariepskop) the terrain geometry needed to be subtracted from a volume block around Mariepskop using an engineering Computer Aided Design (CAD) program. The initial terrain surface was of a poor quality and therefore a surface wrapper was used in conjunction with a surface re-mesher to provide a closed, manifold, non-intersecting surface.

The volume mesh of the model consists of tetrahedral cells and prismatic cells. The tetrahedral cells make up the bulk of the volume mesh, while the prismatic cells are located only on the boundary between the Mariepskop terrain and the atmosphere in direct contact with the mountain. The tetrahedral cells were used because they are not only the fastest volume mesh generator in the STAR-CCM+ program, but also the generator that uses the least amount of computational memory. Therefore, for a large domain like in this study, this type of volume cell is recommended. The prismatic cells are used in order to generate orthogonal prismatic cells next to the geometry surfaces, and are required to accurately simulate turbulence (see STAR-CCM+ user guide, 2011). At the base of the domain (next to geometry surfaces) the velocity

profile changes rapidly and turbulence have large effects. The prismatic cells are very thin in the vertical direction, but longer in the wind flow direction. Therefore these cells account for the large changes in gradient without being excessively computationally expensive (Stangroom, 2004).

Two volume blocks were drawn on the Mariepskop terrain itself, and the mesh resolution was increased within these two blocks. The smallest of the two volume blocks which was located in the inner mountain domain had the highest resolution to capture the detailed topography of the mountain. In this block the smallest volume cells have a resolution in the order of 6 m and the prismatic cells have a vertical resolution in the order of 0.4 m. Cells from the smallest volume block increased in volume towards the larger volume block, which was located around the smaller block (Figure 3-2). Figure 3 2 to Figure 3-6 show the volume mesh of Mariepskop. From Figure 3-2 to Figure 3-4 each figure is amplified closer to Mariepskop itself to illustrate the higher resolution of the mesh as one move to the mountain. Figure 3-5 and 3-6 illustrate a side view of the eastern and western slopes of the Mariepskop volume mesh. The y-direction on the axis indicated in the bottom left corner of the figures points in a northerly direction. It is important to note that the two outer blocks that are visible in Figure 3-2 and 3-3 are merely the attempt of the STAR-CCM+ model to increase the mesh resolution gradually.

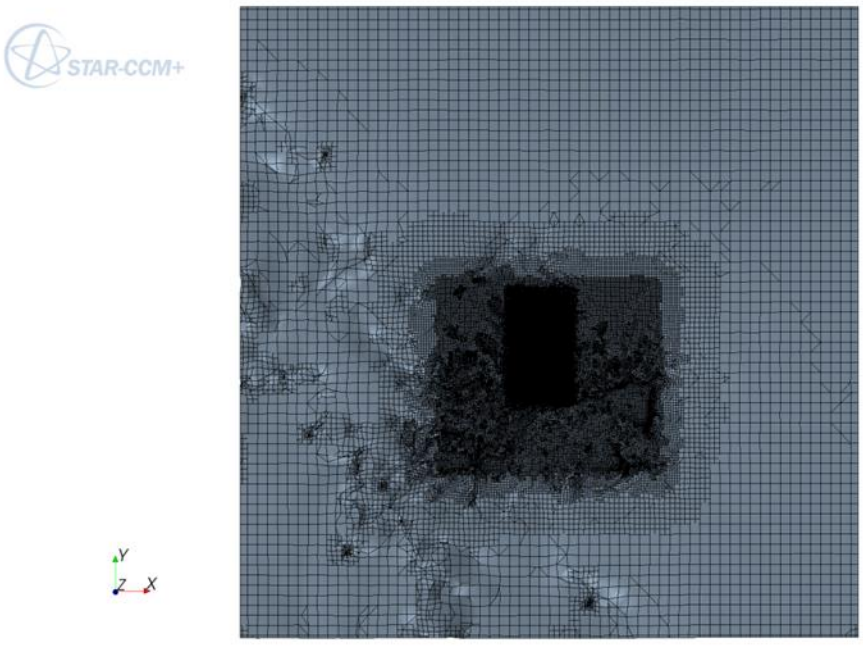

Figure 3-2:
A view from above of the volume mesh over the entire Mariepskop domain. Mariepskop lies in the dark area, or block volume, where the resolution is higher than that of the surrounding areas.

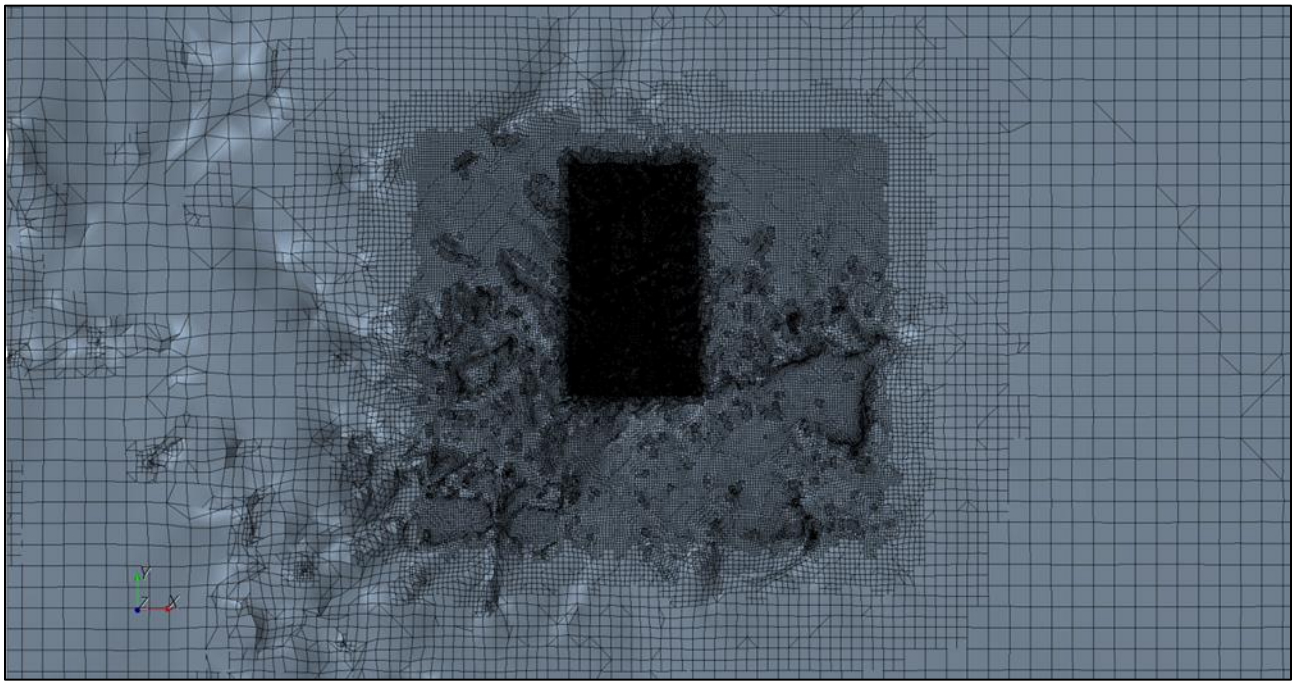

Figure 3-3:
A view from above of the volume mesh over Mariepskop, but amplified towards the mountain area. The two darker block volumes where the mesh resolution has been increased can now be distinguished.

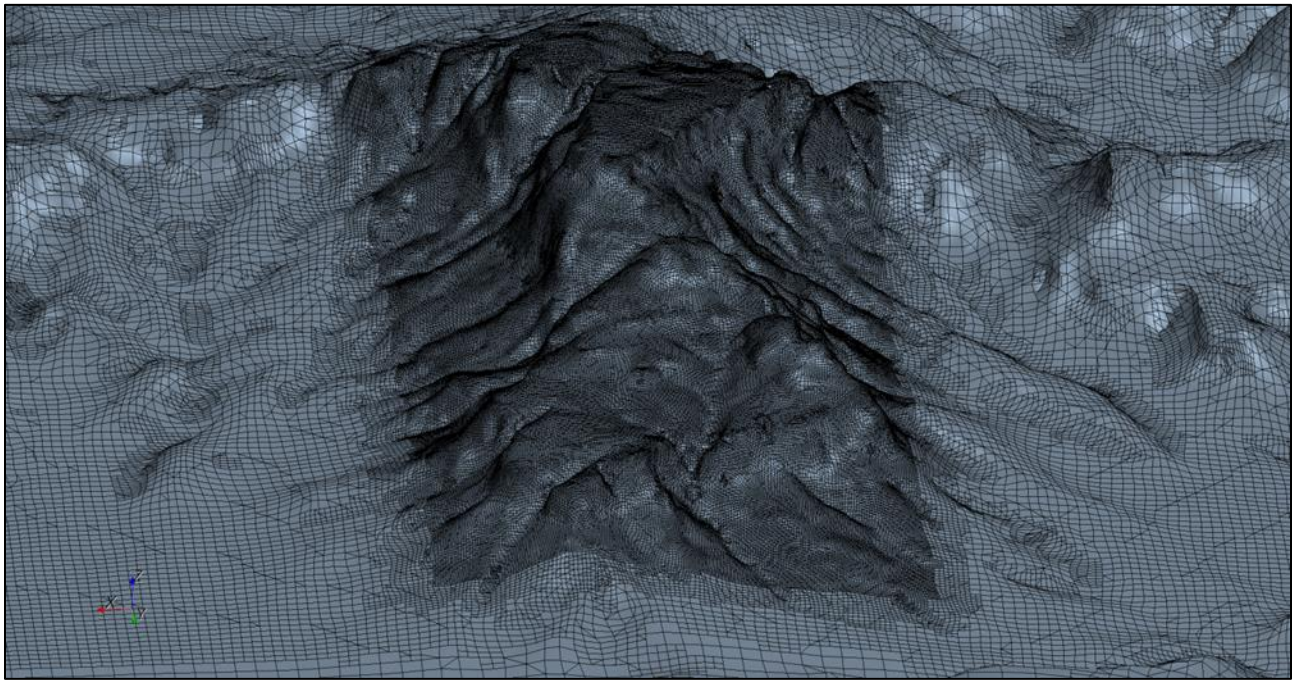

Figure 3-4:
A view from the north of the smallest volume block mesh with the highest resolution of approximately 6 m x 6 m around the Mariepskop mountain domain.

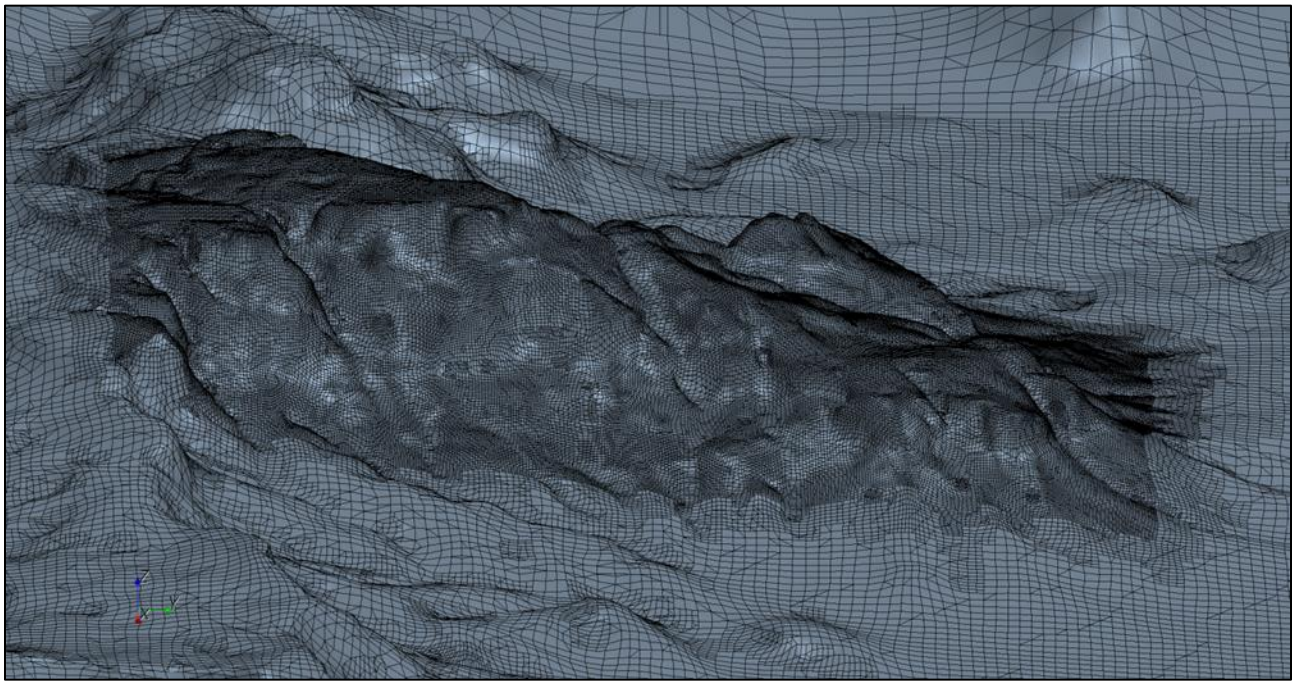

Figure 3-5:
A side view of the eastern slope of the Mariepskop block mesh.

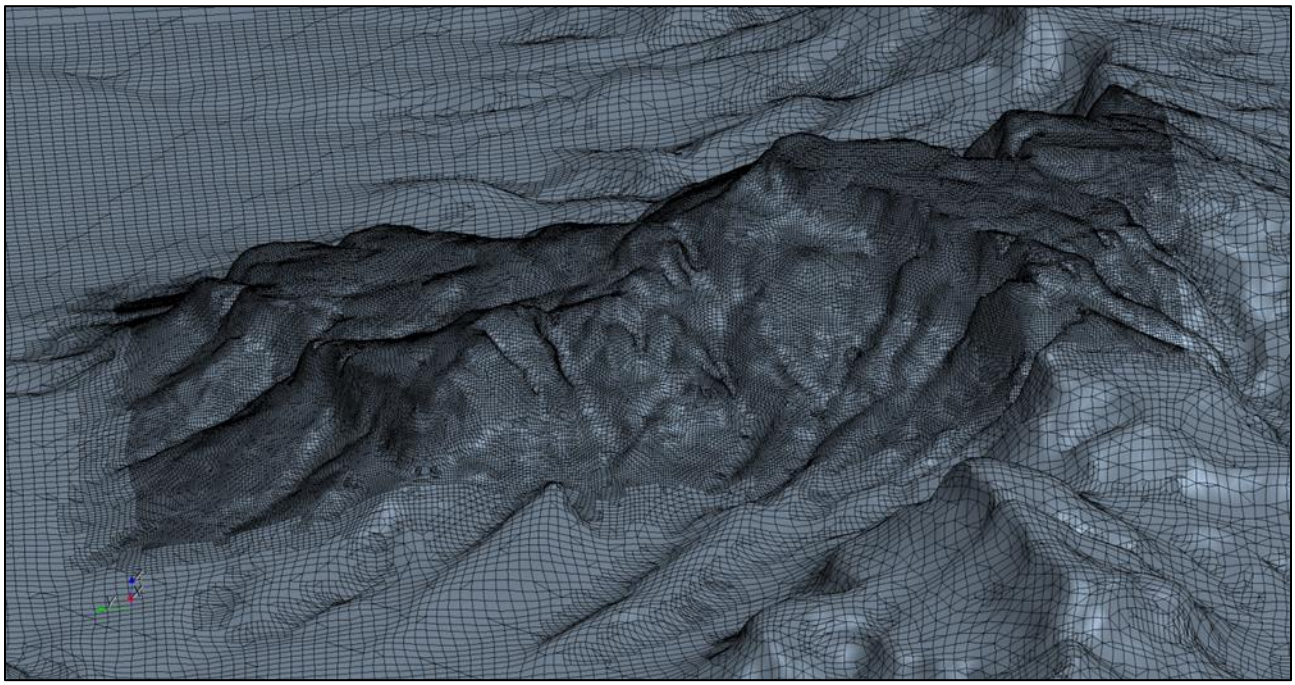

Figure 3-6
A side view of the western slope of the Mariepskop block mesh.

3.4 Boundary types

The Mariepskop terrain was set to a “Wall” type boundary between the mountain and the atmosphere in contact with the mountain, which represents an impermeable, non-slip surface (see STAR-CCM+ user guide, 2011), whereas the lateral boundaries on the north, south, east and west were chosen to be velocity inlet boundaries (where air is pushed into the domain across the upwind boundaries and pulled out of the domain across the downwind boundaries. The top boundary in the upper atmosphere at a height of 8000 m above the lowest point in the terrain was set to a symmetry plane.

3.5 The model conditions

3.5.1 Time steps

The time step simulation method that was selected for this study is referred to as “implicit unsteady”. The reason is because the CFD model failed to converge under steady conditions when a very large domain, such as in this study, is considered. The author had come to this conclusion after a number of test simulations. Since there are regions within the domain where separated flow occurs which is characterized by highly unsteady turbulent flow, a transient solution was necessary to achieve convergence. It was therefore not possible to simulate this highly random turbulent flow by means of a steady simulation. Due to the flow being transient (unsteady) phenomena in nature a steady state simulation will still vary per iteration and will not reach a normalized single value.

At first the simulation time step was set to 0.001 s until the model had stabilized. The simulation time step was then increased to 0.1 s, followed by 1.2 s and eventually 2.4 s, in order to increase running speed which was still very time consuming, but manageable.

The solution was initialized using zero as the initialization value to the numerical solver. The solution within the domain and was allowed to numerically converge from there. The time it takes to converge could be reduced if initialization values closer to the mean flow in the domain are used, but the final solution will not be different.

3.5.2 Flow and energy

3.5.2.1 The viscous regime

Viscous flow can be divided into two categories, namely either laminar or turbulent. Laminar and turbulent flows are natural flow phenomena and are both described by the Navier-Stokes equations. The Navier-Stokes equations are used to describe the effects of viscosity; thermal conductivity and mass diffusion in fluids (see STAR-CCM+ user guide, 2011).

In this study a turbulent viscous regime was chosen, as one of the main aims of running the CFD model was to simulate turbulent flow over Mariepskop in order to reproduce circulation patterns that modulate various climatic zones over the mountain. As a matter of fact, laminar flow is unsuitable for mountain flow studies.

The model's turbulent flow is in a state of continuous instability, exhibiting irregular, small-scale, high-frequency fluctuations in both space and time (see STAR-CCM+ user guide, 2011). White, (2006) gives a good description of turbulence by calling it "a spatially varying mean flow with superimposed three dimensional random fluctuations that are self-sustaining and enhance mixing, diffusion, entrainment and dissipation". Although, strictly speaking, it is possible to simulate turbulent flow directly by direct numerical simulation, the computer resources required are too large to simulate in practice. It is therefore necessary to select the most suitable turbulence model (see STAR-CCM+ user guide, 2011). The turbulence model selected for this study will be discussed in more detail in section 3.5.4.

3.5.2.2 The Coriolis Effect

As the length scale of Mariepskop is less than 10 km, the Coriolis forces of the Earth could be ignored for the purpose of this study (Kaimal and Finnigan, 1994, Stangroom, 2004). As a matter of fact, the scale of turbulent flow or circulation takes place according to the complex topography of the mountain over spatial scales of far less than 10 km, which even more justifies the assumption that the influence of the Coriolis force could be are neglected.

3.5.2.3 The equation of state mode

According to the STAR-CCM+ user guide (2011) the Equation of State model is used to compute the density and the density derivatives with respect to temperature and pressure. For this simulation the ideal gas model was chosen as the Equation of State model.

The Ideal Gas model uses the ideal gas law to express density as a function of temperature and pressure (STAR-CCM+ user guide, 2011).

$$\boldsymbol{\rho = P_{ab}/R_a T} \tag{3.1}$$

Where ρ is density, P_{ab} is absolute pressure, T is temperature, and the gas constant R_a for air is given by R_a=R/M where R is the universal gas constant and M is the molecular mass of air. For the purpose of this study it was assumed that air is an incompressible gas.

3.5.2.4 The segregated flow model

The segregated flow model was selected to simulate flow and energy. This model is best situated for incompressible or mildly compressible flows, particularly when computational resources are limited and in the case of flow with low Mach and Raleigh numbers (see STAR-CCM+ user guide, 2011). As relatively low speed flow occurs in this study, the application of the segregated flow model is regarded as ideal.

According to the STAR-CCM+ user guide (2011), the segregated flow model solves the flow equations (one for each component of velocity, and one for pressure) in a segregated, or uncoupled, way. A predictor-corrector approach maintains the linkage between the momentum and continuity equations. The convection scheme chosen for this simulation is the second order upwind finite volume discretization scheme. The advantage of this scheme is that its accuracy is better than the first order upwind convection scheme.

The STAR-CCM+ model makes use of the Navier-Stokes governing equations. The equations can be represented by the following integral equations for continuity (Equation 3-2) and momentum (Equation 3-3), (STAR-CCM+ user guide, 2011).

$$\frac{d}{dt}\int_V \boldsymbol{\rho\chi dV} + \oint_A \boldsymbol{\rho(v - v_g).da} = \int_V \boldsymbol{S_u dV} \tag{3-2}$$

$$\frac{d}{dt}\int_V \boldsymbol{\rho\chi v dV} + \oint_A \boldsymbol{\rho v \times (v - v_g).da} = -\oint_A \boldsymbol{\rho I.dA} + \oint_A \boldsymbol{T.dA} + \int_V \boldsymbol{(f_r + f_g + f_p + f_u)dV} \tag{3-3}$$

In the equations above, χ denotes porosity (which is not used in the Mariepskop simulation), V is the cell volume, v the velocity vector, v_g the grid velocity vector, and a is the face area vector. I is the identity matrix and A the inviscid flux Jacobian (in the case of this simulation the flow is viscous and therefore no inviscid flow is present).

The terms on the left hand side of Equation 3-3 are the transient and convective flux terms. On the right hand side the pressure gradient term, the viscous flux and the body force terms can be found. The viscous stress tensor is indicated by T. The value of T will depend on whether the viscous flux represents laminar or turbulent flow. In this study the flow is turbulent. The body force terms (f_r, f_g,f_p *and* f_u) represent the effects of system rotation, buoyancy, porous media and user defined body forces - in that order. In the case of the Mariepskop simulations only the buoyancy body force term was utilised which is responsible for the effect of gravity in the simulation.

Thus, in the case of the Mariepskop simulation, the Navier Stokes continuity equation (Equation 3-2) becomes Equation 3-4 when all the assumptions made in this study are taken into account.

$$\oint_A \boldsymbol{\rho}(\boldsymbol{v}-\boldsymbol{v_g}).\boldsymbol{da} = \int_V \boldsymbol{S_u}\boldsymbol{dV} \tag{3-4}$$

The same applies to the Navier Stokes momentum equation, which becomes Equation 3-5:

$$\oint_A \boldsymbol{\rho v}\times(\boldsymbol{v}-\boldsymbol{v_g}).\boldsymbol{da} = -\oint_A \boldsymbol{\rho I}.\boldsymbol{dA} + \oint_A \boldsymbol{T}.\boldsymbol{dA} + \int_V (\boldsymbol{f_g})\boldsymbol{dV} \tag{3-5}$$

3.5.2.5 Turbulent viscous fluxes

In the case of laminar flow in STAR-CCM+, the stress tensor T is defined as in Equation 3-6 (see STAR-CCM+ user guide, 2011):

$$\boldsymbol{T} = \boldsymbol{T_l} = \boldsymbol{\mu}\left[\boldsymbol{\nabla v} + \boldsymbol{\nabla v^T} - \frac{\mathbf{2}}{\mathbf{3}}(\boldsymbol{\nabla}.\boldsymbol{v})\boldsymbol{I}\right] \tag{3-6}$$

For turbulent flow, the complete stress tensor is given by Equation 3-7 (STAR-CCM+ user guide, 2011):

$$\boldsymbol{T} = \boldsymbol{T_l} + \boldsymbol{T_t} \tag{3-7}$$

In Equations 3-6 and 3-7, T_t is the turbulent stress tensor and is also known as the Reynolds stress tensor whereas T_l is the laminar stress tensor. When the Boussinesq approximation is

invoked, the equation for the stress tensor becomes Equation 3-8 (see STAR-CCM+ user guide, 2011):

$$\boldsymbol{T} = \boldsymbol{\mu_{eff}}\left[\boldsymbol{\nabla v} + \boldsymbol{\nabla v^T} - \frac{\mathbf{2}}{\mathbf{3}}(\boldsymbol{\nabla}.\boldsymbol{v})\boldsymbol{I}\right] \quad (3\text{-}8)$$

Where the effective viscosity, $\mu_{eff,}$ is the sum of the laminar and turbulent viscosities ($\mu_{eff} = \mu_l + \mu_{t.}$).

3.5.2.6 Fluid energy through a segregated approach

The Segregated Fluid Energy model that was selected for the Mariepskop simulation is known as the Segregated Fluid Temperature model. This model acts as a companion model to the Segregated Flow model discussed earlier.

This model solves the total energy equation with temperature as the independent variable, whereas enthalpy is then computed from temperature according to the equation of state (see STAR-CCM+ user guide, 2011). It is recommended for cases where no combustion takes place, and as the Mariepskop simulation does not include combustion of any form, this model is appropriate for use. As in the case of the Segregated Flow model, a second order upwind convection finite volume discretization scheme was applied.

The energy equation (written in integral form) is shown in Equation 3-9 (see STAR-CCM+ user guide, 2011):

$$\frac{\boldsymbol{d}}{\boldsymbol{dt}}\int \boldsymbol{\rho E dV} + \oint [\boldsymbol{\rho H}(\boldsymbol{v} - \boldsymbol{v_g}) + \boldsymbol{v_g\rho}].\boldsymbol{da} = -\oint_{\boldsymbol{A}} \boldsymbol{q''}.\boldsymbol{da} + \oint_{\boldsymbol{A}} \boldsymbol{T}.\boldsymbol{v da} + \int_{\boldsymbol{V}} \boldsymbol{f}.\boldsymbol{v dV} + \int_{\boldsymbol{V}} \boldsymbol{s_u dV} \quad (3\text{-}9)$$

Where E denotes the total energy, H the total enthalpy, and $q"$ is the heat flux vector. The body force vector f is the body force vector representing the combined body forces, of which only the buoyancy force is included in this study. In the last term of the equation S_u contributes additional energy source terms that are user specified. No such source terms were included in this study. Therefore, for the purpose of this study, the energy equation becomes Equation 3-10:

$$\int \boldsymbol{\rho E dV} + \oint [\boldsymbol{\rho H}(\boldsymbol{v} - \boldsymbol{v_g}) + \boldsymbol{v_g\rho}].\boldsymbol{da} = -\oint_{\boldsymbol{A}} \boldsymbol{q''}.\boldsymbol{da} + \oint_{\boldsymbol{A}} \boldsymbol{T}.\boldsymbol{v da} + \int_{\boldsymbol{V}} \boldsymbol{f_g}.\boldsymbol{v dV} \quad (3\text{-}10)$$

3.5.2.7 Modeling gravity

The gravity model in STAR-CCM+ is responsible for inducing the action of gravitational acceleration on the fluid that is simulated and it provides the following two possibilities (see STAR-CCM+ user guide, 2011):

- The working pressure becomes the piezometric pressure;
- The body force due to gravitational acceleration can be included in the momentum equations.

In STAR-CCM+ the working pressure is the solution variable used in the flow models. Its definition is a matter of computational convenience and it is always expressed relative to the Reference Pressure (a device that reduces the numerical round off error in the numerical calculations involving pressure).

When the gravity model is activated, the working pressure becomes equal to the piezometric pressure which is defined by Equation 3-11 (see STAR-CCM+ user guide, 2011):

$$\boldsymbol{p_{piezo} = p_{static} - \rho g(x - x_0)} \quad (3\text{-}11)$$

Where p_{piezo} is the piezometric pressure, p_{static} the static pressure, g the gravitational acceleration, x the altitude, and x_0 the reference altitude which is chosen by the user. The static pressure is the spherical part of the stress tensor acting in fluids and has the same value as the actual thermodynamic pressure of the fluid. The reference altitude is the altitude at which the piezometric pressure and static pressure is equal (see STAR-CCM+ user guide, 2011).

3.5.2.8 Modeling turbulence

A turbulence model is needed in STAR-CCM+ for providing closure to the governing equations in turbulent flows. The Reynolds-Averaged Navier Stokes (RANS) k-ε turbulence model was selected for this study. The k-ε turbulence models are known for providing a good compromise between robustness, computational cost and accuracy, and are in general well suited to industrial-type applications that contain complex recirculation, with or without heat transfer (see STAR-CCM+ user guide, 2011).

The RANS equations a statistical method, first proposed by Reynolds (1895), is obtained by decomposing the Navier-Stokes equations for the instantaneous velocity and pressure fields

into a mean value and a fluctuating component. The averaging process may be thought of as ensemble averaging for repeatable transient situations. The resulting equations for the mean quantities are basically identical to the original equations, except for the appearance of an additional term in the momentum transport equation. This additional term is a tensor quantity, known as the Reynolds stress tensor T_t which is defined as follows (STAR-CCM+ user guide, 2011):

$$\boldsymbol{T_t} \equiv -\boldsymbol{\rho}\overline{\boldsymbol{v'v'}} = -\boldsymbol{\rho}\begin{bmatrix}\overline{\boldsymbol{u'u'}} & \overline{\boldsymbol{u'v'}} & \overline{\boldsymbol{u'w}} \\ \overline{\boldsymbol{u'v'}} & \overline{\boldsymbol{v'v'}} & \overline{\boldsymbol{v'w'}} \\ \overline{\boldsymbol{u'w'}} & \overline{\boldsymbol{v'w'}} & \overline{\boldsymbol{w'w}}\end{bmatrix} \tag{3-12}$$

Closure is thus provided to the governing equations by modelling the Reynolds stress tensor from Equation 3-12. The approach that is used by the k-ε turbulence model is an eddy viscosity modelling approach. The most common eddy viscosity model is the model that makes use of the approximated Boussinesq equation. This equation uses the turbulent viscosity μ_t to model the Reynolds stress tensor as a function of mean flow quantities. The approximated Boussinesq equation is defined by Equation 3-13 (see STAR-CCM+ user guide, 2011):

$$\boldsymbol{T_t} = \boldsymbol{2\mu_t S} - \frac{\boldsymbol{2}}{\boldsymbol{3}}(\boldsymbol{\mu_t \nabla . v} + \boldsymbol{\rho k})\boldsymbol{I} \tag{3-13}$$

In Equation 3-13 S is the strain tensor, which can be defined as follows:

$$\boldsymbol{S} = \frac{\boldsymbol{1}}{\boldsymbol{2}}(\boldsymbol{\nabla v} + \boldsymbol{\nabla v^T}) \tag{3-14}$$

and k is the turbulent kinetic energy.

Various k-ε turbulence models exist. These models are generally two-equation models where the transport equations are solved for the turbulent kinetic energy k and its dissipation rate ε (see STAR-CCM+ user guide, 2011).

The k-ε turbulence model used in this study is the realizable two-layer k-ε model. The realizable model was developed by Shih *et al.,* (1994) and is considered as one of the most recent successful additions to the STAR-CCM+ model (see STAR-CCM+ user guide, 2011). According to Stangroom (2004) this model has performed reasonably well for flow over hills and cliffs. It is considered to be substantially more accurate than the standard k-ε model for many applications, and can generally be regarded as at least as accurate. A full discussion on the formulation of

the realizable model formulation can be found in the publication by Shih *et al.,* (1994) and in the STAR-CCM+ user guide.

The Realizable Two-Layer k-ε model combines the Realizable k-ε model discussed in the paragraph above with a two-layer approach. The coefficients in the realizable and realizable two layer models are the same, but the two layer model has the added advantage of an all $y+$ wall treatment (STAR-CCM+ user guide, 2011). According to Salim and Cheah, (2009) the wall $y+$ value is a non-dimensional distance similar to the local Reynolds number, often used in CFD simulations to describe the quality of a mesh for a particular flow simulation. It can be summed up as the ratio between the turbulent and laminar influences in a cell (Salim and Cheah, 2009). The all $y+$ wall treatment works well for either very coarse, very fine or intermediate meshes and is therefore very versatile. It is also the recommended turbulence model for the STAR-CCM+ model (see STAR-CCM+ user guide, 2011).

The two-layer approach was first developed by Rodi, (1991) and in this approach, the computation is divided into two layers, namely the layer adjacent to the wall, and the layer further removed from the wall. The values of the turbulent dissipation rate, ε and the turbulent viscosity μ_t are specified as functions of wall distance whereas the values of ε specified in the near-wall layer are blended smoothly with the values computed from solving the transport equation further from the wall (STAR-CCM+ user guide, 2011).

The two-layer approach will not be discussed here in further detail and the reader is referred to the STAR-CCM+ user guide and the text by Jongen (1998) for further information on the subject.

Although k-ε turbulence models are generally not considered to be as accurate for the modelling of flow over complex terrain as the Large Eddy Simulation (LES) models, they have been used relatively successfully in a number of studies concerning flow over terrain including the studies by Stander, (2008) and Stangroom, (2004). The most significant advantage of RANS turbulence models (such as the k-$\boldsymbol{\varepsilon}$ model) over LES models is that it is much cheaper in both computer time and memory. In the early stages of this study the hope was to refine the Mariepskop mesh to such an extent that a LES model could be considered. However, this plan did not succeed as the Random Access Memory (RAM) limit of the computer was reached before the mesh was fine enough to run a LES simulation (a supercomputer with a RAM of 16 Gigabytes was used for this study).

3.6 Model scenarios

To accommodate the averaged NCEP-NCAR reanalysis data values for the DJF and JJA seasons as well as vertically interpolated values between the two pressure levels (850 hPa and 700 hPa) for each season (as obtained from the data presented in Chapter 2), the Mariepskop STAR-CCM+ simulations were performed three times:

- **First simulation (*700 hPa DJF simulation*):** Averaged wind speed and direction values collected and calculated over the period 1981 to 2011 at the 700 hPa level for the summer (DJF) season were used as higher level laminar lateral boundary input to the model domain. Averaged wind speed and direction values at the 850 hPa level were calculated by only considering those days where the average conditions prevailed at the 700 hPa level, and these values were then used for lower level laminar lateral boundary input. Wind values between the 850 hPa and 700 hPa levels were subsequently linearly interpolated to obtain boundary values for the model's vertical level input.

- **No simulation (*850 hPa DJF simulation*):** the 850 hPa and associated 700 hPa wind speed and wind direction values were very similar to *700 hPa DJF simulation* values (above) and therefore results from the *700 hPa DJF simulation* were considered to be also representative for this simulation – no additional simulation was necessary.

- **Second simulation (*700 hPa JJA simulation*):** Similar to the *700 hPa DJF simulation*, but this time for the JJA season.

- **Third simulation (*850 hPa JJA simulation*):** Because JJA 850 hPa and 700 hPa wind speed and direction averaged values differed substantially, the same was done as in the *700 hPa DJF simulation*, but this time for the JJA season and as the 850 hPa level as basis, where the averaged wind speed and the direction values at the 700 hPa level were calculated only for the days where the average conditions prevailed at the 850 hPa level – in contrast to the first simulation.

3.7 Boundary conditions

The boundary conditions for temperature, pressure and wind velocity were supplied to the model in the form of field functions. The name “Field Functions” are used for functions that supply the CFD model with boundary conditions that change as a function of some variable (or variables). In the case of this study the field functions describe temperature, pressure and wind velocity as a function of height AMSL. Field functions were created from the long-term averaged (1981 to 2011) wind speed, wind direction and surface temperature values obtained from the NCAR/NCEP reanalysis data discussed in Chapter 2.

3.7.1 Temperature

The field function used as the temperature boundary condition was expressed as a linear equation (Equation 3-18) that starts at the average seasonal near-surface temperature at Mariepskop, at the model surface, and then declined with increments of 6.5 °C for every altitudinal increase of 1000 m (1km). This is the same average environmental temperature lapse rate as is specified by the ISA (International Organization for Standardisation, 1975).

This field function is supplied by Equation 3-18:

$$\boldsymbol{T_z = T_{ground} - \frac{6.5}{1000} \times z} \qquad (3\text{-}18)$$

where T_z denotes the temperature at a given height above the surface, T_{ground} the surface temperature and z the height above model land surface level. Figure 3-7 illustrates the decrease in temperature with altitude as provided by equation 3-18 for a surface temperature of 23.5 ºC (the average summer surface temperature at Mariepskop as discussed in Chapter 2).

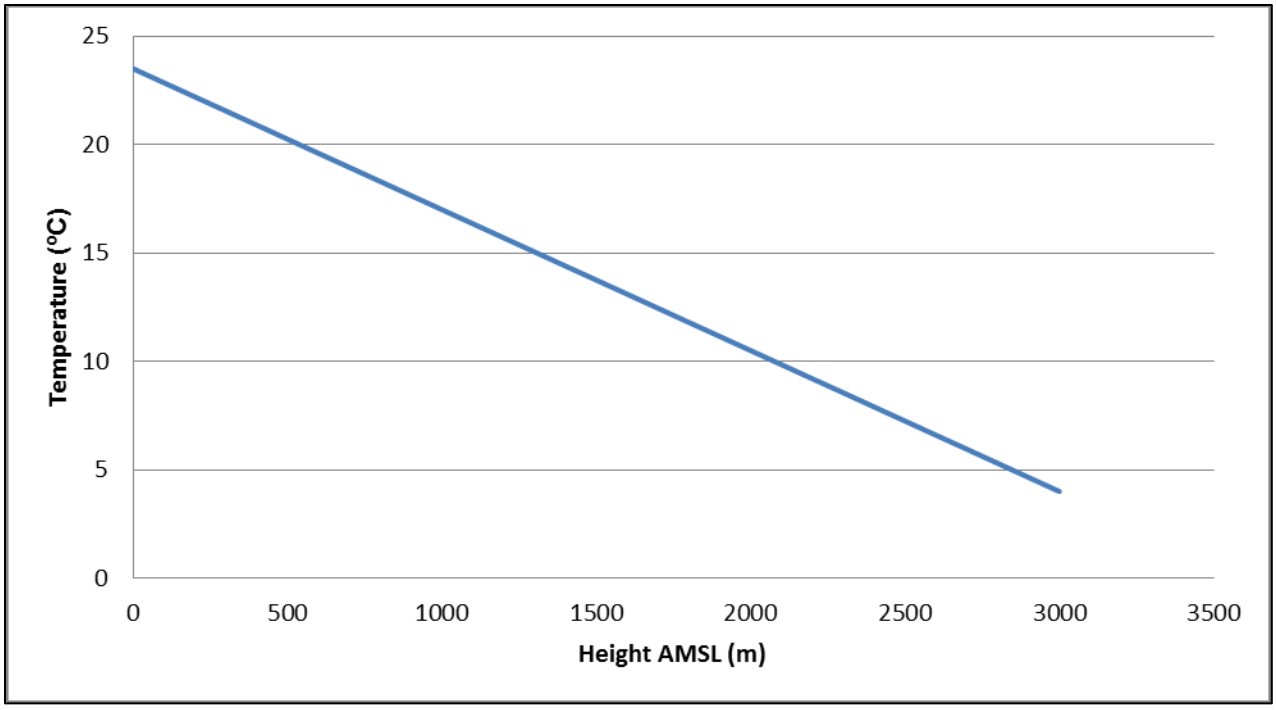

Figure 3-7:
Atmospheric temperature decline (ºC) with an increase in altitude (m) Above Mean Sea Level (AMSL) for a surface temperature scenario of 23.5 ºC.

3.7.2 Pressure

The pressure decrease, as a function of height, was calculated by making use of the barometric equation (Equation 3-19), where the assumption of a linear decrease of pressure with height is made. The barometric equation is believed to be a good approximation for the pressure distribution with height of the troposphere (Berberan-Santos *et al.*, 1997; Iribarne and Godson, 1981; Dutton, 1986). The barometric equation may be defined as follows:

$$\boldsymbol{P(z) = P(0)(1 - \frac{Lz}{T_0})^{\frac{Mg}{RL}}} \qquad (3\text{-}19)$$

Where $P(z)$ is the atmospheric pressure at a certain altitude z, $P(0)$ is the atmospheric pressure at a reference altitude (in this case an altitude of 500 m at the bottom of Mariepskop), L is the temperature lapse rate (0.0065 K.m^{-1} as defined in the ISA), T_0 is the temperature at the reference altitude (in this case it is the average summer and winter temperatures of 23.5 ºC and 17.2 ºC that were obtained in Chapter 2), M is the molar mass of dry air (0.029 kg.mol^{-1}), g is the gravitational acceleration (9.8 m.s^{-2}) and R (8.3 J.(mol.K)$^{-1}$) is the universal gas constant.

The barometric formula for the summer conditions over Mariepskop therefore becomes:

$$\boldsymbol{P(z) = 96000(1 - (2.19 \times 10^{-5})z)^{5.25}} \quad \text{(3-20)}$$

Figure 3-8 shows the decline in pressure (according to Equation3-20) with altitude during summer over Mariepskop.

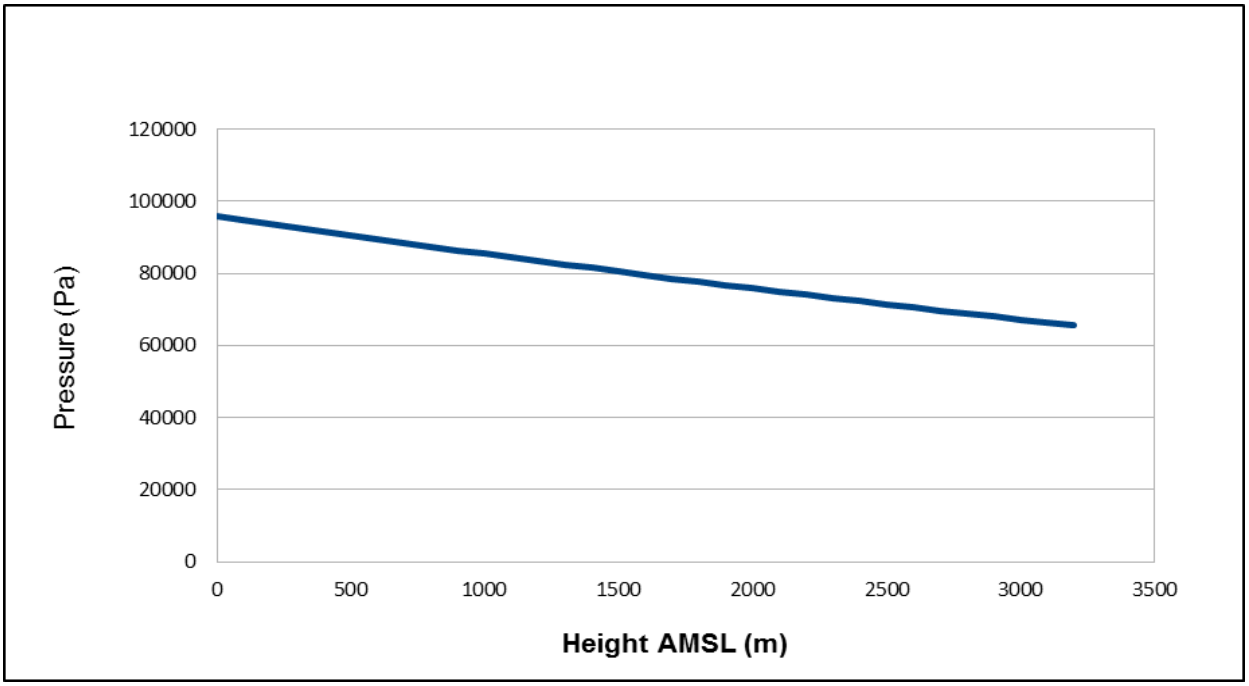

Figure 3-8:
Atmospheric pressure decline (Pa) with an increase in altitude (m) Above Mean Sea Level (AMSL) during the summer season.

For the winter season the barometric formula becomes:

$$\boldsymbol{P(z) = 96000(1-(2.22 \times 10^{-5})z)^{5.25}} \quad \text{(3-21)}$$

Figure 3-9 depicts the atmospheric pressure (according to equation 3-21) with an increase in altitude during winter time.

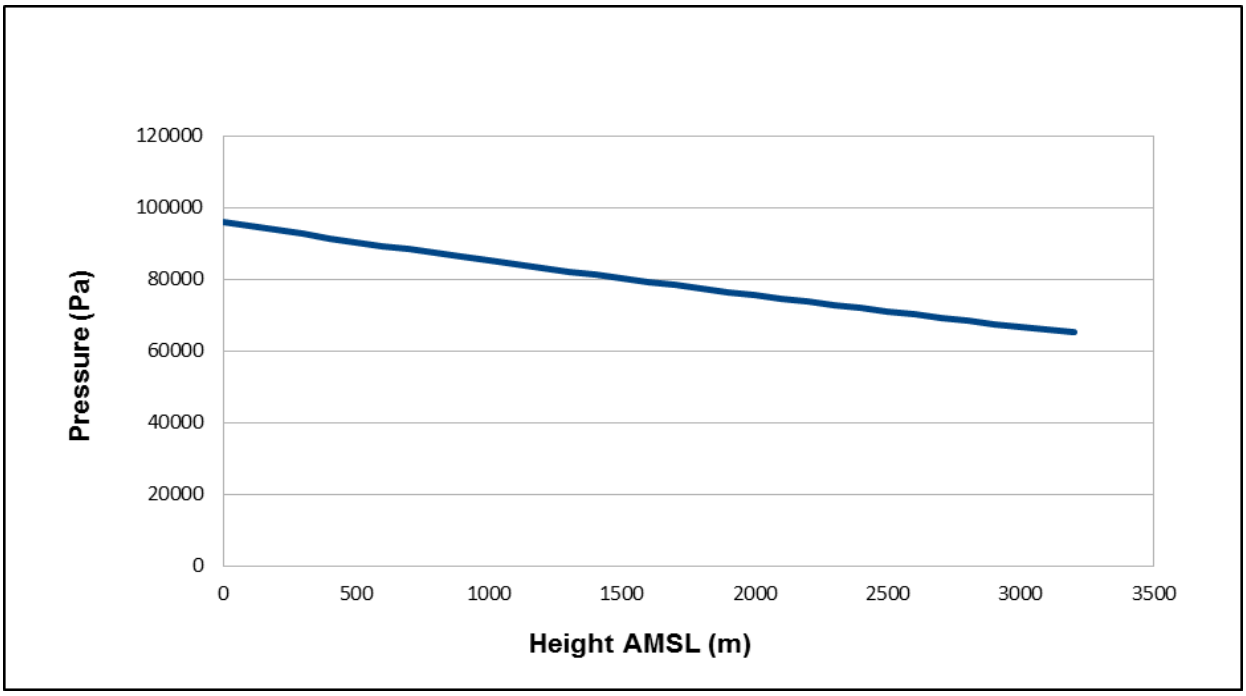

Figure 3-9:
Atmospheric pressure decline (Pa) with an increase in altitude (m) Above Mean Sea Level (AMSL) during the winter season.

3.7.3 Wind speed and direction

The power law velocity equation (Equation 3-22) was used to create an estimated field function of the wind speed profile from the surface of Mariepskop to a height of approximately 1500 m AMSL (or the 850 hPa pressure level). Above 1500 m AMSL a linear interpolation was employed for seasonal (DJF and JJA) averaged wind speeds from the 850 hPa to 700 hPa pressure levels. Above approximately 2500 m AMSL (or the 700 hPa pressure level), the wind speed was kept constant. This is discussed in more detail in sections 3.7.3.1, 3.7.3.2 and 3.7.3.3 for each of the simulation scenarios where graphs of wind speed as a function of height AMSL are shown.

The method depicted by the power-law velocity equation is the most commonly used wind speed extrapolation method in boundary layer studies. It is preferred by engineers for its mathematical simplicity, and it provides a reasonable fit to observed wind velocity profiles within the lower part of the planetary boundary layer. The power-law velocity equation can be expressed as follows (Zoumakis, 1992):

$$\frac{u(z)}{u_1} = \frac{z}{z_1}^{p}, \text{ p>0} \qquad (3\text{-}22)$$

In Equation 3-22, $u(z)$ and u_1 are the wind speeds at heights z and z_1, respectively, where the height z_1 is a "surface" reference height. The exponent p is called the wind speed exponent and is a function of surface geometry and atmospheric stability (Zoumakis, 1992; Tiwary and Colls, 2010). Table 3-1, as adapted from Tiwary and Colls (2010), gives the values of the exponent p compared to pasquill stability classes.

Table 3-1:
Variation of the wind speed exponent p with atmospheric stability (adapted from Tiwary and Colls, 2010).

Pasquill stability class	Description	Exponent for rough terrain	Exponent p for smooth terrain
A	Very unstable	0.15	0.07
B	Moderately unstable	0.15	0.07
C	Slightly unstable	0.2	0.1
D	Neutral	0.25	0.15
E	Stable	0.4	0.35
F	Very stable	0.6	0.55

Although it has been stated that the logarithmic profile law has a sounder theoretical and physical basis than the power-law profile (Arya, 1988), the logarithmic profile makes use of surface roughness and stability values which were unknown in this study.

As in the case of wind speed, wind directions were known at two pressure levels, namely 850 hPa and 700 hPa (which correspond roughly to an altitude of approximately 1500 m and 2500 m AMSL). Wind directions from the surface of the terrain to a level of 1500 m AMSL were kept constant (as the value of the dominant wind direction at 1500 m AMSL as obtained from the data presented in Chapter 2) whereas the wind directions were allowed to change linearly between the known dominant directions at the 1500 m and 2500 m AMSL levels. From the 2500 m AMSL level upwards the wind direction was again kept at a constant value (the dominant wind direction at the 2500 m level as obtained from the data presented in Chapter 2). The change in

wind direction for each of the simulation scenarios are discussed in further detail in sections 3.5.5.3.1, 3.5.5.3.2 and 3.5.5.3.3.

3.7.3.1 700 hPa DJF simulation

If it is assumed that the height AMSL at the 850 hPa and 700 hPa atmospheric levels are 1500 m and 2500 m, Table 3-2 lists the change of wind speed with height AMSL for the *700 hPa DJF simulation*.

Table 3-2:
The functions governing wind speed with an increase in height Above Mean Sea Level (AMSL) for the *700 hPa DJF simulation*.

Wind speed functions for the *700 hPa DJF simulation* (m/s)		
Below 1500 m	Between 1500 m and 2500 m	Above 2500 m
$u(z) = 0.251z^{0.4}$	$u(z)=0.0016z+2.25$	$u(z)=6.3$

Where $u(z)$ is the wind speed in $m.s^{-1}$ at a height z AMSL.

Figure 3-10 shows the wind speed distribution against height AMSL graphically, as obtained from the equations in Table 3-2:

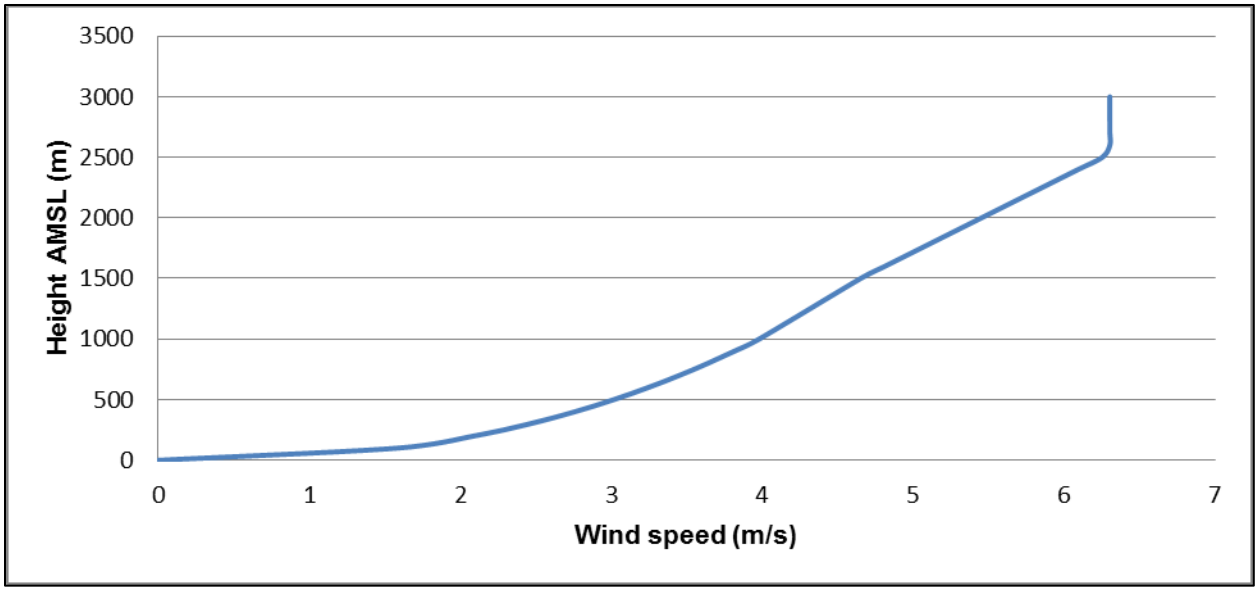

Figure 3-10:
The wind speed distribution with height Above Mean Sea Level (AMSL) for the *700 hPa DJF simulation*.

The functions governing wind direction with an increase in altitude for the *700 hPa DJF simulation* are shown in Table 3-3.

Table 3-3:
The functions governing wind direction with an increase in height Above Mean Sea level (AMSL) for the *700 hPa DJF simulation*.

Wind direction functions for the *700 hPa DJF simulation* (rad)		
Below 1500 m	Between 1500 m and 2500 m	Above 2500 m
D=-3.32	D = 0.00059z-2.43	D= -3.91

3.7.3.2 700 hPa JJA simulation

The equations used to determine the wind speed distribution with height AMSL for the *700 hPa JJA simulation* are given in Table 3-4.

Table 3-4:
The functions governing wind speed with an increase in height Above Mean Sea Level (AMSL) for the *700 hPa JJA simulation*.

Wind speed functions for the *700 hPa JJA simulation* (m/s)		
Below 1500 m	Between 1500 m and 2500 m	Above 2500 m
$u(z) = 0.2z^{0.32}$	u(z)=0.004z-3.84	u(z)=6.09

A graph representing the equations in Table 3-4 can be seen in Figure 3-11.

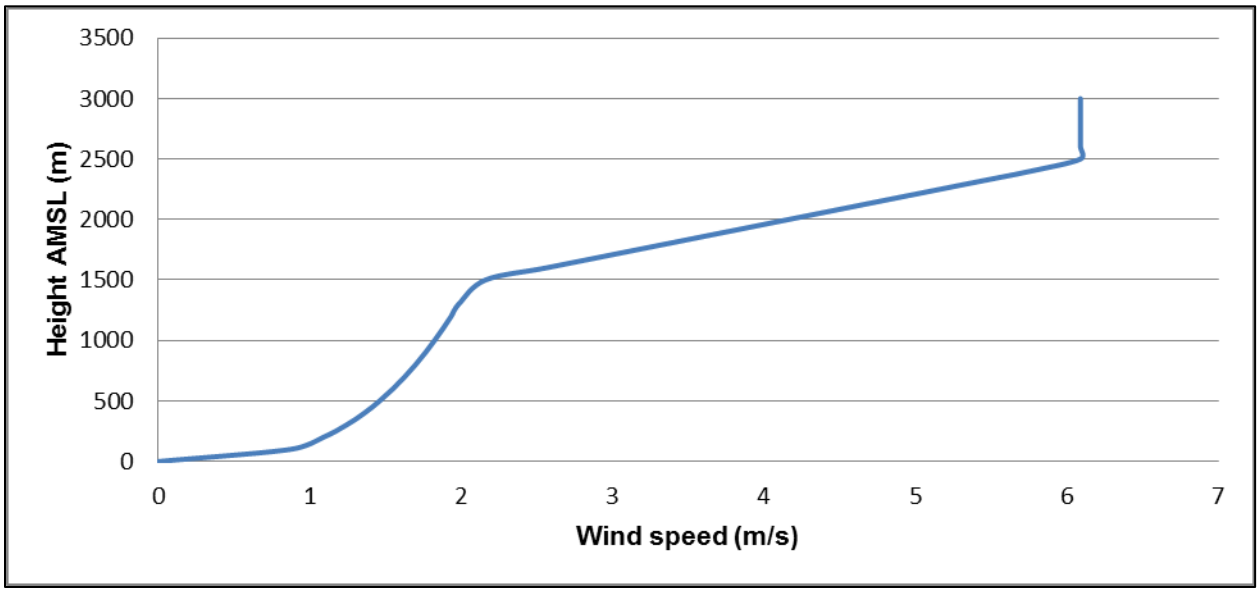

Figure 3-11:
The wind speed distribution against height Above Mean Sea Level (AMSL) for the *700 hPa JJA simulation*.

The functions governing wind direction with an increase in height AMSL for the *700 hPa JJA simulation* are shown in Table 3-5.

Table 3-5:
The functions governing wind direction with an increase in height Above Mean Sea Level (AMSL) for the *700 hPa JJA simulation*.

Wind direction functions for the *700 hPa JJA simulation* (rad)		
Below 1500 m	Between 1500 m and 2500 m	Above 2500 m

Wind direction functions for the *700 hPa JJA simulation* (rad)		
D=-1.94	D=0.0023z-5.42	D=0.387

3.7.3.3 850 hPa JJA simulation

Table 3-6 lists the change of wind speed with height AMSL for the *850 hPa JJA simulation*.

Table 3-6:
The functions governing wind speed with an increase in height Above Mean Sea Level (AMSL) for the *850 hPa JJA simulation*.

Wind speed functions for the *850 hPa JJA simulation* (m/s)		
Below 1500 m	Between 1500 m and 2500 m	Above 2500 m
$u(z) = 0.158z^{0.2}$	u(z)=0.0016z-1.734	u(z)=2.26

A graphical representation of the equations in Table 3-6 can be seen in Figure 3-12.

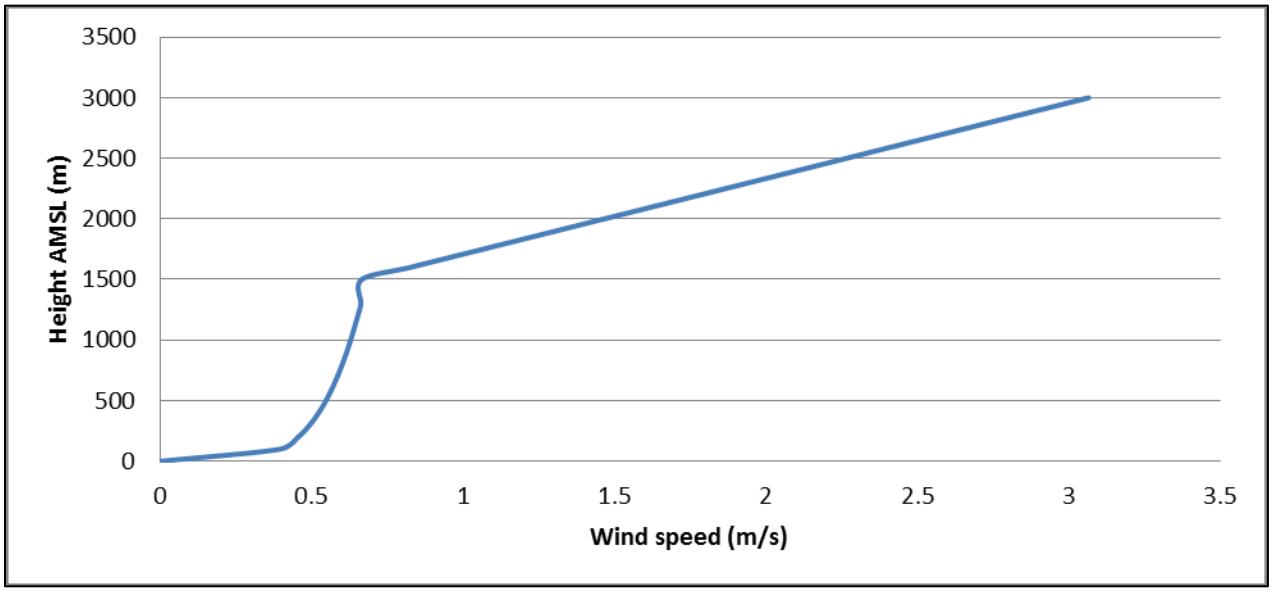

Figure 3-12:
The wind speed distribution against height Above Mean Sea Level (AMSL) for the *850 hPa JJA simulation.*

The equations describing the change in wind direction with an increase in height AMSL are listed in Table 3-7.

Table 3-7:
The functions governing wind direction with an increase in height Above Mean Sea Level (AMSL) for the *850 hPa JJA simulation*.

Wind direction functions for the *850 hPa JJA simulation* (rad)		
Below 1500 m	Between 1500 m and 2500 m	Above 2500 m
D=--3.52	D=0.00295z-7.95	D=-0.576

3.8 Further assumptions

Due to limited information and computer resources, surface roughness and solar radiation (although it can be sufficiently modeled by the STAR-CCM+ model) were not included in this study.

3.9 Verification of the model output

In order to validate the output of the CFD model, three wind speed monitors were set up in the model domain approximately at the geometrical positions were the 1300 m, 1600 m, and 1900 m weather stations are located on Mariepskop. The wind speed measurements made by the monitors were then compared to the wind speed measurements made by the weather stations on Mariepskop in order to delineate whether any correlations exist between the model output and the weather station measurements. The verification of the model output is discussed in more detail in Chapter 4.

3.10 Other options explored

An attempt was made to do a high resolution run over the Mariepskop domain by making use of the Weather Research and Forecasting (WRF) atmospheric model. The reasoning behind this was that the atmospheric model will be able to give us detailed information about the atmospheric flow over Mariepskop as well as information about moisture, cloud formation and rainfall. This option has proven to be very computationally expensive as the WRF model is not as well suited for very high resolution runs as the CFD model. Another problem was that the

WRF model makes use of a sigma terrain following coordinate. This terrain following coordinate would have a smoothing effect on the Mariepskop topography which means that many of the steep slopes on Mariepskop (of which there are many) would be lost. Therefore it was concluded that the WRF model is not ideally suited for the purpose of this study as valuable information about flow in a complex terrain such as Mariepskop will be lost and the model is computationally and time expensive. However, information about moisture circulation and rainfall patterns will be priceless for the continuation of the Mariepskop multidisciplinary project. Therefore it is recommended that a simulation on an atmospheric model such as WRF be done in the future, as including moisture effects in a CFD model such as STAR-CCM+ is difficult to do compared with and atmospheric model. It is also a possibility to couple the WRF atmospheric model with a CFD model such as STAR-CCM+ by down scaling the WRF model as far as possible and then feeding the atmospheric boundary conditions from WRF into a CFD model (instead of using simple averaged boundary conditions as in the case of this study) from where the CFD model can be run at high resolution. This will be a best case scenario as both models' advantages will be put to use.

4

Verification Results

4.1 Introduction

This chapter deals with the STAR-CCM+ model results and the verification thereof. Model simulated wind speed and wind direction results were compared to observed results logged by the three weather stations on Mariepskop (Figure 4-24). The model was further used to create streamlines of flow over Mariepskop. These streamlines were used to identify areas where air rises over the mountain, as these areas will have the highest probability of cloud formation and rainfall. These identified potential rainfall areas were then compared to aerial photographs of Mariepskop in order to establish whether the streamlines are a reflection of reality.

4.2 Volume mesh sensitivity study

In order to decide on the most adequate volume mesh size for the final simulation, it was important to first perform a volume mesh sensitivity study. The ideal would be to a reach a point where the amount of cells selected for the volume mesh no longer influences the simulation results. The accuracy of a mesh is not only dependant on the number of cells, but more importantly their location. The areas where complex flow occurs should have a larger number of cells per unit area, compared to regions where simpler flow phenomena occur (Stangroom, 2004). Such a volume mesh sensitivity study was done by considering the first simulation over Mariepskop, namely the *700 hPa DJF simulation*. It was only performed for one of the three simulations as the geometry of all three simulations are the same and therefore the volume mesh sensitivities of all three simulations were also regarded as being similar.

Sensitivity simulations for the *700hPa DJF simulation* were performed from initialisation, where the prescribed winds enters the model domain, until such time (in seconds) where the simulated winds reach the cells in the mountain domain that are under investigation. Note that these cells were selected in such a way that the weather stations at 1300 m, 1600 m and 1900 m AMSL on Mariepskop, which will later be used for verification (Figure 4-24), are spatially and attitudinally located in the three cells. Sensitivity simulation results of wind speed obtained for a volume mesh with two million cells are depicted in Figure 4-1. These results can now be compared to the results obtained for a volume mesh with nine million cells (shown in Figure 4-2). From the two figures it can be seen that the simulation results

are very similar and that the average wind speed results for the 1300 m, 1600 m and 1900 m AMSL cells correlate relatively well. When calculated, the difference in average wind speed between the two and nine million cell volume meshes' results for 1300 m , 1600 m and 1900 m AMSL are 17%,19% and 1%, respectively. It can therefore be argued that for the purpose of this study, where average values are considered, the increase in mesh size beyond two million cells did not influence the output results of the simulation radically and that the mesh size at nine million cells is therefore suitable for application in this study.

A computer with a Random Access Memory (RAM) of 16 Giga Bytes was used to perform the simulations. Each of the simulations with a volume mesh size of nine million cells took between one and two months to complete (in actual time), depending on the simulation in question. As mentioned before, three simulations were completed, meaning that the computer simulations took five months in total to complete. The reason for the long simulation times is because for an unsteady time-step method (as in the case of the simulations performed in this study), each of the Navier Stokes governing equations has to be solved for all nine million cells during each iteration, which is a very time consuming process.

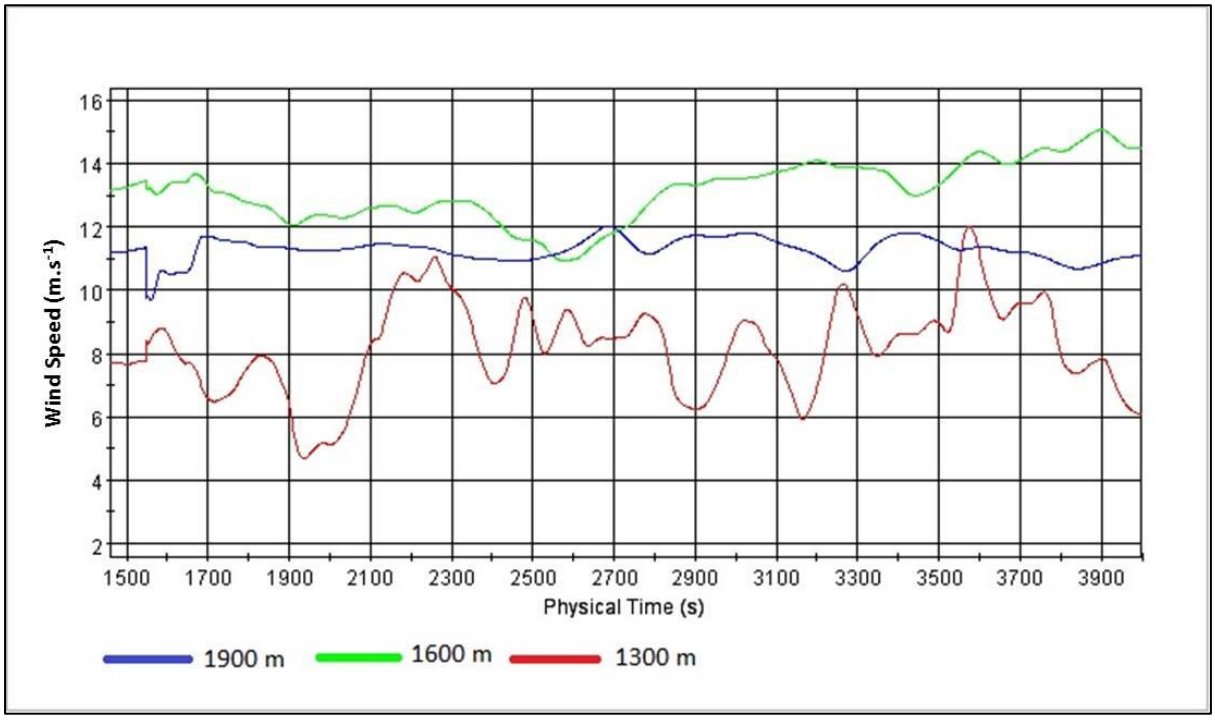

Figure 4-1:
Sensitivity study model simulated wind speed results ($m.s^{-1}$) at 1300 m, 1600 m and 1900 m Above Mean Sea Level (AMSL) for the *700 hPa DJF simulation* over a period of approximately 4000 seconds. These results were obtained for a volume mesh with two million cells.

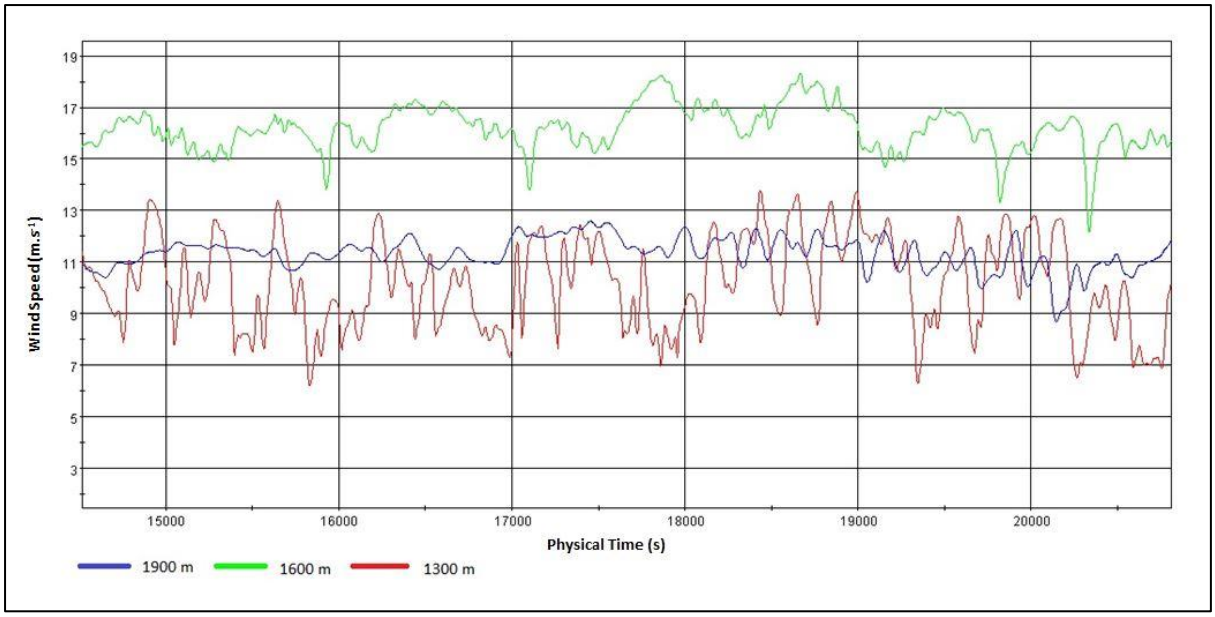

Figure 4-2:
Sensitivity study model simulated wind speed results ($m.s^{-1}$) at 1300 m, 1600 m and 1900 m Above Mean Sea Level (AMSL) for the *700 hPa DJF simulation* over a period of approximately 4000 seconds. These results were obtained for a volume mesh with nine million cells.

4.3 Model stabilization

The model was assumed to be stabilized when all the residuals (momentum, continuity, turbulence kinetic and turbulent dissipation rate) has converged to an expectable value (10^{-3}) for an unstable flow phenomena such as in the case of this study were excessive separation occurs. Graphs of the residuals for the *700 hPa DJF simulation*, *850 hPa JJA simulation* and *700 hPa JJA simulation* are shown in Figures 4-3 to 4-5.

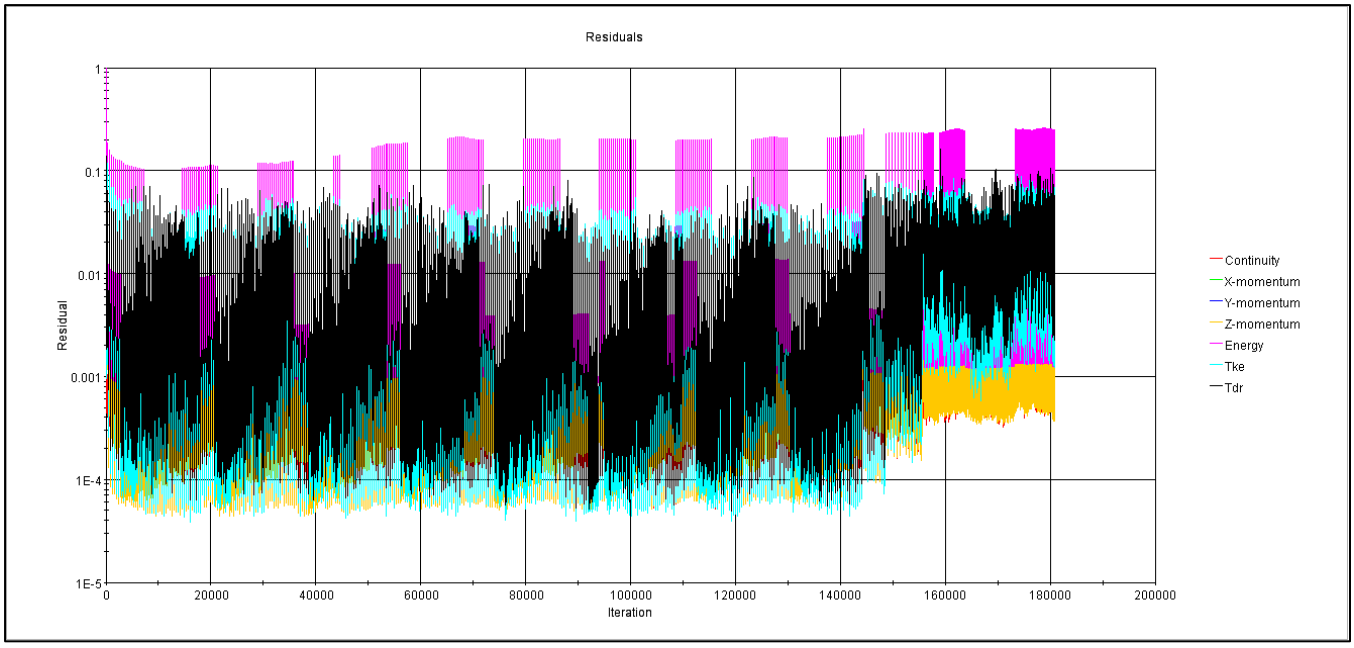

Figure 4-3:
A graph showing the residuals for the 700 hPa DJF simulation.

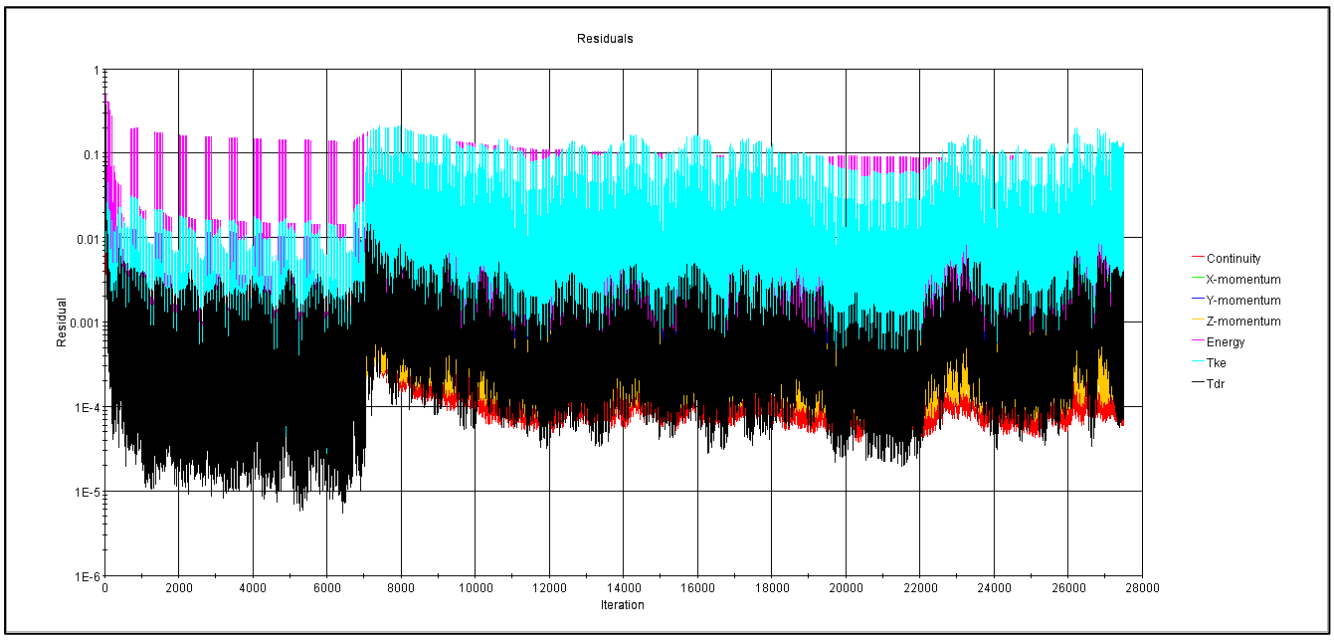

Figure 4-4:

A graph showing the residuals for the 850 hPa JJA simulation.

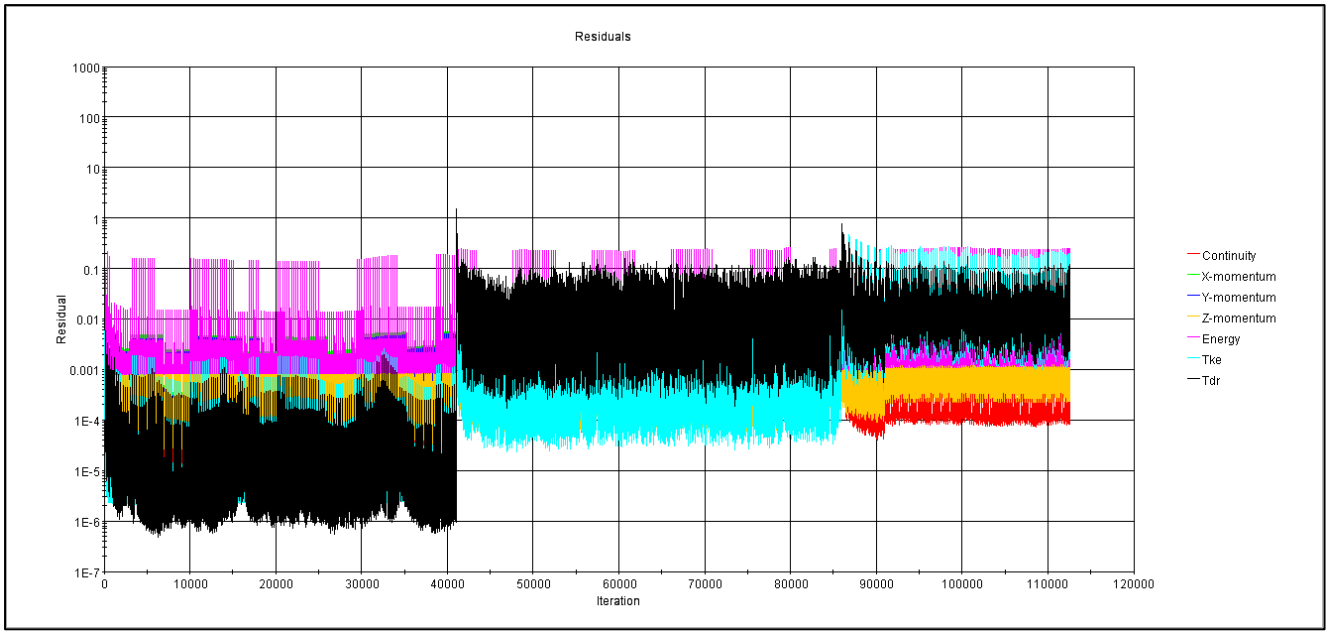

Figure 4-5:

A graph showing the residuals for the 700 hPa JJA simulation.

4.4 Wind speed

In this section model simulated wind speed are verified against the associated averaged observed winds measured by the three weather stations at 1300 m, 1600 m and 1900 m AMSL on Mariepskop. Note that model simulated winds represent interpolated NCEP-NCAR long-term averages, as discussed in previous Chapters, while verification is performed by using shorter-term averages from the three point stations. These shorter-terms extended over one season (DJF of 2010-2011 or JJA of 2011), and averages of hourly data were calculated. Since observations from the three point stations were the only recorded data available, it was assumed that hourly averages taken over a season from these stations are representative of the climate. A more comprehensive verification may be performed in the future when longer-term observations become available.

It is important that each simulation be run for a long enough time span (physical model time) in order to allow air flow from the boundary of the domain to reach the position of Mariepskop (in the centre of the domain) at least once. This equates to at least 4000 s of model time over a distance of 11 km from the boundary of the simulated domain to the position of Mariepskop. The ideal would have been to run the simulations until a wind speed pattern evolves (the period of each pattern starting with wind flow at the boundary and ending with flow reaching the mountain), but due to time and computing power constraints (as mentioned in the previous section) it was only possible to run each simulation for approximately one such a period.

4.4.1 700 hPa DJF simulation

4.4.1.1 Simulation results

Figure 4-2 shows the model simulated wind speed results at 1300 m, 1600 m and 1900 m AMSL cells as a function of model time for the *700 hPa DJF simulation*. The model simulated that 1600 m AMSL experiences the highest wind speeds, followed by 1900 m AMSL and 1300 m AMSL (in that order). According to the model, the average wind speed at 1600 m AMSL is approximately 16 m.s^{-1} whereas the average wind speed at 1900 m and 1300 m AMSL was around 11 m.s^{-1} and 10 m.s^{-1}, respectively.

4.4.1.2 Verification

4.4.1.2.1 1300 m Weather station

The wind speed classes observed at the 1300 m weather station during the DJF months are shown in Figure 4-3. From the figure it is clear that the dominant wind speed class is the 0.5 to 2.1 m.s^{-1} class (with a frequency of occurrence of 64.7%), followed by the wind speed class consisting of calm conditions (wind speeds less than 0.5 m.s^{-1}), with a frequency of occurrence of 25.2%.

It is therefore clear that the STAR-CCM+ model over predicted DJF wind speeds at 1300 m AMSL by 7 to 9 m.s^{-1} (see Figure 4-2). The reason for this is probably because the STAR-CCM+ model is forced with a wind speed profile that stays constant over time.

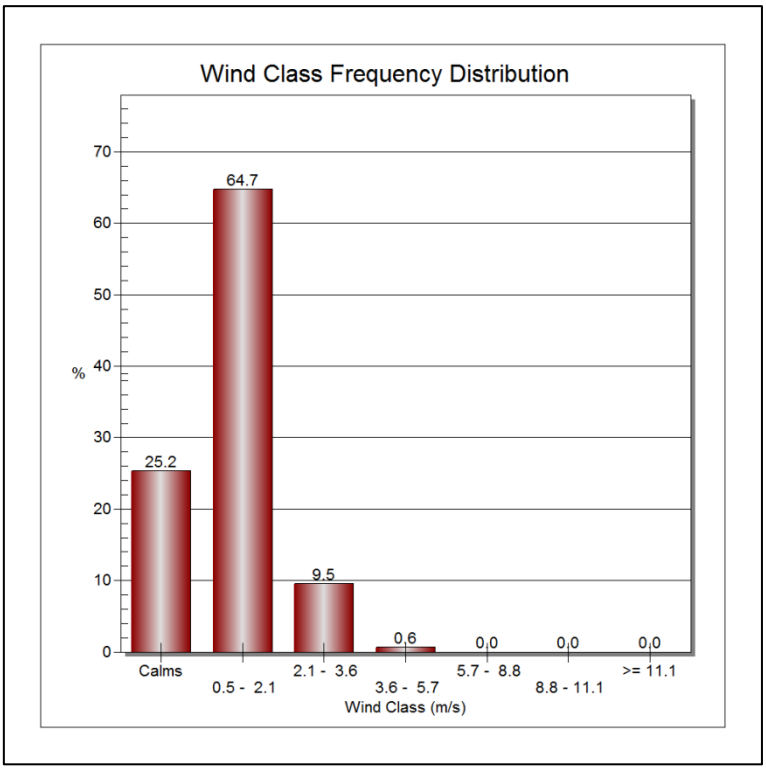

Figure 4-6:
Wind class frequency distribution (%) for the 1300 m Above Mean Sea Level (AMSL) weather station on Mariepskop during the months of December, January and February (DJF) in the 2010-1011 season.

4.4.1.2.2 1600 m Weather station

The wind speed class distribution observed at the 1600 m AMSL weather station on Mariepskop for the DJF months is shown in Figure 4-4. The dominant wind speed class at this elevation is the 0.5 to 2.1 m.s^{-1} class (with a frequency of occurrence of 44.4%) followed by the 2.1 to 3.6 m.s^{-1} (40.0%) class and the 3.6 to 5.7 m.s^{-1} (13.4%) class.

It is evident that the STAR-CCM+ model over predicted the wind speed at this elevation as well. However, the model did predict the 1600 m to have higher wind speeds than the 1300 m elevation, which was also reflected by the observed results.

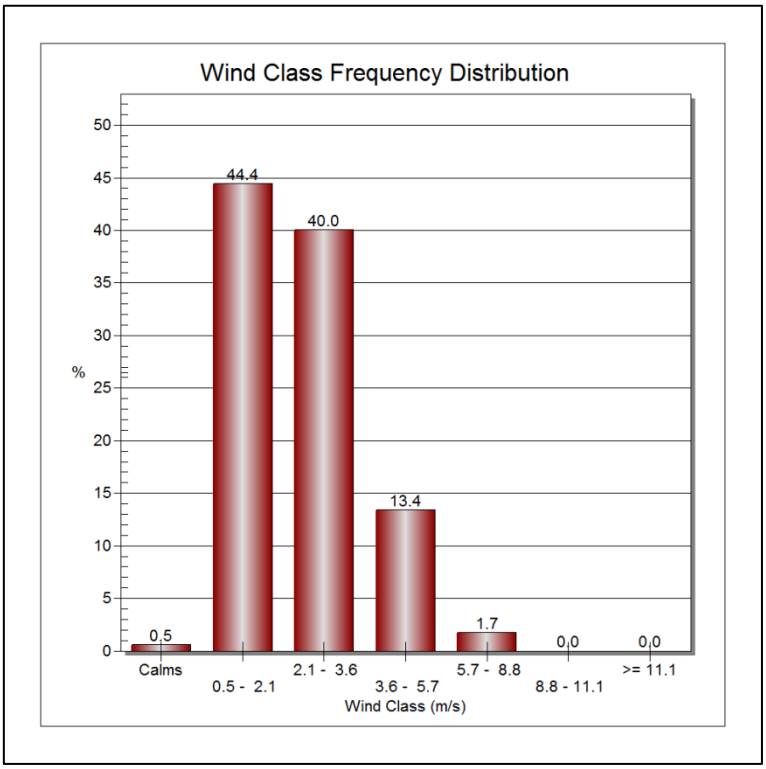

Figure 4-7:
Wind class frequency distribution (%) for the 1600 m Above Mean Sea Level (AMSL) weather station on Mariepskop during the months of December, January and February (DJF) in the 2010-2011 season.

4.4.1.2.3 1900 m Weather station

The wind speed class distribution observed at 1900 m AMSL on Mariepskop is depicted in Figure 4-5. From the figure it is clear that the dominant wind speed class is the 0.5 to 2.1 m.s^{-1} class (29.4%) followed by the 2.1 to 3.6 m.s^{-1} (24.8%) class and 3.6 to 5.7 m.s^{-1} class (22.7%).

It is clear that the STAR-CCM+ model also over predicted wind speeds at 1900 m AMSL. From the observed results it can be seen that the 1300 m wind speeds are the lowest compared to 1600 m and 1900 m AMSL. It can further be seen that the 1600 m speeds are lower than the 1900 m speeds. The simulated results show 1300 m AMSL as having the lowest wind speeds, but the 1600 m and 1900 m relative wind speeds were not portrayed accurately by the model.

The reason for this inaccuracy is most probably related to boundary conditions which may not reflect the reality in the region of Mariepskop. Boundary conditions were obtained by interpolating reanalysis data at the position of Mariepskop (refer to Chapter 2 of this document); it is possible that local conditions in reality may differ from the regional average interpolated conditions during the DJF months.

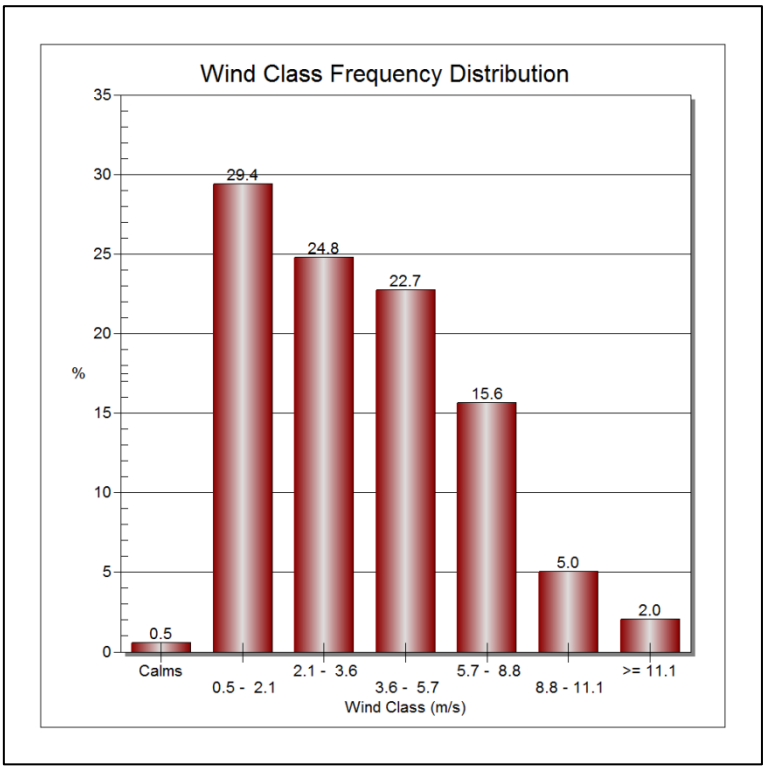

Figure 4-8:
Wind class frequency distribution (%) for the 1900 m Above Mean Sea Level (AMSL) weather station on Mariepskop during the months of December, January and February (DJF) in the 2010-2011 season.

4.4.2 700 hPa JJA simulation

4.4.2.1 Simulation results

The modelled wind speed results for the *700 hPa JJA simulation* is shown in Figure 4-6. The simulation output shows variable results. The 1900 m wind speeds vary between 1.5 $m.s^{-1}$

and 9 m.s^{-1}, whereas the 1600 m speeds vary between 1.5 m.s^{-1} and 6 m.s^{-1} and the 1300 m speeds vary between 1.2 m.s^{-1} and 7 m.s^{-1}. On average, the highest wind speeds were modelled for 1900 m AMSL. Very similar speeds were modelled, on average, for 1300 m and 1600 m AMSL.

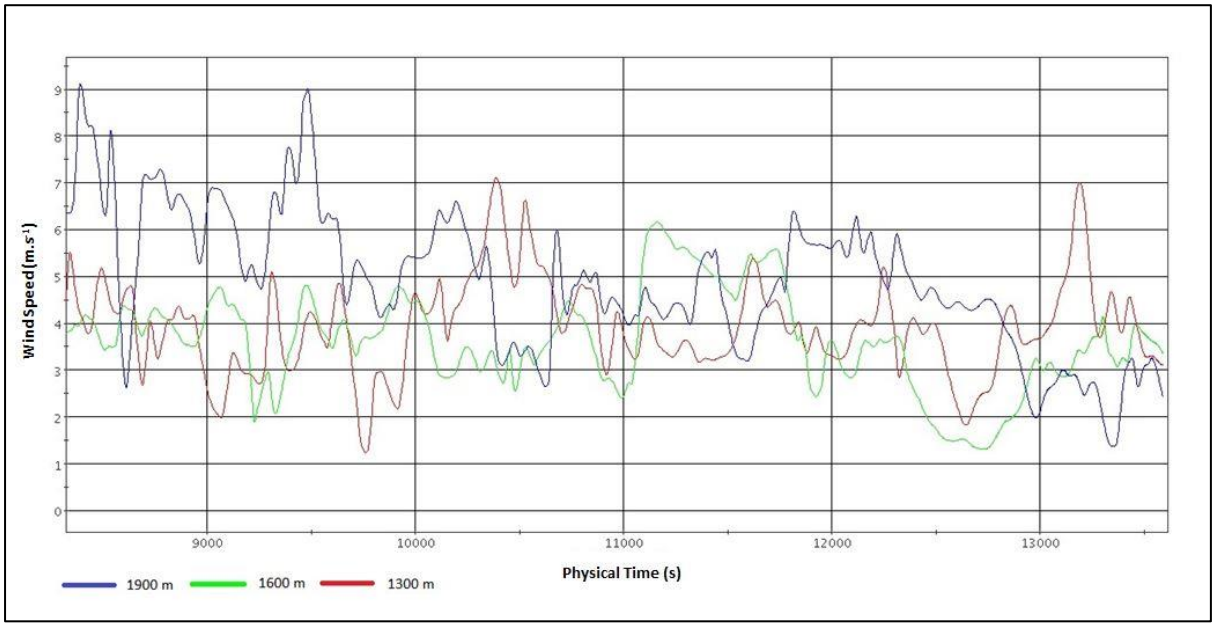

Figure 4-9:
Modelled wind speed results (m.s^{-1}) at 1300 m, 1600 m and 1900m Above Mean Sea Level (AMSL) for the *700 hPa JJA simulation*.

4.4.2.2 Verification

4.4.2.2.1 1300 m Weather station

The wind speed distribution observed at the 1300 m weather station for the JJA months (2011) is given in Figure 4-7. From the figure it is clear that the dominant wind speed class is the 0.5 to 2.1 m.s^{-1} class (66.6%), followed by the calm wind speed class with wind speeds between m.s^{-1} and 0.5 m.s^{-1} (20.6 %) and the 2.1 to 3.6 m.s^{-1} class (12.7%).

It can be seen that the modelled wind speeds for the *700 hPa JJA simulation* at 1300 m AMSL (Figure 4-6) is in better agreement with the observed results (at the 1300 m weather station on Mariepskop) than the DJF modelled results.

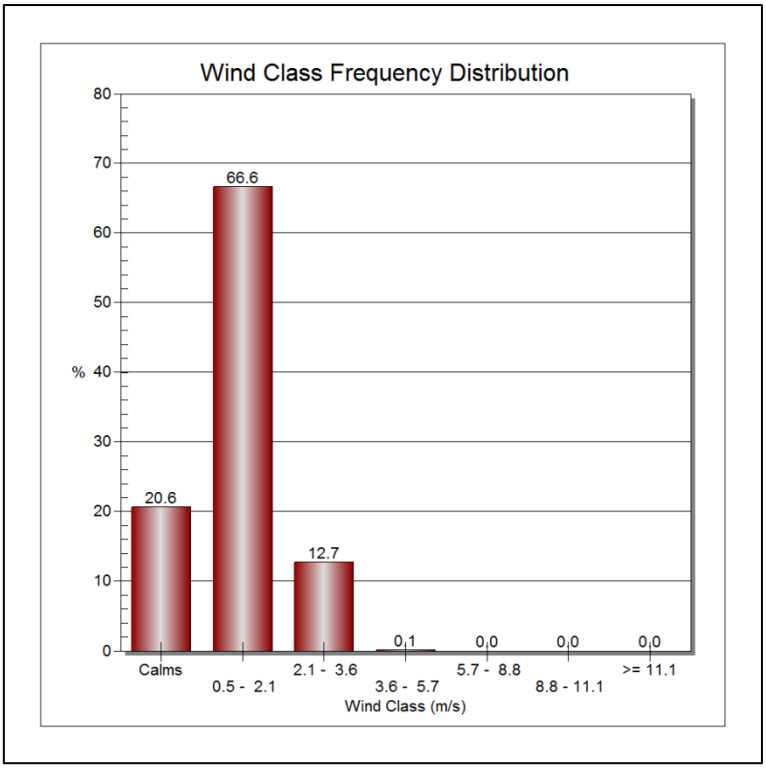

Figure 4-10:
Wind class frequency distribution (%) for the 1300 m Above Mean Sea Level (AMSL) weather station on Mariepskop during the months of June, July and August (JJA) in the 2011 season.

4.4.2.2.2 1600 m Weather station

Figure 4-8 depicts the wind class frequency distribution observed by the 1600 m weather station on Mariepskop. The dominant wind speed class is the 0.5 to 2.1 $m.s^{-1}$ class (62.8%), followed by the 2.1 to 3.6 $m.s^{-1}$ and 3.6 to 5.7 $m.s^{-1}$ classes. It is clear that the average observed wind speeds at 1600 m AMSL are higher than those at 1300 m AMSL; this cannot be seen clearly in the *700 hPa JJA simulation* results. However, the modelled wind speed for 1600 m AMSL reflects reality relatively well.

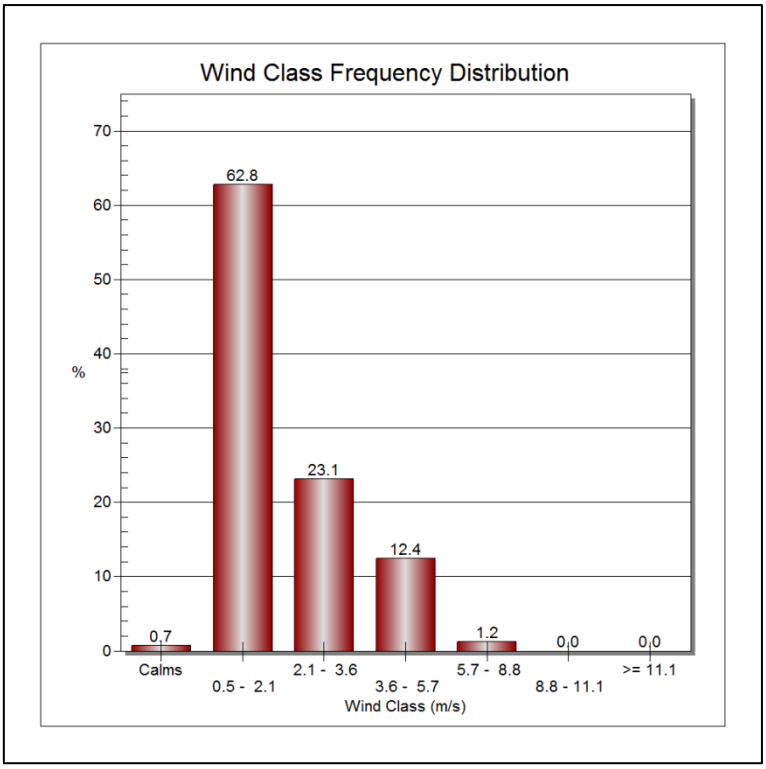

Figure 4-11:
Wind class frequency distribution (%) for the 1600 m Above Mean Sea Level (AMSL) weather station on Mariepskop during the.months of June, July and August (JJA) in the 2011 season.

4.4.2.2.3 1900 m Weather station

The wind class frequency distribution graph for the JJA months (2011) as observed by the 1900 m weather station on Mariepskop can be seen in Figure 4-9. The 2.1 to 3.6 $m.s^{-1}$ wind speed class dominates (25.9%), followed by the 3.6 to 5.7 $m.s^{-1}$ (22.6%) and 5.7 to 8.8 $m.s^{-1}$ (22.3 %) classes. It is clear that, on average, the 1900 m weather station experiences the highest wind speeds of the three weather stations, followed by the 1600 m station. The 1300 m station experiences the lowest wind speeds and the calmest conditions. This trend was captured by the *700 hPa JJA simulation*. The observed wind speeds at 1900 m AMSL and the modelled wind speeds agree relatively well.

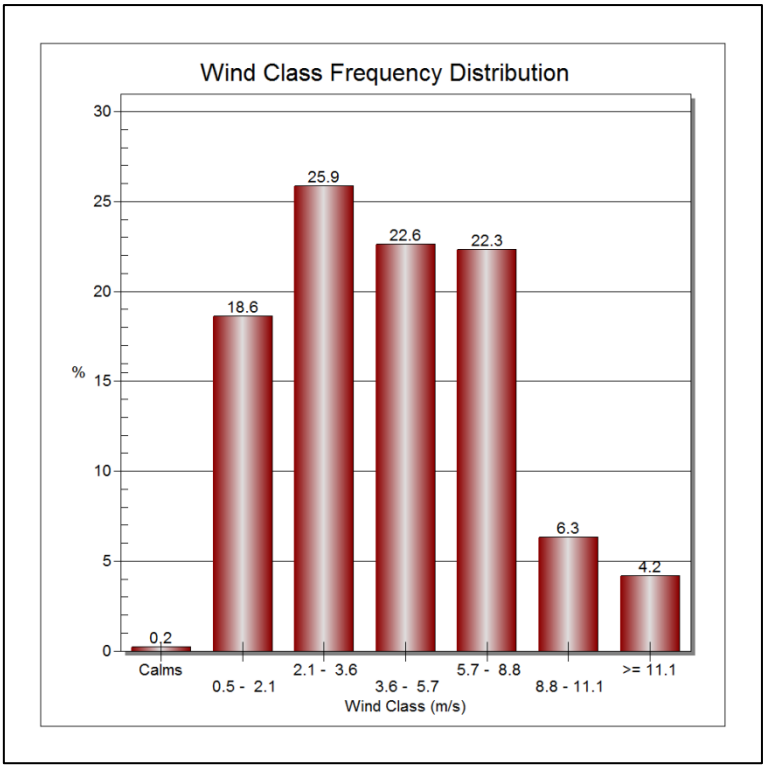

Figure 4-12:
Wind class frequency distribution (%) for the 1900 m Above Mean Sea Level (AMSL) weather station on Mariepskop during the months of June, July and August (JJA) in the 2011 season.

4.4.3 850 hPa JJA simulation

4.4.3.1 Simulation results

The modelled wind speed results for the *850 hPa JJA simulation* are shown in Figure 4-10. The modelled wind speed results are variable. The 1600 m results vary between 2.5 $m.s^{-1}$ and 6.5 $m.s^{-1}$ whereas the 1900 m results vary between 0.2 $m.s^{-1}$ and 6.8 $m.s^{-1}$. The 1300 m results vary less and are between a minimum of around 1 $m.s^{-1}$ and a maximum of approximately 2.8 $m.s^{-1}$. On average, 1600 m AMSL has the highest modelled wind speeds, followed by 1900 m and 1300 m AMSL.

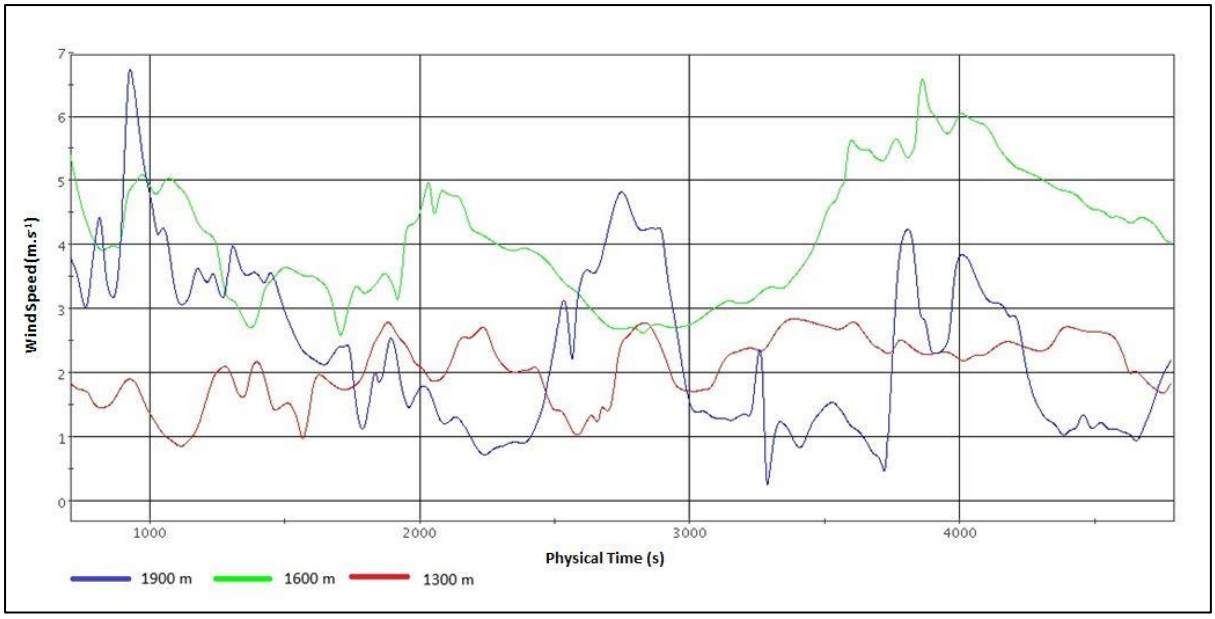

Figure 4-13:
Modelled wind speed results ($m.s^{-1}$) at 1300 m, 1600 m and 1900 m Above Mean Sea Level (AMSL) for the *850 hPa JJA simulation*.

4.4.3.2 Verification

The modelled wind speed results for the *850 hPa JJA simulation* can be verified against the observed wind speed class frequency distribution histograms for the months of JJA (2011) at the 1300 m, 1600 m and 1900 m weather stations as depicted in Figure 4-7, Figure 4-8 and Figure 4-9. It is clear that the 1900 m weather station experienced winds with the highest wind speeds, followed by the 1600 m weather station. The 1300 m station experienced the lowest wind speeds and the calmest conditions. This increase of wind speed with altitude was not captured by the model, as the model simulated wind speeds at the 1600 m to be higher, on average, than those at 1900 m AMSL. However, there were times in the simulation when the model simulated higher wind speeds at 1900 m AMSL. The model did capture the lower wind speeds at 1300 m AMSL relative to 1900 m and 1600 m AMSL reasonably well.

4.4.4 Observations and the literature

During both the DJF and JJA months it was observed that wind speeds increase with an increase in altitude. This finding correlates with existing literature (Stangroom, 2004; Nappo, 1977, Barry, 2008).

4.5 Wind Direction

This section deals with the validation of the modelled wind directions against wind direction observations made by the three weather stations (1300 m, 1600 m and 1900 m AMSL) on Mariepskop.

It is important to note that the Figures 4.11 to 4.19 provide only snapshots at a specific time of the flow. It is the best indication the author could provide of flow direction in a document format. The positions of the weather stations in most instances in Figures 4.11 to 4.19 confer to areas were non-separated flow takes place and therefore some information about non-separated wind direction can be obtained from these figures. The wind fields are meant to show the reader a layout of the domain and give the reader insight in to the typical pattern of flow and are not meant to give absolute values. The “snapshots” of flow were taken after a sufficient time after the model was allowed to stabilize.

4.5.1 700 hPa DJF simulation

4.5.1.1 1300 m AMSL

Figure 4-11 provides a graphic representation of the modelled wind directions at 1300 m AMSL on Mariepskop. The position of the 1300 m weather station is indicated by a red circle. A wind rose representing observed conditions during the months of DJF at the 1300 m weather station (2010-2011) can be seen in the top right corner of Figure 4-11.

The modelled flow direction on the eastern ridge at 1300 m AMSL is predominantly to the north. To the west of the ridge the dominant direction becomes south-south-east and south-east. At the position of the station the dominant modelled wind direction is east, east-north-east and east-south-east. From the figure the assumption can be made that the easterly flow at the weather station is a local topographic effect of the valley and ridge that can be found to the east of the weather station. This predominant easterly flow is very prominent in the wind rose depicting observed conditions. The model simulated flow direction relatively well at this elevation, even though it overestimated wind speed significantly for the DJF months.

4.5.1.2 1600 m AMSL

Figure 4-12 depicts the modelled and the observed wind directions for the *700 hPa DJF simulation* at 1600 m AMSL. Again the wind rose showing observed results at the 1600 m weather station during the months of DJF (2010-2011) is shown in the top right corner of Figure 4-12. From the figure it can be seen that the dominant modelled wind direction over the 1600 m region on Mariepskop is south-east. To the east of the green circle indicating the

position of the 1600 m weather station, topography forces the wind direction into a south-south-easterly and southerly direction. The modelled wind directions at the 1600 m weather station position agree exceptionally well with the observed results which also show a south-east dominancy in wind direction.

4.5.1.3 1900 m AMSL

The modelled and observed wind directions for the *700 hPa DJF simulation* at 1900 m AMSL are indicated in Figure 4-13. The dominant modelled wind direction at this elevation is south-east (similar to 1600 m AMSL). Light blue wind velocity arrows to the north of the 1900 m station position (blue circle) indicate very slow winds with flow in the opposite direction. This possibly represents flow within a separation bubble, as flow within a separation bubble is usually opposite to the main flow direction outside of the bubble. Once again the modelled wind directions correlate very well with the observed results at the 1900 m weather station, indicating a dominant south-easterly wind

4.5.2 700 hPa JJA simulation

4.5.2.1 1300 m AMSL

Modelled and observed wind directions for the *700 hPa JJA simulation* at 1300 m AMSL is depicted in Figure 4-14. The topographical disturbance of the valley to the east of the 1300 m weather station position in Figure 4-14 again has a pronounced effect on the modelled wind directions. Wind directions modelled in the vicinity of the weather station position vary substantially in a small area from a southerly direction, to a north-north-easterly, north-westerly and a south-south-easterly direction. The dominant observed wind direction at this elevation is south-south-east, followed by a south-westerly direction. It is difficult to establish with certainty that the model was able to simulate wind direction accurately at this elevation. It is therefore important to look at the results of the other two modelled elevations before coming to any conclusions regarding the accuracy of the model in capturing the observed results.

4.5.2.2 1600 m AMSL

Figure 4-15 depicts wind flow and observed wind directions at 1600 m AMSL for the *700 hPa JJA simulation*. The dominant modelled wind directions are south-west in the region west of the weather station position and west-south-west at the weather station position and east of it. The dominant observed wind direction at the 1600 m weather station is west. It is clear that the modelled wind direction is within 25 ˚ of the dominant observed wind direction. It is

evident that the model was able to capture wind direction at 1600 m AMSL for the 700 hPa JJA conditions reasonably well.

4.5.2.3 1900 m AMSL

Modelled and observed wind directions at 1900 m AMSL for the *700 hPa JJA simulation* can be seen in Figure 4-16. The dominant modelled wind direction at this elevation is west. This coincides well with the observed results obtained from the 1900 m weather station for JJA.

4.5.3 850 hPa JJA simulation

4.5.3.1 1300 m AMSL

Figure 4-17 depicts the modelled and observed wind directions for the *850 hPa JJA simulation* at 1300 m AMSL on Mariepskop. The dominant modelled wind direction at 1300 m AMSL is south-south-east. This agrees with the dominant observed wind direction at the 1300 m weather station during the winter months of JJA (2011) (as depicted in the top right corner of Figure 4-17). The scattering of wind in variable directions by the valley to the east of the position of the 1300 m weather station may explain the variability in wind directions observed by the 1300 m weather station.

4.5.3.2 1600 m AMSL

Figure 4-18 depicts the modelled and observed wind directions at 1600 m AMSL for the *850 hPa JJA simulation*. The dominant wind direction modelled at this elevation (and also at the position of the 1600 m weather station) is a south-south-easterly direction. When compared to the results observed by the 1600 m weather station, it is clear that the model correlates to the second most dominant direction (also south-south-east). This is also the direction from which the stronger winds blew. The dominant wind direction in terms of frequency observed by the weather station is a westerly wind, but it can be seen from the wind rose that winds from the west mostly had very low speeds (speeds less than 2.1 $m.s^{-1}$ on average). The model was therefore successful in capturing the conditions when stronger winds prevail. A constant wind was forced across the boundaries of the model, therefore the model could not simulate calm conditions and thus only average, windy conditions could be captured.

4.5.3.3 1900 m AMSL

Figure 4-19 indicates the modelled and observed flow directions for the *850 JJA simulation* at 1900 m AMSL on Mariepskop. At the point of the 1900 m weather station (indicated by a blue circle) topographical effects force modelled wind directions to be relatively variable. At the weather station position wind directions range from north-north-east to the east of the weather station to north-north-west to the west of the weather station. The weather station observations during the winter months of JJA also show a greater variability than that of the 1300 m and 1600 m stations. The model captured the observed north-north-eastern winds relatively well but failed to capture the dominant wind from the west and the north-west.

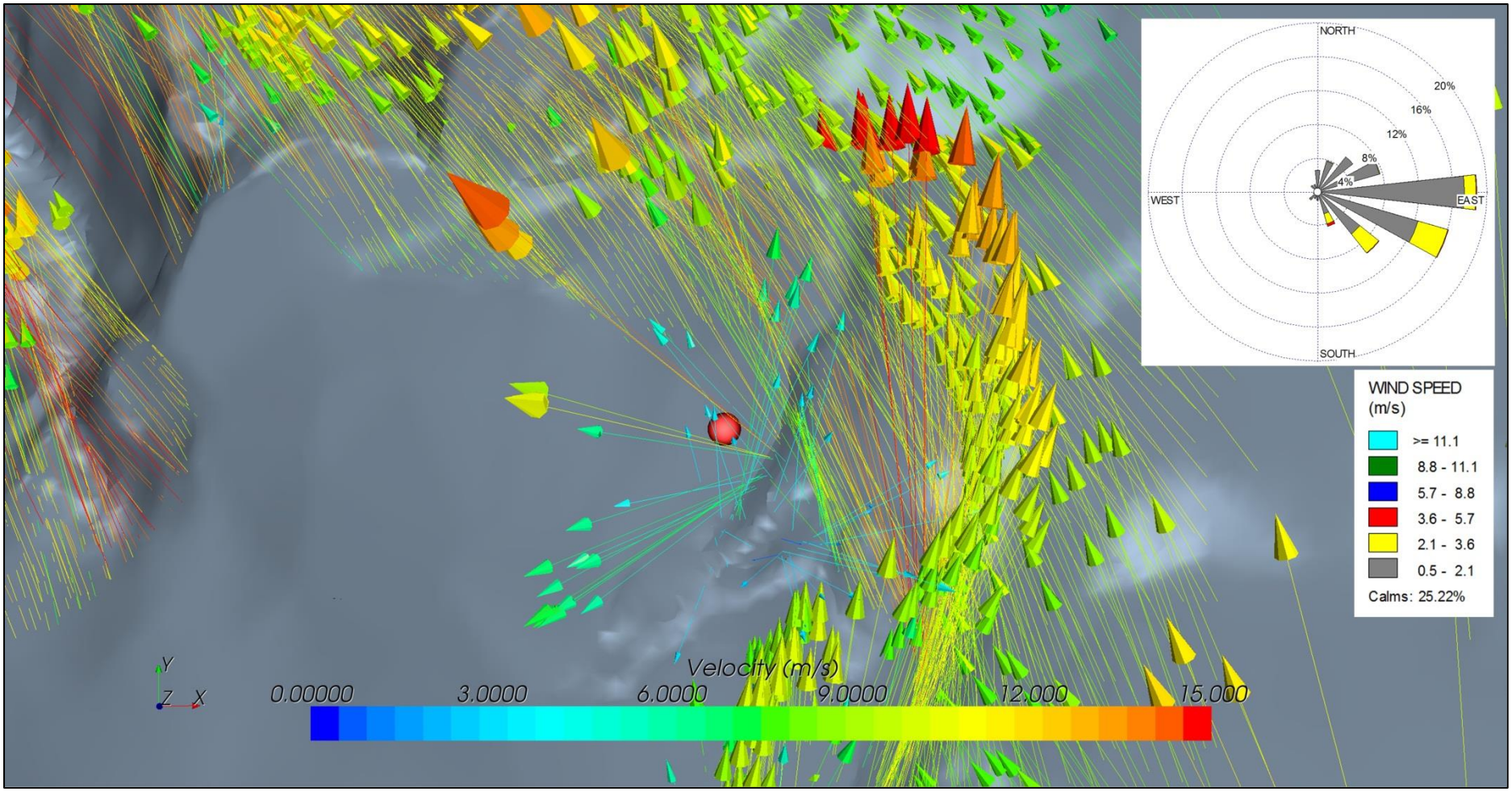

Figure 4-14:
700 hPa DJF simulated (arrows) and observed (wind rose – top right) results of wind speed and direction at 1300 m Above Mean Sea Level (AMSL) on Mariepskop. The red circle represents the position of the 1300 m weather station.

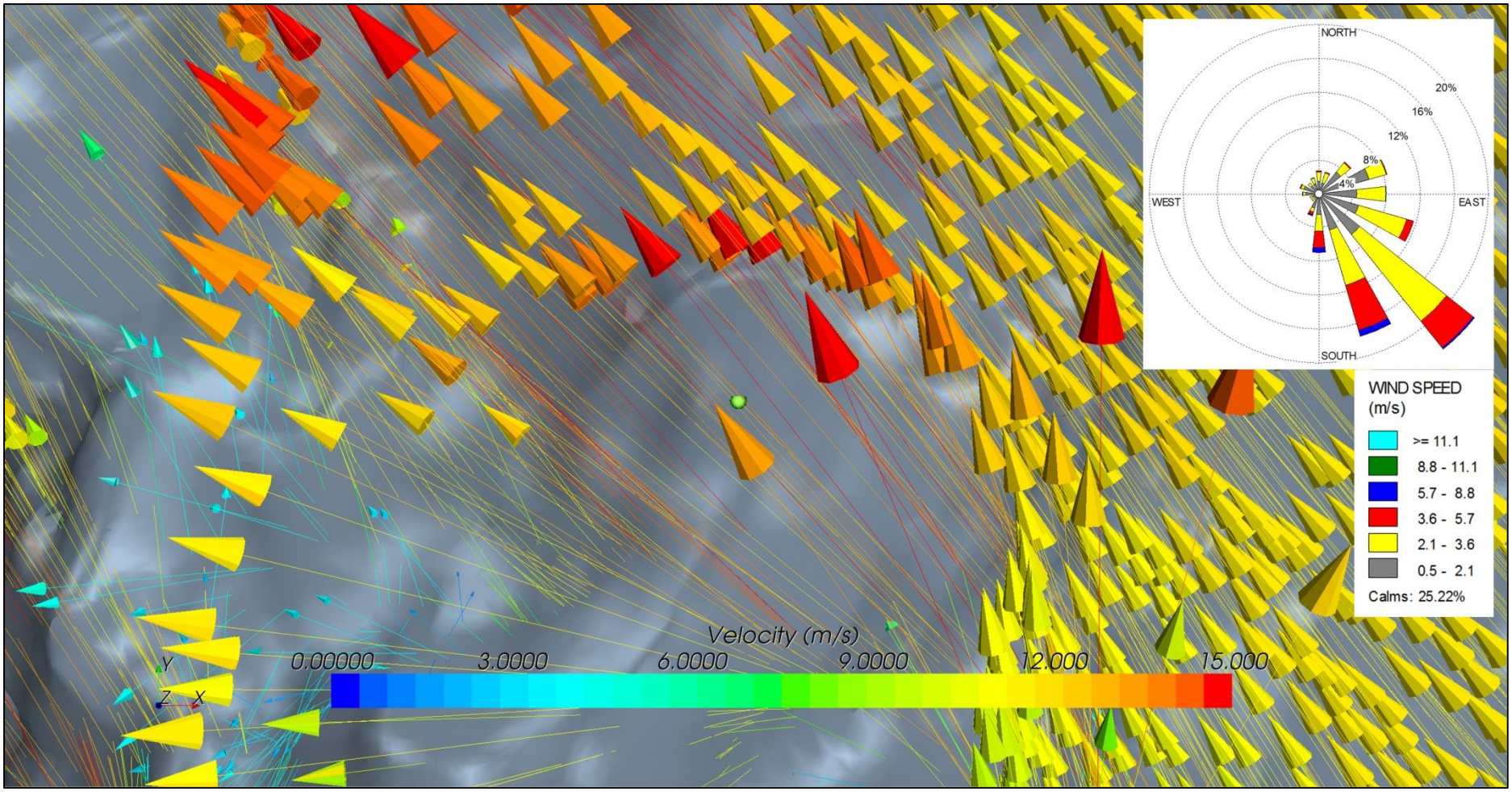

Figure 4-15:
700 hPa DJF simulated (arrows) and observed (wind rose – top right) results of wind speed and direction at 1600 m Above Mean Sea Level (AMSL) on Mariepskop. The green circle represents the position of the 1600 m weather station.

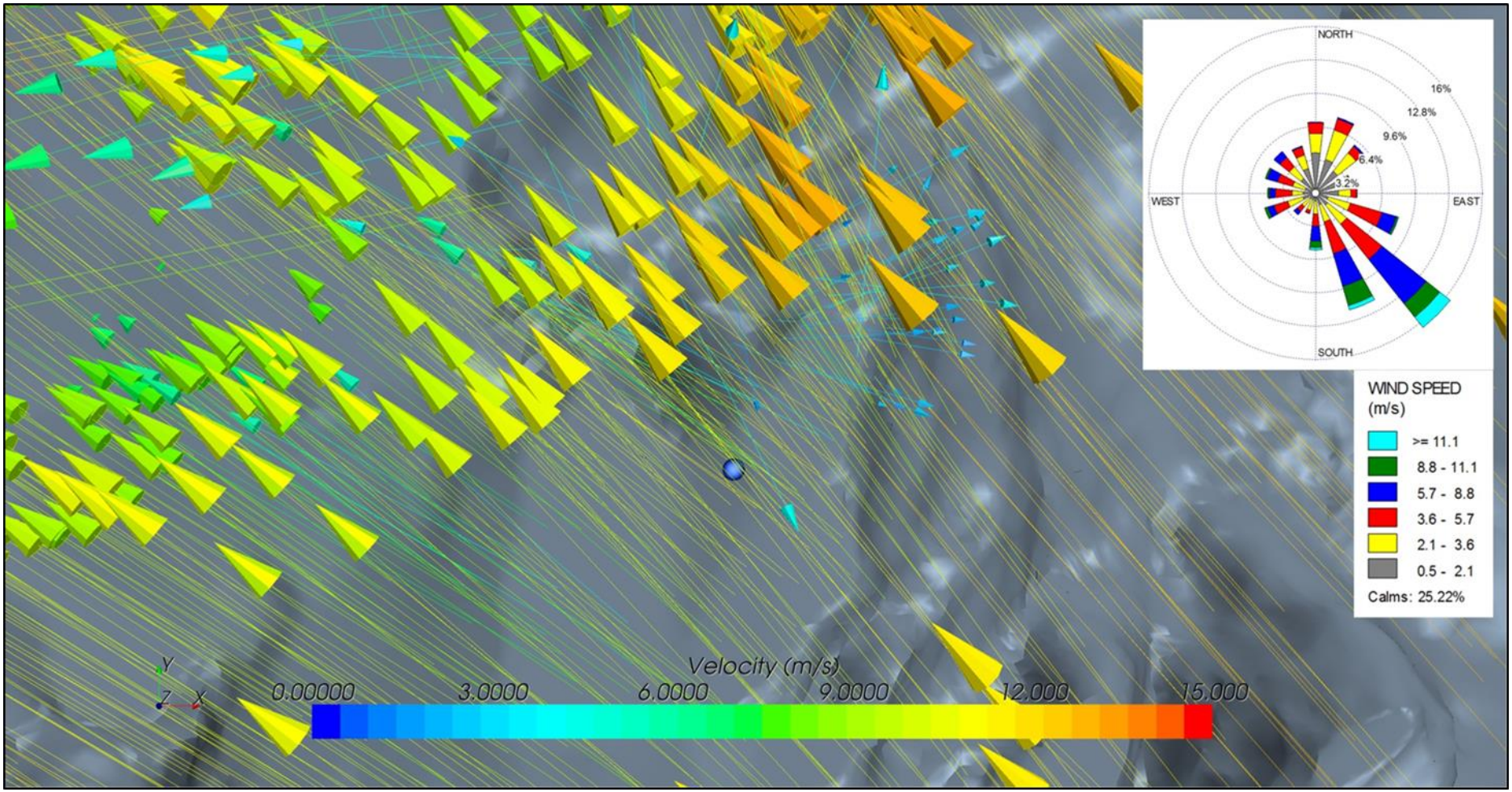

Figure 4-16:
700 hPa DJF simulated (arrows) and observed (wind rose – top right) results of wind speed and direction at 1900 m Above Mean Sea Level (AMSL) on Mariepskop. The blue circle represents the position of the 1900 m weather station.

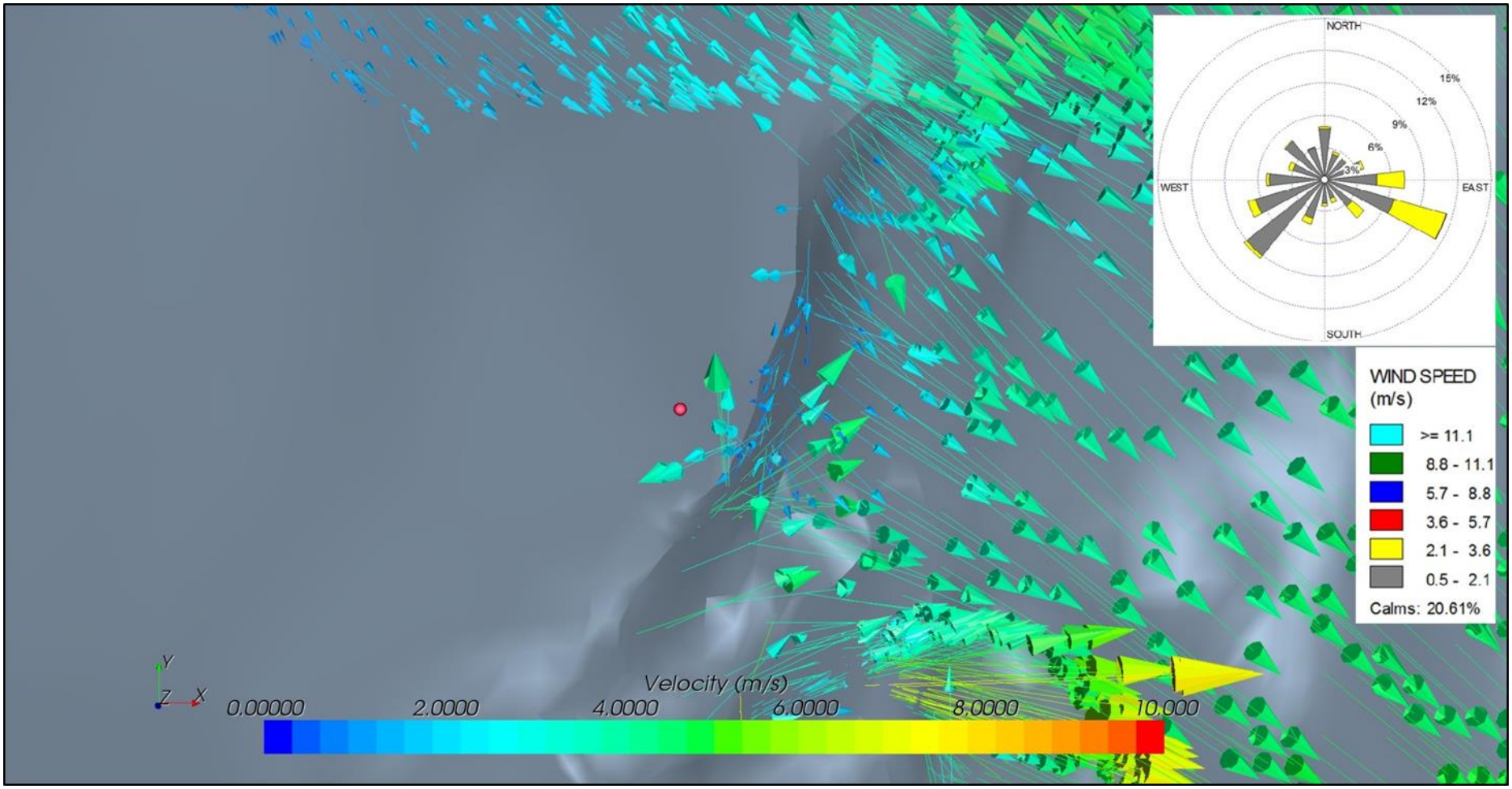

Figure 4-17:
700 hPa JJA simulated (arrows) and observed (wind rose – top right) results of wind speed and direction at 1300 m Above Mean Sea Level (AMSL) on Mariepskop. The red circle represents the position of the 1300 m weather station.

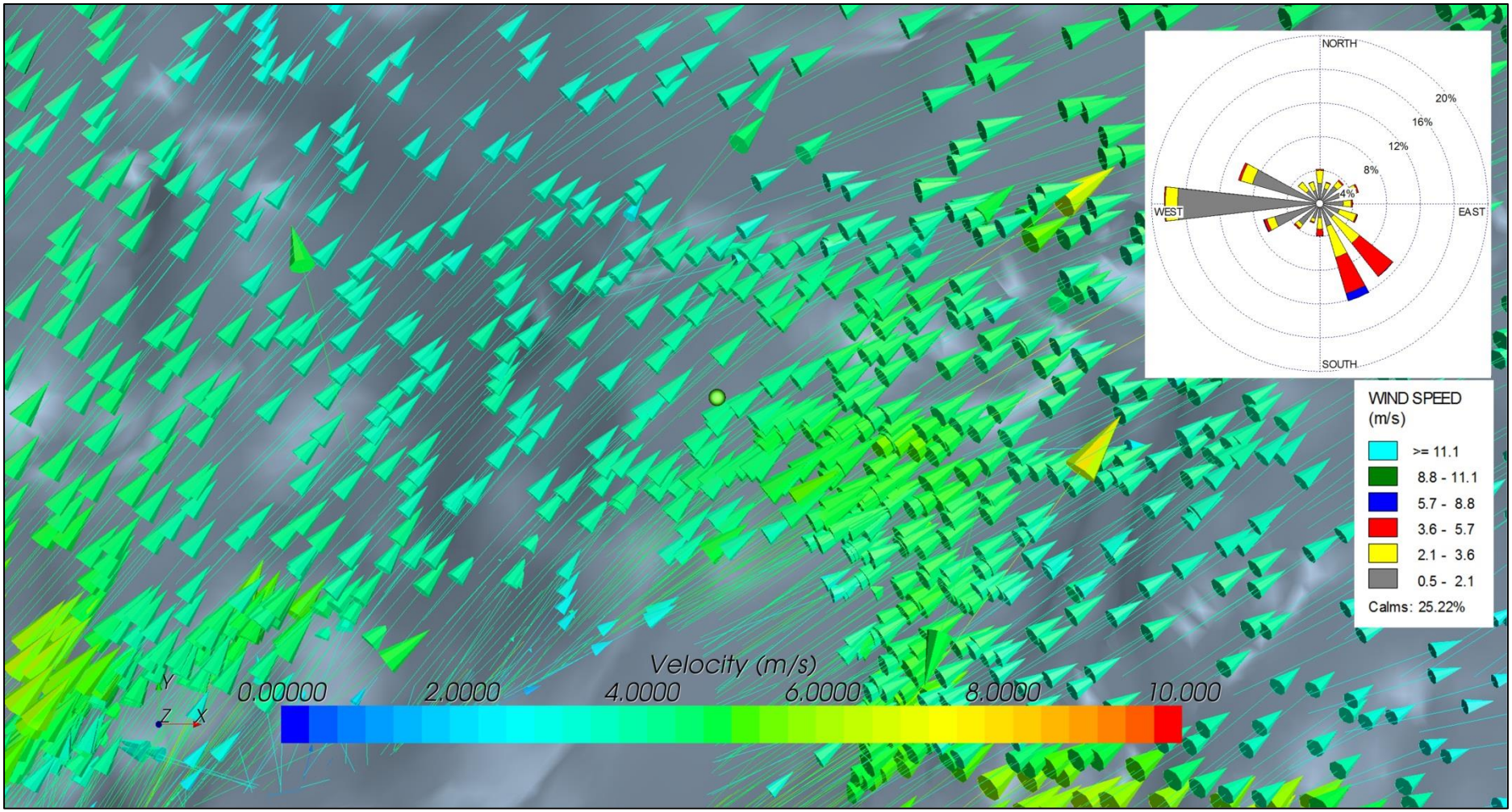

Figure 4-18:
700 hPa JJA simulated (arrows) and observed (wind rose – top right) results of wind speed and direction at 1600 m Above Mean Sea Level (AMSL) on Mariepskop. The green circle represents the position of the 1600 m weather station.

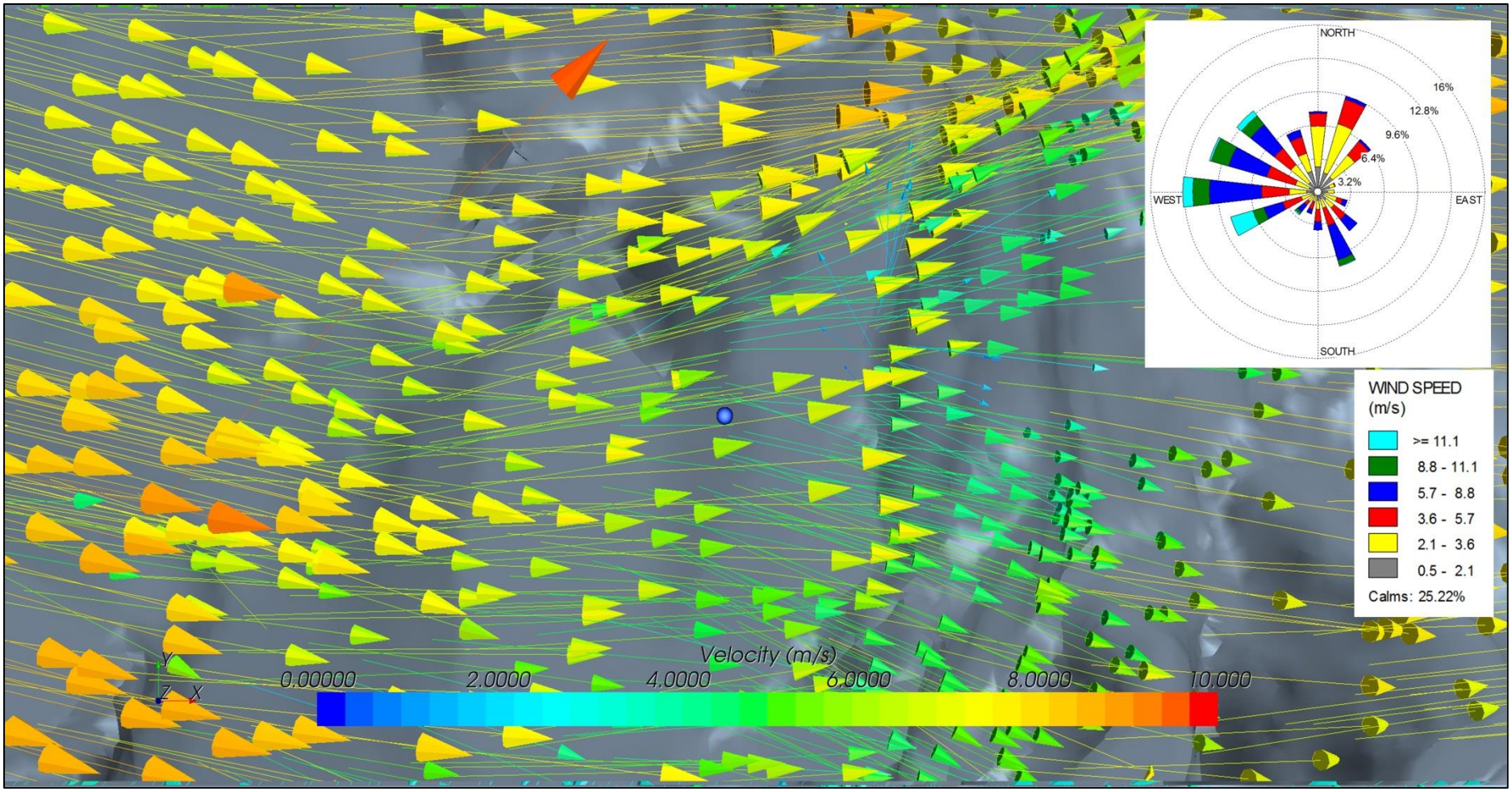

Figure 4-19:
700 hPa JJA simulated (arrows) and observed (wind rose – top right) results of wind speed and direction at 1900 m Above Mean Sea Level (AMSL) on Mariepskop. The blue circle represents the position of the 1900 m weather station.

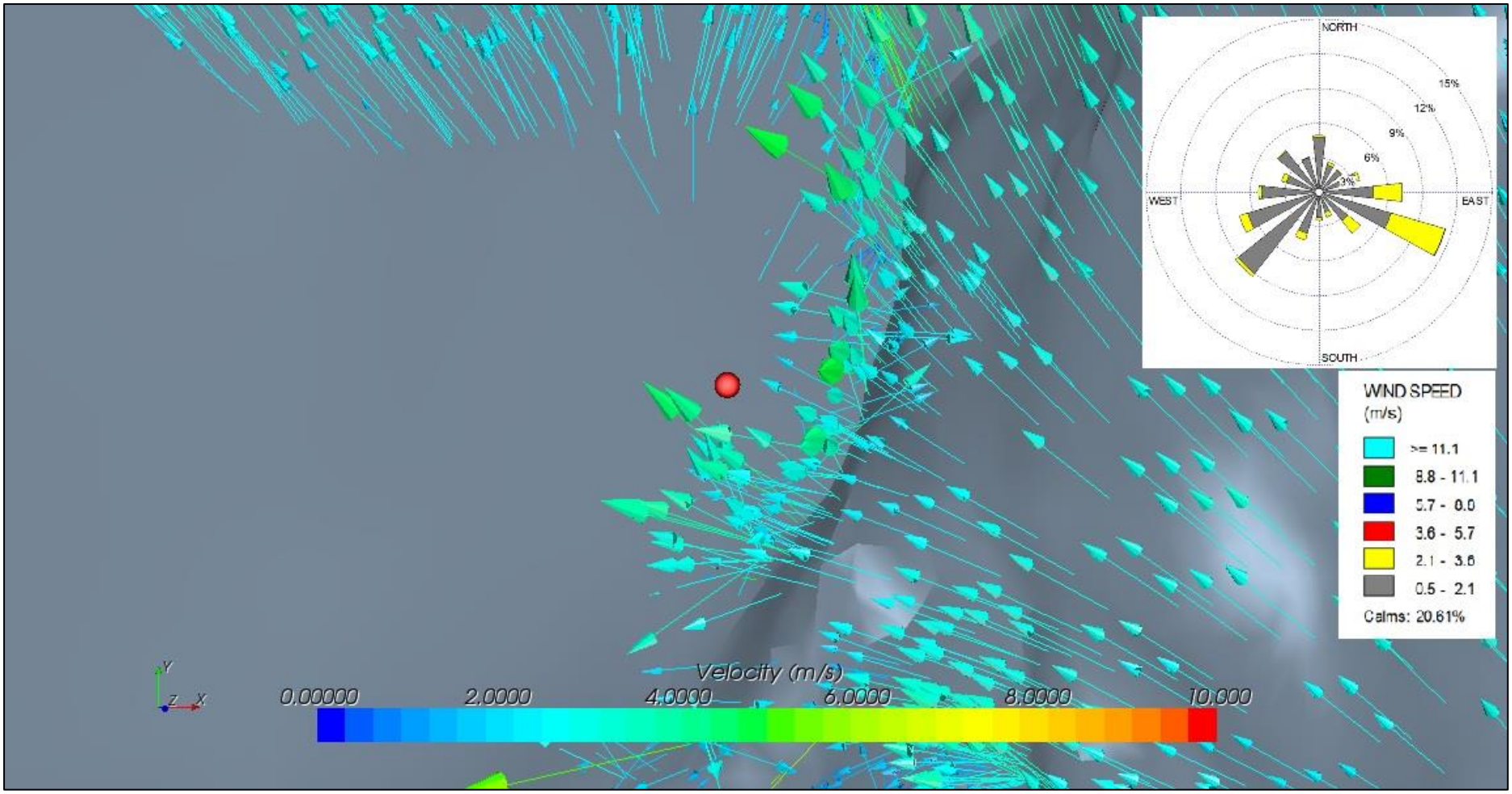

Figure 4-20:
850 hPa JJA simulated (arrows) and observed (wind rose – top right) results of wind speed and direction at 1300 m Above Mean Sea Level (AMSL) on Mariepskop.. The red circle represents the position of the 1300 m weather station.

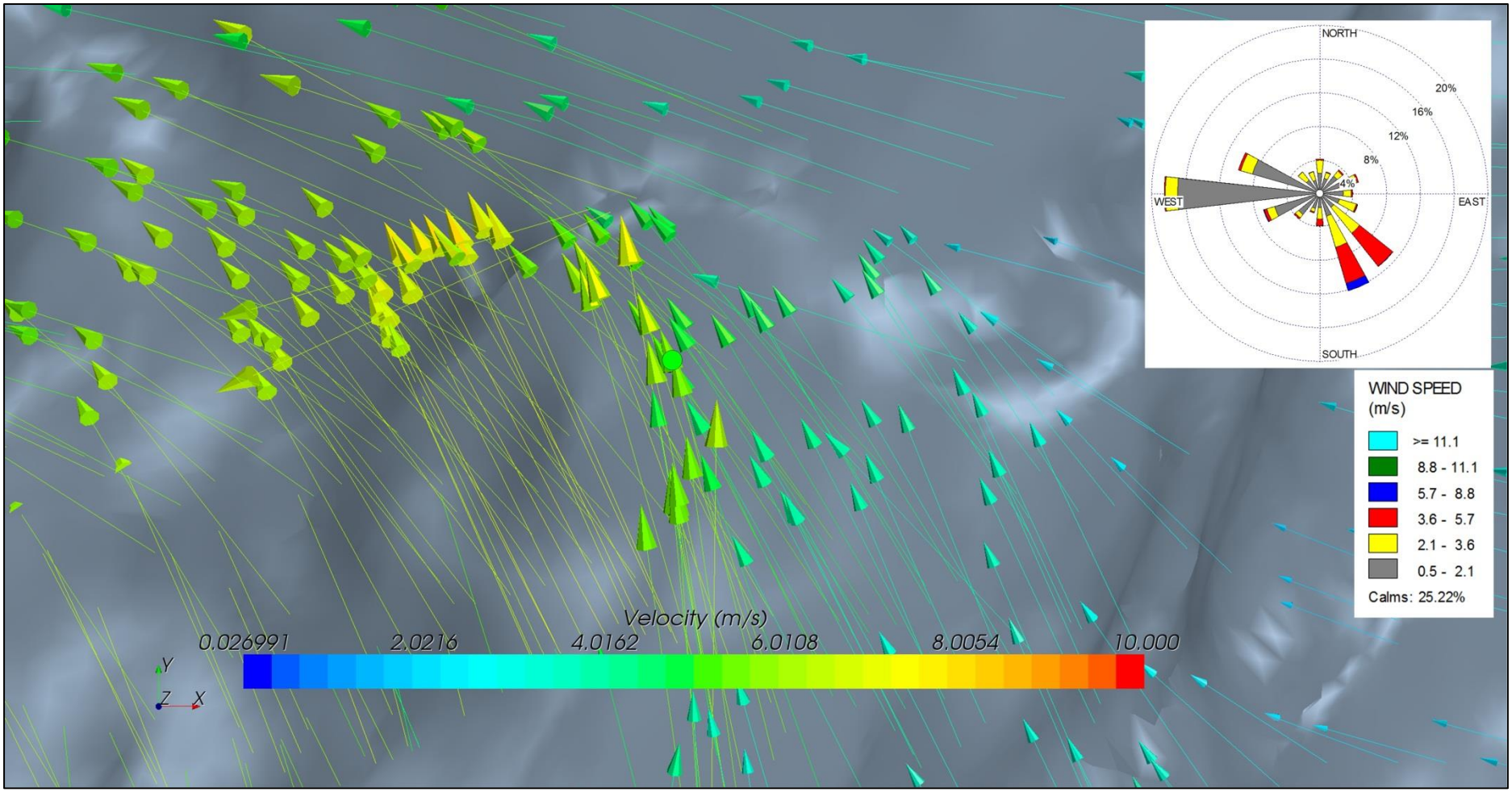

Figure 4-21:
850 hPa JJA simulated (arrows) and observed (wind rose – top right) results of wind speed and direction at 1600 m Above Mean Sea Level (AMSL) on Mariepskop. The green circle represents the position of the 1600 m weather station.

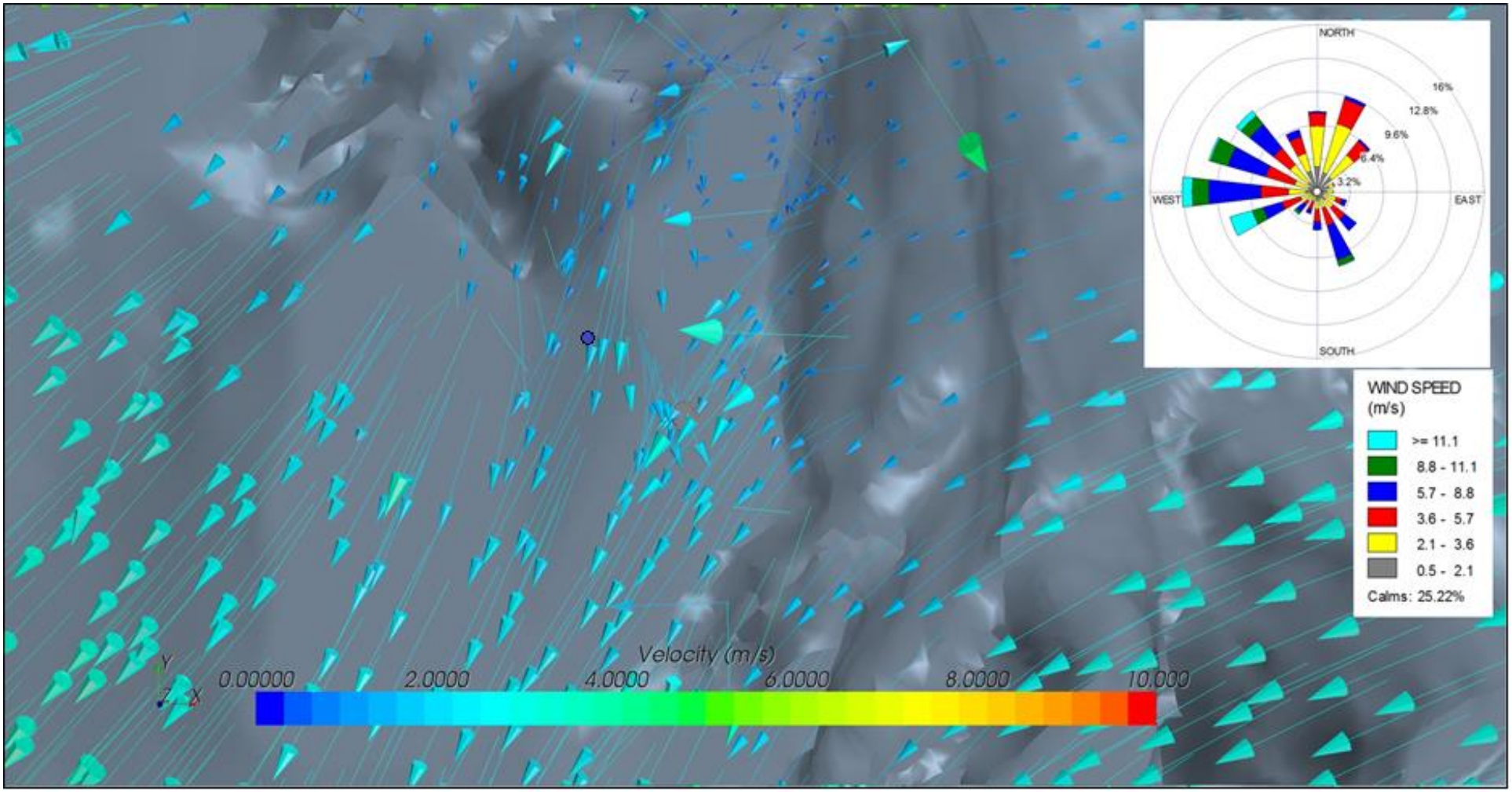

Figure 4-22:
850 hPa JJA simulated (arrows) and observed (wind rose – top right) results of wind speed and direction at 1900 m Above Mean Sea Level (AMSL) on Mariepskop. The blue circle represents the position of the 1900 m weather station.

4.6 Rainfall estimation

The eastern interior of South Africa (including the boundary between the Highveld and Lowveld – along South Africa's eastern escarpment where Mariepskop is situated) receives rainfall mainly during the summer season. It was therefore argued that streamlines generated by the STAR-CCM+ model for the DJF simulation can be used in order to delineate where summer rainfall occurs on Mariepskop. It was shown before that the largest percentage of summer winds come from the east or south-east, bringing moist air from the Indian Ocean. Where air rises it will be subjected to adiabatic cooling. If the rising air is moisture rich, condensation may take place if the air cools enough for the dew point temperature to be reached. The condensation of moisture in the air may lead to precipitation. Therefore it can be assumed that mountainous regions over which air ascends have a higher probability of receiving precipitation during summer months (DJF) than regions where air descends.

4.6.1 700 hPa DJF streamlines

Figures 4-20 to 4-23 indicate the flow of air modelled over Mariepskop in the form of streamlines. As the y-direction in the axis at the bottom of each figure indicates north, it is clear that the figures represent a northerly view of the Mariepskop mountain.

From each one of the figures it can be seen that air predominantly flows from the south east from where it reaches the eastern slopes of Mariepskop. The air, presumably moist, then climbs the eastern slope from where it flows smoothly over the mountain ridge. When the air reaches the western slope it descends and then forms a recirculation zone on the western slope of the mountain.

From this explanation of airflow over Mariepskop one would expect the eastern slope of Mariepskop to have a high probability of receiving precipitation as air ascends over the mountain. One would further expect the western slope to have a probability of receiving precipitation in the area where the recirculation zone forms, as air will rise when it circulates back to the western slope of the mountain.

In order to verify the accuracy of the streamlines generated by the model, an aerial photograph taken during the summer of 2008 (the most recent Google satellite image taken during the summer season over Mariepskop) were compared to the streamlines discussed in this section. Figure 4-24 depicts an aerial image in which the wetter and drier areas are indicated, according

to vegetation density, by means of green and orange circles (where green circles indicate areas assumed to be wet and orange circles assumed to be dry).

The areas appearing dark green on the aerial photograph in Figure 4-24 (therefore the areas assumed to receive the most precipitation) coincides very well with the areas where the model results showed ascending and recirculating airflow. The model was therefore able to simulate the general directions and patterns of airflow over Mariepskop relatively accurate.

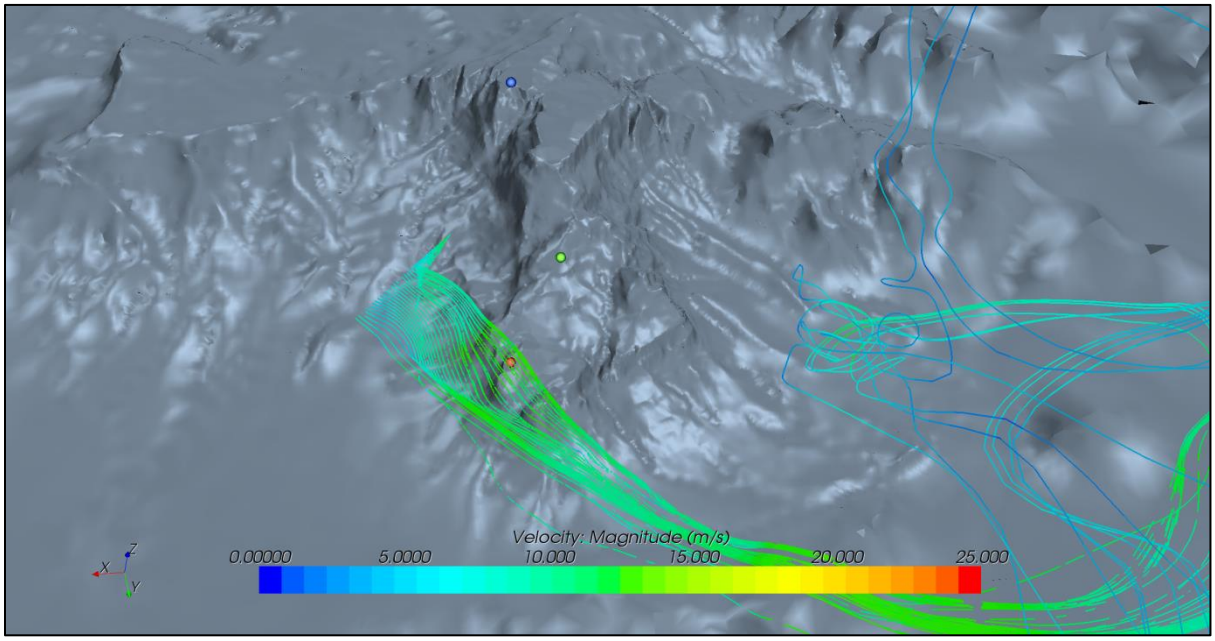

Figure 4-23:
Streamlines from the *700 hPa DJF simulation* at an altitude of 1200 m Above Mean Sea Level (AMSL).

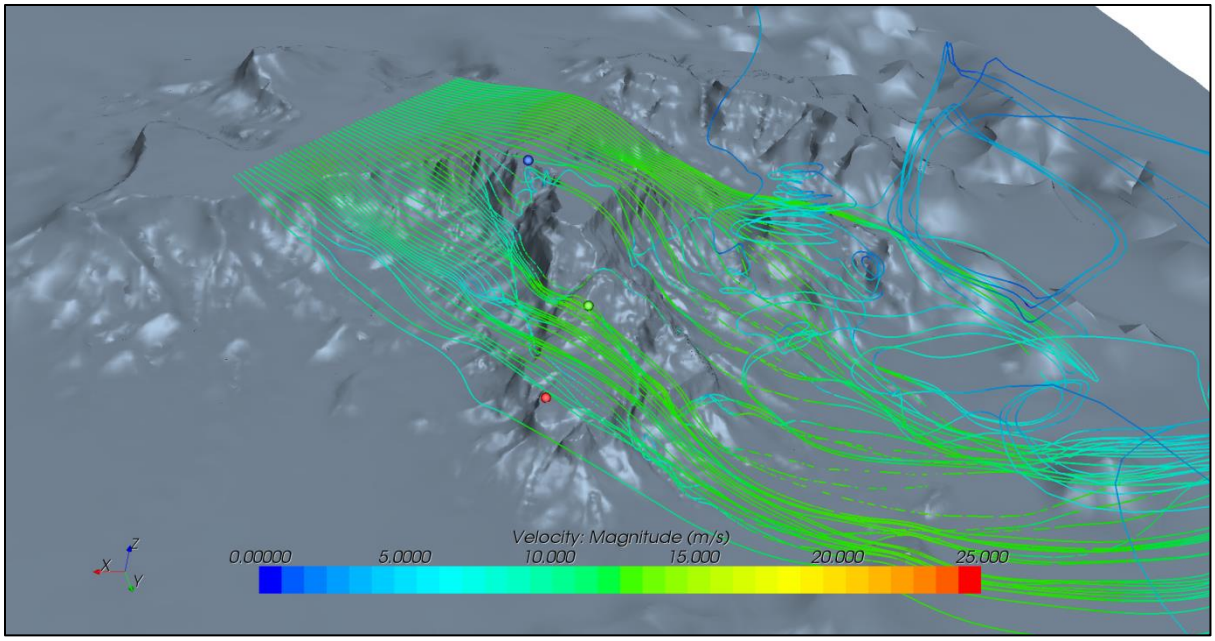

Figure 4-24:
Streamlines from the *700 hPa DJF simulation* at an altitude of 1800 m Above Mean Sea Level (AMSL).

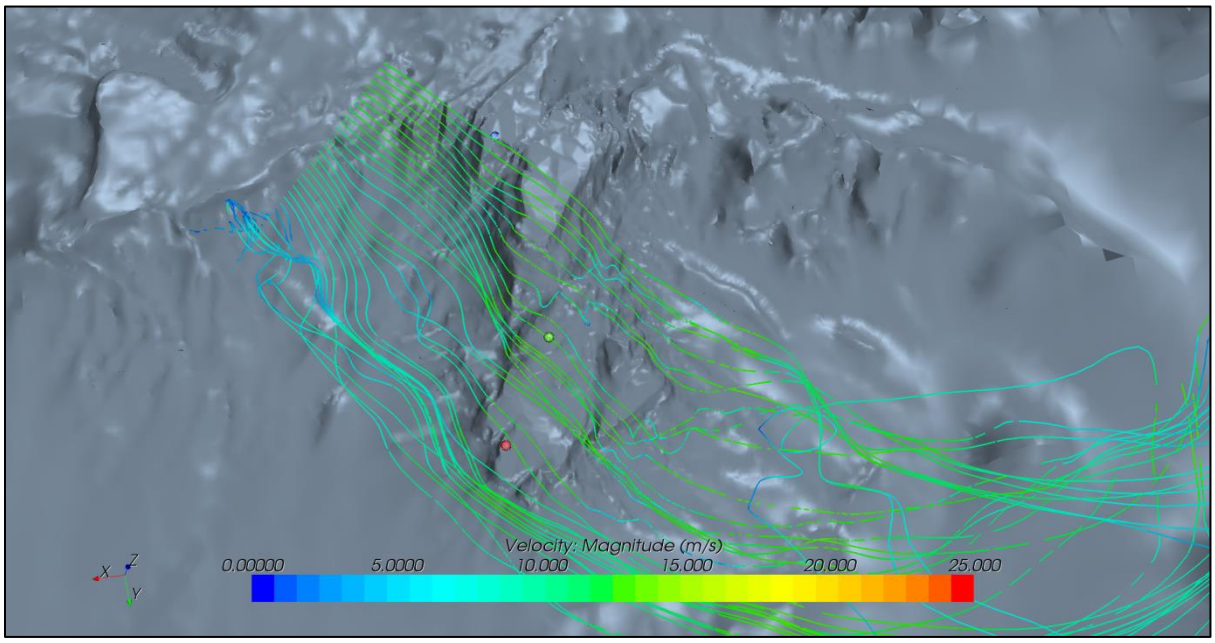

Figure 4-25:
A view from above of the streamlines from the *700 hPa DJF simulation* at an altitude of 400 m to 2000 m Above Mean Sea Level (AMSL).

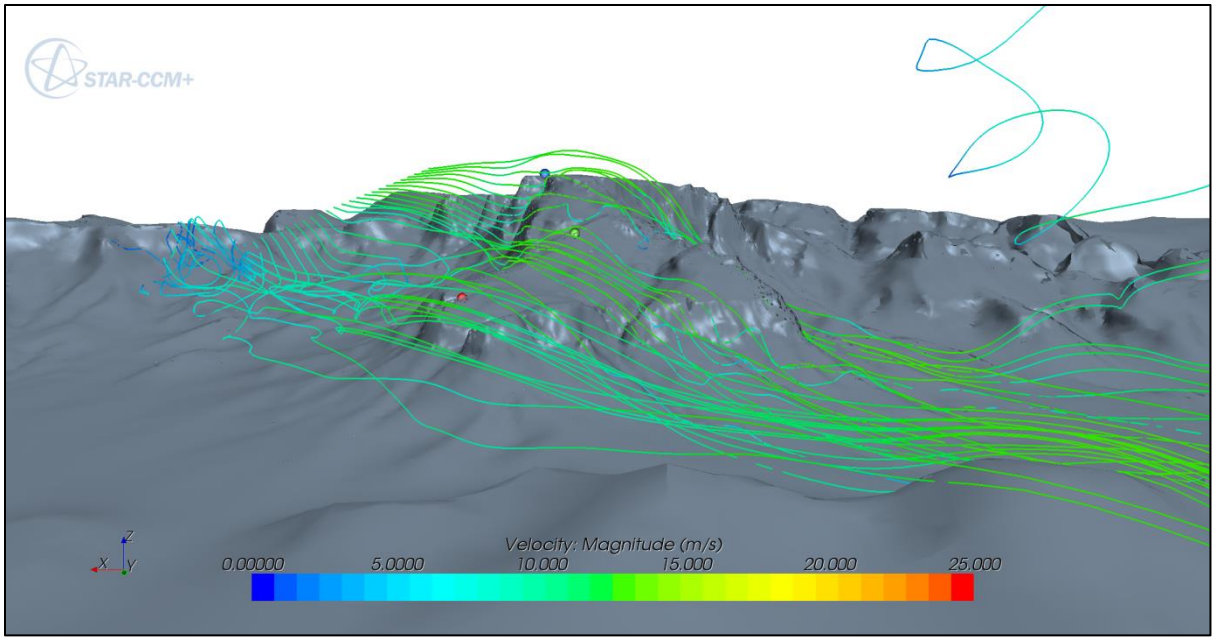

Figure 4-26:
A front view of the streamlines from the *700 hPa DJF simulation* at an altitude of 400 m to 2000 m Above Mean Sea Level (AMSL).

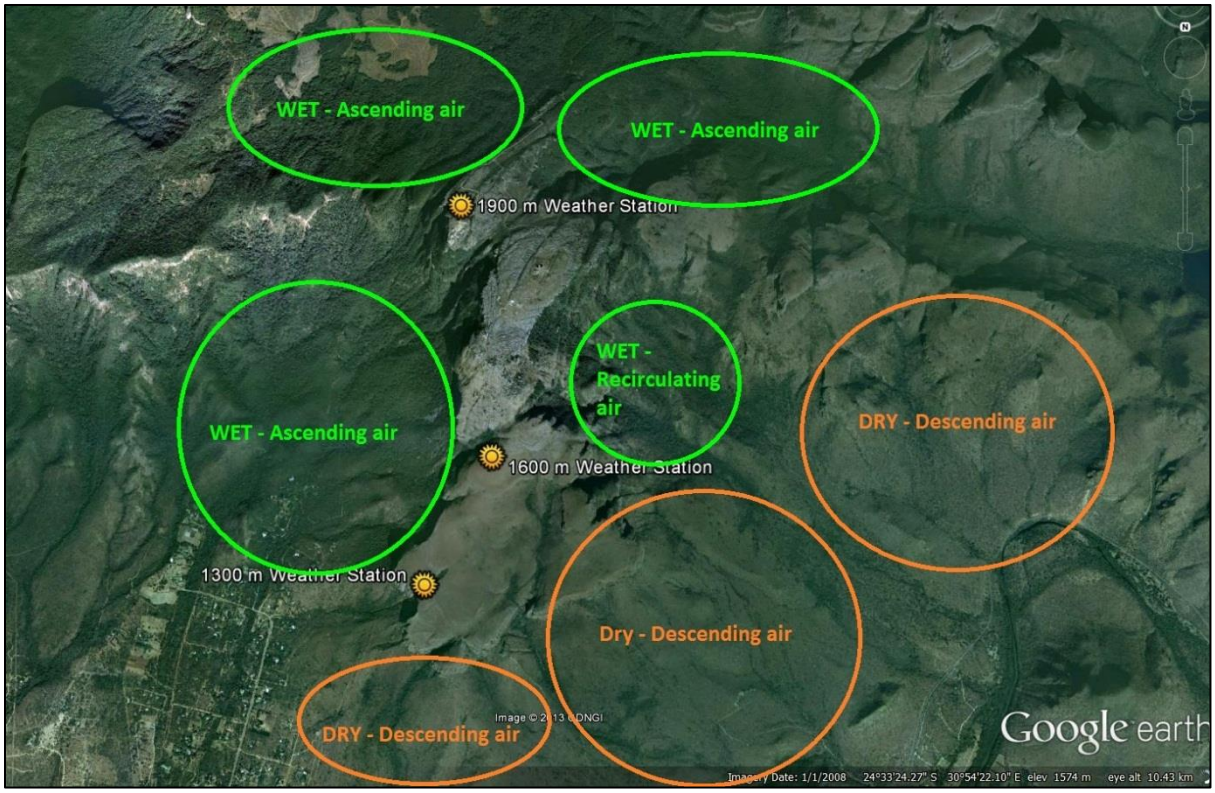

Figure 4-27:
An aerial photograph of Mariepskop where dark-green areas represent areas assumed to receive higher amounts of precipitation relative to light green areas assumed to receive less precipitation. The latter was used to draw circles of presumably “wet” (green circles) and “dry” (orange circles) areas. The location of the 1300 m, 1600 m and 1900 m observation sites are also shown.

5

Conclusions and recommendations

5.1 Overview

It is well known that complex terrain such as mountains have a profound effect on local and regional climates (Fridley, 2009; Daly *et al.,* 2007; Beniston, 2006; Wood, 2000 and Swanson *et al.,* 1988). Mountainous terrain often consists of a number of climatic zones which are usually associated with high biodiversity. According to Beniston (2006), some characteristics of orographic features are the rapid and systematic changes in climatic parameters, in particular temperature and precipitation, over short distances (Becker and Bugmann, 1997). Landforms, such as mountains, also influence the flow paths of winds (Swanson *et al.,* 1988). Winds usually increase near the crests of mountains and reduce and are more variable in the valleys and at the lee side of mountains. As a result, climate might change significantly with increases in altitude over relatively short horizontal distances, and so do vegetation patterns, hydrological features and biodiversity (Beniston, 2006; Whiteman, 2000). A consequence of the climatic diversity of mountains is that mountain ecosystems are often endemic, because many species remain isolated at high elevations compared to lowland vegetation communities that occupy climatic niches spread over wider surface areas (Beniston, 2006).

Mariepskop, which is an isolated but outstanding mountain located on the border of the Mpumalanga and Limpopo Provinces of South Africa, is well suited for climate studies. It is a high mountain peak that is partly isolated from the rest of the Drakensberg mountain range, making it ideal to study the effects of flow dynamics and climate over the mountain without significant interference in the flow from adjacent topography. Mariepskop also has many endemic fauna and flaura species making it a conservation concern. To date only limited studies were done on the climate of Mariepskop and none was done on its flow dynamics.

The flow dynamics of Mariepskop was studied by forcing averaged, long-term synoptic observations at Mariepskop across the lateral boundaries of a CFD model called STAR-CCM+. The argument was that, by doing so, one would be able to get an idea of the general average airflow over Mariepskop. Although CFD models have traditionally been used for engineering applications, they have been used more commonly in the meteorological realm over the last few years. CFD is used especially for wind flow modeling over complex terrain for wind-farm and fire

prediction applications (Stangroom, 2004; O'Sullivan *et al.,* 2010; Forthofer *et al.,* 2003; Watson *et al.,* 2004, Stander, 2008). The advantage of CFD models are that they can handle flow over complex terrain quite well and that they can be run at very fine resolutions. The disadvantage, however, is computational expense and the expertise to operate such a model (Stangroom, 2004). CFD model results obtained from this preliminary study were verified against weather station data that was collected at various altitudes on the mountain.

5.2 Conclusions

5.2.1 Long term synoptic data

Long-term NCAR/NCEP reanalysis wind data was obtained over Mariepskop at two atmospheric pressure levels (850 and 700 hPa). Near-surface temperature data was also collected. It was found that east-south-easterly and south-easterly wind directions prevail at both pressure levels during the summer months of DJF, and occur in association with both continental and ridging anti-cyclonic conditions. During the winter months of JJA, the predominant wind direction at 850 hPa is south-easterly and is due to the influence of ridging anticyclones. At 700hPa, however, the dominant wind direction is west-south-west. In near-surface temperatures a weak increasing temperature trend was observed for both seasons.

5.2.2 CFD model results

5.2.2.1 Wind speed

In this study it was found that the STAR-CCM+ model over predicted wind speeds during DJF, but succeeded in predicting the higher wind speeds at 1600 m and 1900 m AMSL relative to the wind speeds at 1300 m AMSL.

In the case of the JJA simulations, the model was relatively accurate in simulating wind speeds and relative wind speeds at different elevations on Mariepskop.

During both the summer and winter seasons it was observed that wind speeds increase with an increase in altitude. This finding correlates with existing literature (Stangroom, 2004; Nappo, 1977, Barry, 2008).

5.2.2.2 Wind direction

The model could simulate wind flow directions for all three simulations reasonably well. The correlations between modeled and observed results for the DJF and JJA 700 hPa simulations were better than that for the 850 hPa JJA simulation.

5.2.2.3 Rainfall

The model was able to identify areas of high probable rainfall for the summer season relatively accurately. It was found that higher rainfall is experienced on the windward side of Mariepskop (which is a finding consistent with literature (Wood, 2000)) and over a small area on the lee side where recirculation takes place.

5.2.3 General impression

CFD studies have been limited in the meteorological realm in the past mainly because of computing expense. As computing power becomes more accessible it is possible to use this extremely powerful tool to simulate meteorological problems. The STAR-CCM+ model performed well in this study and could model flow conditions over Mariepskop relatively successfully even though a simple set of averaged boundary conditions were used. This makes a strong case for using CFD models in similar studies in the future.

5.3 Recommendations

It is recommended that a simulation using an atmospheric model such as the WRF model be performed in future, as including moisture and rainfall in a CFD model such as the STAR-CCM+ model is difficult at this moment in time. It is also a possibility to couple the WRF atmospheric model with a CFD model such as STAR-CCM+ by down scaling the WRF model as far as possible and then feeding the atmospheric boundary conditions from WRF into a CFD model (instead of using simple averaged boundary conditions as in the case of this study) from where the CFD model can be run at high resolution. This will be a best case scenario as both models' advantages will be put to use.

Surface roughness and solar radiation could not be simulated in this study, due to a lack of computing power. However, as time progress and computing power becomes more accessible it might be beneficial to include these parameters in future simulations.

6 References

1. American Meteorological Society, (2000). Glossary of Meteorology, 2nd Ed, http://amsglossary.allenpress.com/glossary/search. Website created by Tim Keefer, Allen Press. Accessed 20 June, 2011.

1. Arya S.P.S, (1988). Introduction to Micrometeorology, Academic Press, Inc., San Diego, California.

2. Hewitson B.C. and Crane R.G., (2005). Consensus between GCM climate change projections with empirical downscaling: precipitation downscaling over South Africa. Int. J. of Climatol. Vol. 26, 1315-1337 (2006).

3. Banta, R. M., (1990). The role of mountain flows in making clouds. Atmospheric Processes over Complex Terrain, Meteor. Monogr. No. 45, Amer. Meteor. Soc., 173-228.

4. Barry, R. G., (1992). Mountain Weather and Climate. 2nd ed. Routledge, 402 pp.

5. Barry, R.G., (1994). Past and potential future changes in mountain environments: a review. In Beniston M. (ed.), Mountain Environments in Changing Climates. Routledge Publishing Company, London and New York, 3-33.

6. Becker, A. and Bugmann, H (eds.), (1997). Predicting Global Change Impacts on Mountain Hydrology and Ecology: Integrated Catchment Hydrology/Altitudinal Gradient Studies. International Geosphere-Biosphere Programme (IGBP) Report 43, Stockholm.

7. Beniston, M., (2003). Climatic change in mountain regions: a review of possible impacts. Climatic change, Vol. 59, 5-31.

8. Beniston, M., (2006). Mountain weather and climate: A general overview and focus on climatic change in the Alps. Hydrobiologica (2006), Vol 562, 3-16.

9. Berberan-Santos M.N., Bodunov E.N., and Pogliani L., (1997). On the barometric formula. Am. J. Phys. 65 (5), May 1997.

10. Caldwell, (2010). Statistics unplugged. Wadsworth Publishing, 2nd ed, 52 – 71.

11. CD-Adapco, (2011). 'STAR-CCM+ User Guide, Version 6.04', CD-Adapco.

12. Chen S.H. and Lin Y.L., (2004). Orographic effects on a conditionally unstable floe over and idealized three-dimensional mesoscale mountain. Meteorology and Atmospheric Physics.

13. Rife D.L., (1996).The effects of mountains and complex terrains on airflow and development of clouds and precipitation. Weston Union Technical Attachment, No.96-16, July, 1996.

14. Daly, C., Smith, J.W. and Smith, J.I., (2007). High-Resolution Spatial Modeling of Daily Weather Elements for a Catchment in the Oregon Cascade Mountains, United States. American Meteorological Society, Vol. 45, 1565-1586.

15. Kalnay E., Kanamitsu M., Kistler R., Collins W., Deaven D., Gandin L., Iredell M., Saha S., White G., Woollen J., Zhu Y., Chelliah M., Ebisuzaki W., Higgins W., Janowiak J., Mo K.C., Ropelewski C., Wang J., Leetmaa A., Reynolds R., Jenne R., Joseph D., (1996). The NMC/NCAR 40-Year reanalysis project. Bull. Am. Meteorol. Soc., Vol. 77, 437–471.

16. Epifanio, C.C., (2003). Lee vortices. In. Encyclopedia of the Atmospheric Sciences. Cambridge University Press, 1150-1160.

17. Federico S., Dalu G.A., Bellecci C., and Colacino M., (2000). Mesoscale energetics and flows induced by sea-land and mountain-valley contrasts. Ann. Geophysicae, Vol. 18, 235±246.

18. Flohn, H., (1968). Contributions to meteorology of the Tibetan Highlands. Atmospheric Physics. Paper 130, Dept. of Atmospheric Sciences, Colorado State University, Fort Collins, 120 pp.

19. Forthhofer J.M., Butler B.W., Shanon K.S., Finney M.A. and Bradshaw L.S., (2003). Predicting surface winds in complex terrain for use in fire spread models. Systems for Environmental Management, Missoula, MT.

20. Freytag C., (1984). Investigation of mesoscale weather phenomena in mountainous regions. Mountain Research and Development, Vol. 4, No. 4, 305-313.

21. Fridley J.D., (2009). Downscaling Climate over Complex Terrain: High Finescale (<1000 m) Spatial Variation of Near-Ground Temperatures in a Montane Forested Landscape (Great Smoky Mountains). American Meteorological Society, Vol.48, 1033-1049.

22. Galewsky J., (2008). Orographic Clouds in Terrian-Blocked Flows: An Idealized Modeling Study. Am. Meteorol. Soc., Vol. 65, 3460-3478.

23. Garstang M., Tyson P.D., Swap R., Edwards M., Kallberg P. and Lindsay J.A., (1996). Horizontal and vertical transport of air over southern Africa. J. Geophys. Res. Vol. 101(D19), 23721-23736.

24. Geiger R., Aron R.H. and Todhunter P., (2003). The Climate near the Ground. 6th ed. Rowmann and Littlefield, 584 pp.

25. Hemp A., (2005). Climate change-driven forest fires marginalize the impact of ice cap wasting on Kilimanjaro. Global Change Biology, Vol. 11, 1013-1020.

26. Holton J.R., (2004). An Introduction to Dynamic Meteorology. International Geophysics, Vol. 88, 1-535.

27. International Organization for Standardisation, (1975). Standard Atmosphere.

28. IPCC, (2007). Climate Change 2007: The Physical Science Basis Contribution of Working Group I to the Fourth Assessment Report of the Environmental Panel on Climate Change [Solomon, S., Qin D., Manning M., Chen Z., Marquis M., Averyt K.B., Tignor M. and Miller H.M. (eds.)]. Cambridge University Press, Cambridge, United Kingdom and New York, NY USA, 996 pp.

29. Dutton J.A., (1986).Dynamics of Atmospheric Motion. Dover, New York, Chap. 4.

30. Iribarne J.V. and Godson W.L., (1981). Atmospheric Thermodynamics. Reidel, Dordrecht, The Netherlands, 2nd ed., Chap. 8.

31. Jongen T. 1998. Simulation and Modelling of Turbulent Incompressible Flows, Ph.D. Thesis, Lausanne EPFL.

32. Kaimal J. C., Finnigan J.J. (1994). Atmospheric Boundary Layer Flows: Their structure and measurement, Oxford University Press.

33. Laprise R., (1992). The Euler Equations of Motion with Hydrostatic Pressure as an Independent Variable. Mon. Wea. Rev., Vol. 120, 197-207.

34. Lindeman J.D., (2008). A numerical study of orographic effects on flow regimes in the lower atmosphere. George Madison University, 151 pp.

35. Lundquist K.A., Chow F.K., Lundquist J.K. and Kosovic B., (2009). Accurate Wind Characterization in Complex Terrain Using the Immersed Boundary Method. The Fifth International Symposium on Computational Wind Engineering. Chapel Hill, NC, United States, May 23, 2010 through May 27, 2010.

36. NCEP Reanalysis data provided by the NOAA/OAR/ESRL PSD, Boulder, Colorado, USA, from their Web site at http://www.esrl.noaa.gov/psd/, accessed April, 2011.

37. Nel W., (2007). On the climate of the Drakensberg: rainfall and surface-temperature attributes, and associated geomorphic effects. Doctoral Thesis, Department of Geography, Geoinformatics and Meteorology, University of Pretoria.

38. Ooyama K.V., (1990). A Thermodynamic Foundation for Modeling the Moist Atmosphere. Journal of Atmospheric Science, Vol. 21, 2580-2593.

39. Orville H. D., (1965). A numerical study of the initiation of cumulus clouds over mountainous terrain. J. Atmos. Sci., Vol. 22, 684-699.

40. Orville H. D., (1968). Ambient wind effects on the initiation and development of cumulus clouds over mountains. J. Atmos. Sci., Vol. 25, 385-403.

41. O'Sullivan J.P., Pecnik R. and Laccarino G., (2010). Investigating turbulence in wind flow over complex terrain. Center for turbulence Research, Proceedings of the Summer Program, 2010, 129 – 139.

42. Reid P.A., Jones P.D., Brown O., Goodess C.M. and Davies T.D., (2001). Assessments of the reliability of NCEP circulation data and relationships with surface climate by direct comparisons with station based data. Climate Research, Vol. 17, 247 – 261.

43. Pathirana A., Yamaguchi M., and Yamada T., (2003). Idealized simulation of airflow over a mountain ridge using a mesoscale atmospheric model. Annual Journal of Hydrologic Engineering, JSCE, Vol. 47, February, 2003.

44. Pinard J.P., (1999). Computer Models for Wind Flow over Mesoscale Mountainous Terrain Applied to the Yukon. 45 pp.

45. Raymond W.H., (1986). Topographically-induced mesoscale motions in antitriptically balanced barotropic flow. Tellus, Vol. 38A, p. 251-262.

46. Reynolds O., (1895). On the dynamical theory of incompressible viscous fluids and the determination of the criterion. Proceedings of the Royal Society of London. Vol. 451.

47. Rodi W., (1991). Experience with Two-Layer Models Combining the k-ε Model with a One-Equation Model Near the Wall. 29th Aerospace Sciences Meeting, January 7-10, Reno, NV, AIAA, 91-0216.

48. Ross K.E., Piketh S.J., Swap R.J. and Staebler R.M., (2001). Controls governing airflow over the South African Lowveld. South African Journal of Science, Vol. 97, 29-40.

49. Salim M.S., and Sheah S.C., (2009). Wall y+ Strategy for Dealing with Wall-bounded Turbulent Flows. Proceedings of the International Multi-Conference of Engineers and Computer Scientists 2009. Vol II IMECS 2009, March 18 - 20, 2009, Hong Kong.

50. Shamarock S., Klemp J.B., Dudhia. J., Gill D.O., Barker. D.M., Wang W. and Powers, G., (2005). A description of the Advanced Research WRF Version 2. NCAR Technical note, Mesoscale and Microscale Meteorology Division, National Center for Atmospheric research, Boulder, Colorado, USA.

51. Shih T.H., Liou W.W., Shabbir A., Yang Z. and Zhu J., (1994). A New k-ε Eddy Viscosity Model for High Reynolds Number Turbulent Flows - Model Development and Validation. NASA TM 106721.

52. Shreve F., (1912). Cold air drainage and plant distribution. Plant World, Vol. 15, 110-115.

53. Smith R.B., (1982). Synoptic observations and theory of orographically disturbed wind and pressure. J. Atmos. Sci., Vol. 39, p. 60-70.

54. Stander, N.J., (2008). The specification of a small commercial wind energy conversion system for the South African Antarctic Research base, Sanae IV. Master of Science in Engineering Thesis, University of Stellenbosch, 2008. 168 pp.

55. Stangroom P., (2004). CFD Modelling of Wind Flow over Terrain. Thesis submitted to The University of Nottingham for the degree of Doctor of Philosophy, January 2004, 298 pp.

56. Swanson F.J., Kratz T.K. Caine N. and R.G. Woodmansee, (1988). Landform effects on Ecosystem Patterns and Processes: Geomorphic features of the earth's surface regulate the distribution of organisms and processes. Bioscience, Vol. 38 No. 2, 92-98.

57. Tennant W., (2004). Considerations when using pre-1979 NCEP/NCAR reanalyses in the southern hemisphere. Geophysical Research Letters 31: L11112, DOI: 10.1029/2004GL019751.

58. Tiwary A. and Colls J., (2010). Air Pollution: Measurement, modelling and mitigation, (3rd Ed). Taylor and Francis Routledge Group, Chapter 6.

59. Tyson P.D., Garstang M., Swap R., Kallberg P. and Edwards M., (1996). An air transport climatology for subtropical southern Africa. Int. Climatol., Vol. 16, 265-291.

60. Tyson P.D., Preston-Whyte R.A., (2000). The Weather and Climate of South Africa. Oxford University Press South Africa, 2nd edition. 396 pp.

61. Volkert H., Binder P. Benoit R. Bougeault P., Buzzi A., Mayr G., Schar and Steinacker R., (1996). The Mesoscale Alpine Programme (MAP): An international research initiative in Alpine meteorology. Internationales Symposion, Interpraevent 1996 – Garmisch-Partenkirchen, Tagungspublikation, Band 1, 55-63.

62. Watson G., Douglas N. and Hall S., (2004). Comparison of wind flow models in complex terrain. Natural Power Consultants Ltd., The Green House, Forrest Estate, St John's Town of Dalry, Castle Douglas, Dumfries and Galloway, Scotland.

63. White F.M., (2006). Viscous Fluid Flow, 3rd Edition. McGraw Hill International Edition, 629 pp.

64. Whiteman D., (2000). Mountain Meteorology. Oxford University Press, 355 pp.

65. Wood N., (2000). Wind flow over complex terrain: A historical perspective and prospect for large-eddy modeling. Boundary-Layer Meteorology, Vol. 96, p 11-32.

66. Zoumakis N.M., (1992). On the Relationship between the Gradient and the Bulk Richardson Number for the Atmospheric Surface Layer. Nuevo Cimento, 15C, 111 – 114.